IRE
Transactions
on ANTENNAS and PROPAGATION

Volume AP-6 OCTOBER, 1958 Number 4

Published Quarterly

TABLE OF CONTENTS

CONTRIBUTIONS

COMMUNICATIONS

PUBLISHED BY THE
Professional Group on Antennas and Propagation

IRE TRANSACTIONS® PGAP IS A QUARTERLY PUBLICATION DEVOTED TO EXPERIMENTAL AND THEORETICAL PAPERS ON ANTENNAS AND WIRELESS PROPAGATION OF ELECTROMAGNETIC WAVES

MANUSCRIPTS should be submitted to John B. Smyth, Editor, Smyth Research Associates, 3555 Aero Court, San Diego 11, Calif. Manuscripts should be original typewritten copy, double spaced, plus one carbon copy. References should appear as footnotes and include author's name, title, journal, volume, initial and final page numbers, and date. Each paper must have a summary of not more than 200 words. News items concerning PGAP members and group activities should be sent to the News Editor, Mr. Arthur Dorne, Dorne and Margolin, Inc., 30 Sylvester Street, Westbury, L.I., N.Y.

ILLUSTRATIONS should be submitted as follows: All line drawings (graphs, charts, block diagrams, cutaways, etc.) should be inked uniformly and ready for reproduction. If commercially printed grids are used in graph drawings, author should be sure printer's ink is of a color that will reproduce. All halftone illustrations (photographs, wash, airbrush, or pencil renderings, etc.) should be clean and ready to reproduce. Photographs should be glossy prints. Call-outs or labels should be marked on a registered tissue overlay, not on the illustration itself. No illustration should be larger than 8 x 10 inches.

Copies can be purchased from
THE INSTITUTE OF RADIO ENGINEERS
1 East 79 St., New York 21, N.Y.

PRICE PER COPY: members of the Professional Group on Antennas and Propagation, $1.50; members of the IRE, $2.25; nonmembers, $4.50.

ANNUAL SUBSCRIPTION PRICE: PGAP members, included in PGAP fee of $4.00; IRE members, $8.50; Colleges and public libraries, $10.00; nonmembers, $17.00.

IRE Transactions on Antennas and Propagation

Printed in U.S.A.

Entered as second-class matter, at the post office at Menasha, Wisconsin, under the act of August 24, 1912. Acceptance for mailing at a special rate of postage is provided for in the act of February 28, 1925, embodied in Paragraph 4, Section 412, P. L. & R., authorized October 26, 1927.

contributions

The Effect of Echo on the Operation of High-Frequency Communication Circuits*

D. K. BAILEY†

Summary—**Echo on high-frequency communication services is defined as the simultaneous reception of signals over both major and minor arcs of the great circle connecting a transmitter and receiver. Two distinct kinds of echo are recognized according to the illumination conditions under which they occur. Echo of the first kind is observed when the great-circle path coincides with the twilight zone surrounding the earth, whereas echo of the second kind, which can occur only on fairly long communication paths, is most severe when the short path is most intensely illuminated. Little can be done to obviate echo of the first kind and it is not, like echo of the second kind, amenable to prediction by available methods of calculating sky-wave field intensities. Radio traffic data are cited which corroborate calculations and show both that echo of the second kind is more severe at times of maximum solar activity, and is less severe on higher frequencies. Conclusions are drawn concerning mode of operation and choice of operating frequency to minimize echo interference.**

Introduction

RADIO engineers operating high-frequency communication circuits over long distances have for many years identified a certain type of difficulty in the operation of their circuits with the simultaneous reception of signals over both the major arc (known as the long path) and the minor arc (known as the short path) of the great circle connecting the transmitter and the receiver. The identity of the long-path signals is easily established by the determination of their delay times with respect to the short-path signals. This reception condition is known as echo because of the aurally perceptible delays in telegraphy and the hollow "large auditorium" sound of telephony. Echo should not be confused with multipath distortion of high-speed telegraphic communication which is the result of the difference in arrival time between the first and last significant modes of propagation between transmitter and receiver along the same portion of the entire great circle. If the very difficult case of antipodal circuits (circuits of the order of 18,000 km or longer in length) is excluded, it may be said that the simple echo condition described above is characterized by delays of the order of 10 to 100 msec. Such delays are capable of preventing any but slow-speed telegraphy and of causing annoyance to users of telephony.

In the course of an investigation of echo and its relationship to the mode of operation and the choice of operating frequencies, it was found to be possible to distinguish two quite distinct types of echo, according to the conditions under which they occur.[1]

* Manuscript received by the PGAP, August 12, 1957. Originally issued as Natl. Bur. of Standards report (1951), Washington, D. C. The material in this paper constitutes one of the necessary preliminary investigations undertaken by the author in connection with his duties as Chairman of the Propagation Working Group of the Provisional Frequency Board of the International Telecommunications Union, which met at Geneva, Switzerland, from 1948 to 1950. It reflects the international character of the Geneva activities. The Propagation Working Group was specifically charged with the duty of establishing on an engineering basis rules for the selection of operating frequencies for high-frequency point-to-point radio communications.

† Page Communications Engineers, Inc., Washington, D. C. Formerly with Natl. Bur. of Standards, Washington, D. C.

[1] "Second Report of Working Group 1 (Propagation) Committee 4," Internatl. Telecommun. Union, Provisional Frequency Board, Geneva, Switzerland, Doc. No. 375-E, pp. 4–5; October 6, 1948.

Echo of the First Kind

Echo of the first kind is observed on circuits having lengths as short as 5000 km and occurs only at times when the great-circle path connecting the transmitter and receiver is coincident or nearly coincident with the twilight great circle which surrounds the earth. Under this particular illumination condition the attenuation of radio waves is at times much less than can be accounted for by use of any of the presently available quasi-empirical tools for the computation of skywave field intensities.[2] The broken-line curve in Fig. 2, considered in the light of the discussion of the next section, illustrates this failure in a specific manner. In fact numerous observations are known which have revealed observable signals that traveled once and occasionally several times entirely around the earth in both directions in the twilight zone. For observers located in the skip-zone of nearby high-powered transmitters, a special case of twilight-zone echo is sometimes observed with delays approximating $\frac{1}{7}$ of a second. It is the result of the time delay between the scattered signal (often arriving from some direction other than the true direction of the transmitter), or a weak direct signal, and the signal which has passed entirely around the earth in the twilight zone. Hess[3,4] has recently published results of studies of the twilight-zone type of echo, and provides useful references to early reports. He and the earlier workers appear to have observed echo only of the first kind. This can probably be ascribed to the fact that their observations were made at times of intermediate and low solar activity, a circumstance which would account for their belief that echo could only occur under twilight-zone conditions.

There is at present insufficient understanding of echo of the first kind to permit an evaluation of its effect on the selection of operating frequencies for high-frequency communication. It seems fairly clear however that echo of the first kind is independent of transmitter power, and that improving the front-to-back ratio of the transmitting and receiving antennas in view of the complete round-the-world possibilities can at best be of limited use in obviating it as a source of cochannel interference. Echo of the first kind can occur with serious consequences at all phases of the solar cycle.

Echo of the Second Kind

Echo of the second kind is observed on circuits having short-path lengths greater than 8000 to 10,000 km at times when the short path is most intensely illuminated. It seems to have its most serious consequences to the communications services when the sun is near or at the zenith at the midpoint of the short path. For a particular operating frequency it is more serious at periods of maximum than at periods of minimum solar activity.

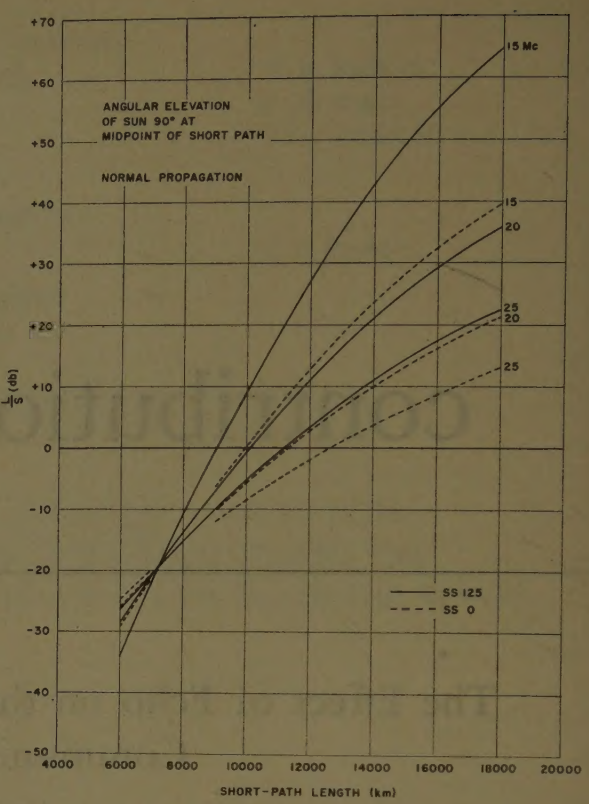

Fig. 1—Calculated severity of echo of the second kind as produced under the most favorable illumination condition.

Presently available methods for the computation of long-term median sky-wave field intensities[2] permit the prediction of a number of characteristics of echo of the second kind. If normal propagation is assumed to be possible over both the long and short paths, it is possible to calculate, for an omnidirectional transmitting antenna, the ratio of the median field intensities of the long to the short path at the receiving location. This ratio, called L/S, is expressed in Figs. 1 to 3 in decibels. It measures the severity of the echo condition. The main parameters involved in its calculation are:

1) Length of short path,
2) Frequency,
3) Geometrical position of the sun relative to the long and short paths (uniquely given by two angles, *viz.* the angular elevation of the sun at the midpoint of the short path, and the orientation of the short path at its midpoint with respect to the minor arc of the great circle which connects the midpoint of the short path to the subsolar point),
4) Level of solar activity (as measured by the smoothed relative sunspot number, abbreviated "SS" on the figures), and
5) Auroral-zone absorption on the long path (taken to be zero on all the curves except one on Fig. 3 for which representative maximum auroral-zone effects have been introduced).

[2] "Ionospheric Radio Propagation," Natl. Bur. of Standards, Washington, D. C., Circular 462, pp. 104–150; June 25, 1948.
[3] H. A. Hess, "Investigations of high-frequency echoes," Proc. IRE, vol. 36, pp. 981–992; August, 1948.
[4] H. A. Hess, "Part II—Investigations of high-frequency echoes," Proc. IRE, vol. 37, pp. 986–989; September, 1949.

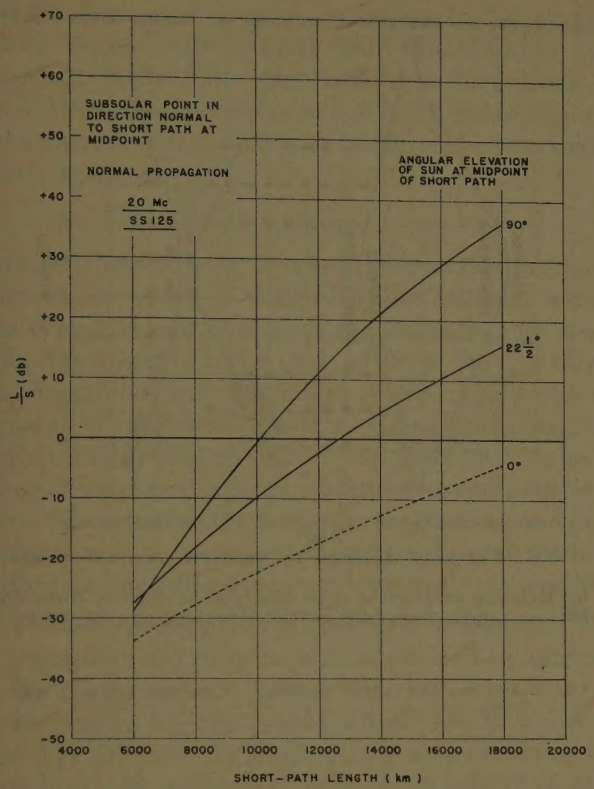

Fig. 2—Calculated severity of echo of the second kind for a frequency of 20 mc for various illumination conditions.

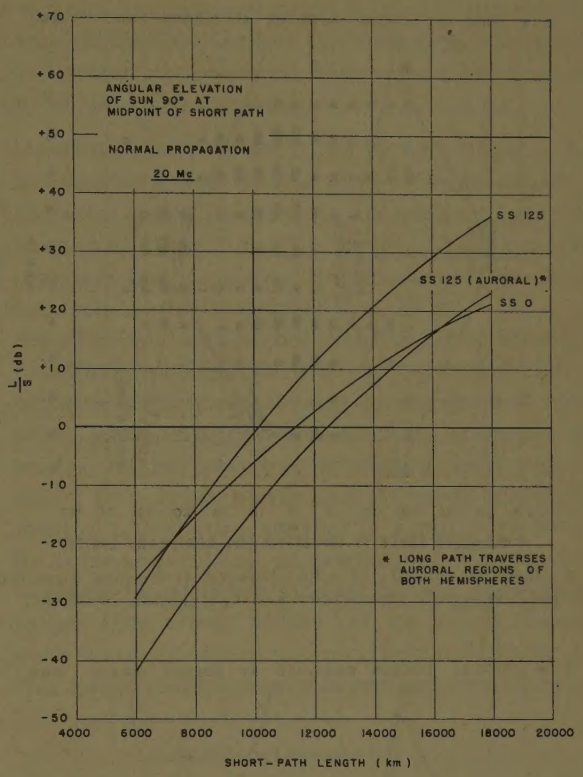

Fig. 3—Calculated severity of echo of the second kind for a frequency of 20 mc as produced under the most favorable illumination condition for representative levels of solar activity, including the auroral case.

Then, considering a range of short-path lengths from 8000 to 18,000 km, by varying each of the main parameters in the order above in turn, it is seen in Figs. 1 to 3 for a variety of typical absorption conditions and frequencies, that the echo condition:

1) Increases in seriousness with length of short path,
2) Varies in seriousness as an inverse function of frequency,
3) Is most serious when the sun is overhead at the midpoint of the short path,
4) Varies in seriousness as a direct function of solar activity, and
5) Decreases in seriousness with increasing auroral disturbance to the long path.

In addition to the main points above, the following additional points are also brought to light by the calculations:

6) There appears to exist a critical short-path length below which echo effects vary in seriousness directly with frequency. This critical short-path length is a function of the geometrical position of the sun relative to the long and short paths, but is too small for serious echo effects on any frequency likely to be of practical use.
7) The effect of introducing auroral absorption on the long path is to depress a particular curve of the type shown in Fig. 1 by an amount independent of short-path length but dependent upon frequency. Curves for lower frequencies are more depressed. This would have the effect, for example in Fig. 1, of increasing the critical short-path length as discussed in the preceding point.

None of these conclusions is valid for very low angles of elevation of the sun at the path midpoint, when, with suitable path orientation, the necessary condition for echo of the first kind is established.

Comparison with Observations

Direct evidence in support of the first five predicted characteristics of echo of the second kind, as well as examples of echo of the first kind, are available in receiving station logs.

Figs. 4 and 5 show the observed occurrence of echo without regard to kind on the circuit from London to Buenos Aires as observed at Buenos Aires on the principal day frequency used for this 11,000-km circuit for 1947, a year of maximum solar activity, and for 1944, a year of minimum solar activity. The station being received is GLW operating on a frequency of 19,100 kc. The figures show, by the heights of the blocks, the relative severity of the echo, if present, which was observed at each hour of the day for each month of the year. The units are arbitrary. Sunrise and sunset curves are shown for each terminal of the path. The occurrence of echo of the first kind is thus identifiable during the morning twilight most markedly in December and January, and during the evening twilight most markedly in June

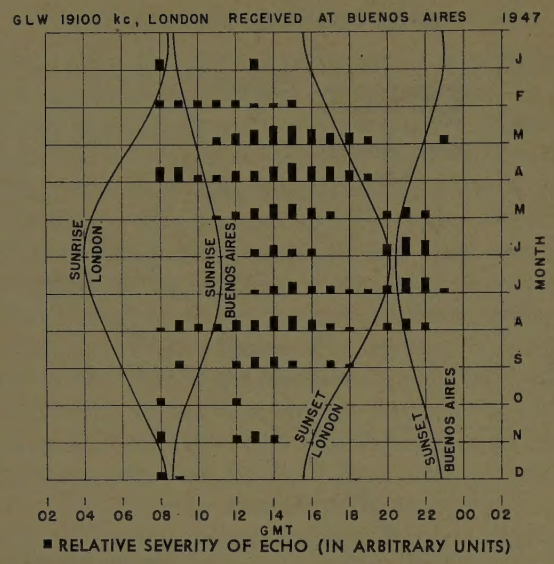

Fig. 4—Relative severity of echo observed at Buenos Aires during 1947 on signals from station GLW, England, 19,100 kc.

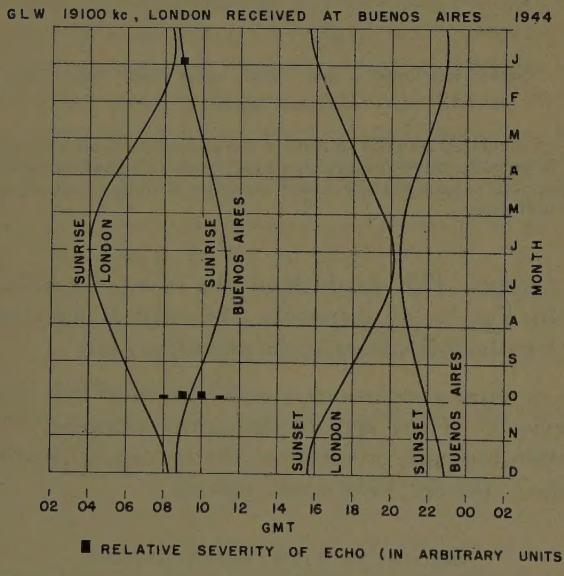

Fig. 5—Relative severity of echo observed at Buenos Aires during 1944 on signals from station GLW, England, 19,100 kc.

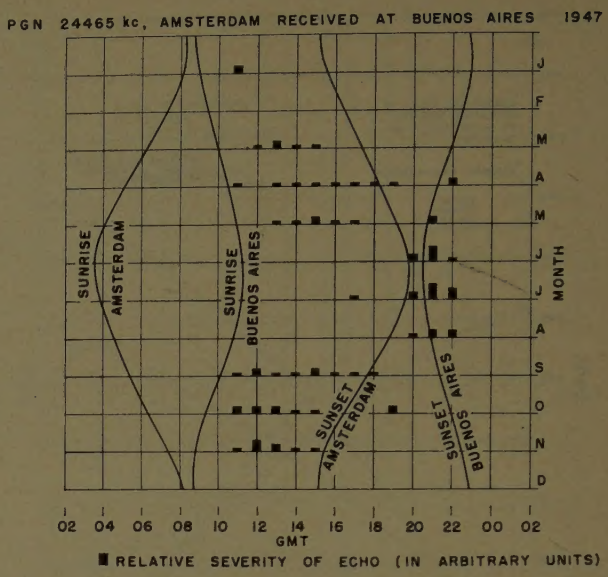

Fig. 6—Relative severity of echo observed at Buenos Aires during 1947 on signals from station PGN, Netherlands, 24,465 kc.

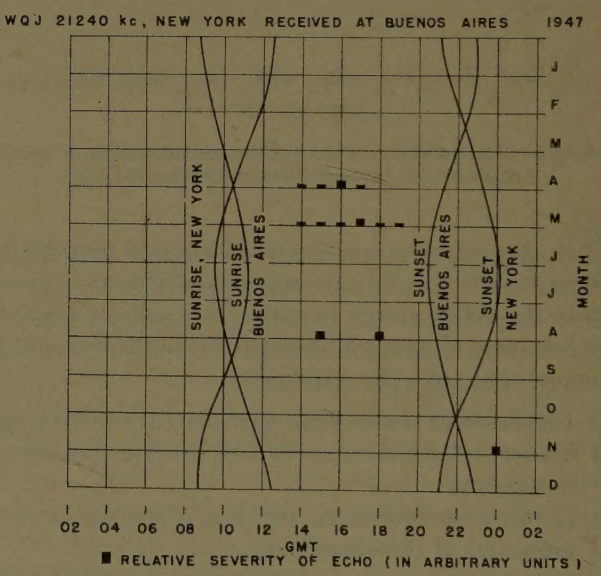

Fig. 7—Relative severity of echo observed at Buenos Aires during 1947 on signals from station WOJ, New York, 21,240 kc.

and July. At other seasons the twilight zone does not coincide very closely with the path at any time of day. During 1944 the operating frequency under consideration was sufficiently high to receive relatively little use at times when echo of the first kind could occur.

With regard to echo of the second kind Figs. 4 and 5 reveal that the effects are most severe at maximum solar activity, and of no serious consequence for the particular case shown at minimum. Furthermore the sun is most nearly vertical at the short-path midpoint during the months of April and August; the observations of Fig. 4 reveal more serious echo of the second kind during these months, and show definite minima in the solstice months. As would be expected from the foregoing and from the actual geographical position of the short path, the minimum at the December solstice is the deeper. The improvement to be obtained by the use in 1947 of a higher frequency is illustrated by Fig. 6 which presents the echo observations at Buenos Aires for a frequency of 24,465 kc as transmitted by station PGN during its use on the Amsterdam to Buenos Aires circuit. The paths London to Buenos Aires and Amsterdam to Buenos Aires are considered sufficiently similar to permit direct comparison. It is unlikely that the full benefits to be derived from use of a higher frequency are revealed by the comparison of Figs. 4 and 6 since the realizable front-to-back gain of the transmitting Franklin beam array at London is probably significantly greater than that of the rhombic used at Amsterdam. Fig. 7 presents the echo observation made during 1947 at Buenos Aires of station WQJ used for the New York to Buenos Aires circuit and operating on

21,240 kc. This path is about 8500 km in length and therefore significantly shorter than the London and Amsterdam paths. The long path from New York to Buenos Aires passes directly across both polar regions, and the observation of only very slight echo disturbance is clearly revealed.

Conclusions

Without definite and detailed information on such matters as the value of the protection ratio for a particular type of telegraph service against cochannel interference, the benefits to be derived from the use of diversity reception, and the values of realizable front-to-back gains of transmitting and receiving antennas, it is not profitable to discuss further the problem of echo of the second kind as it affects particular communications circuits. Nevertheless the following conclusions of a general nature may be expressed with regard to the mode of operation of high-frequency communications circuits:

1) The interference effects of echo of either kind in a particular situation cannot be reduced by increasing the power,
2) Increasing the realizable front-to-back gains of either or both the transmitting and receiving antennas will reduce the interference effects of echo of the second kind,
3) Introduction of diversity gain or improvement in diversity gain of the receiving antennas will reduce the interference effect of echo of the second kind, and
4) Use of the long path, particularly for larger values of short-path length such as 12,000 to 18,000 km, with adequate transmitting and receiving antenna directivity, will often give a usable service when the short path is unusable with the antennas and frequency available, because of echo of the second kind.

For circuits having short paths subject to interference from echo of the second kind, the following conclusions may be tentatively expressed with regard to the selection of the operating frequency:

5) It is important to select the highest possible day frequency for use during the minimum phases of the solar cycle in order to minimize echo interference at these times. It would appear for most practical purposes that this frequency should lie between approximately 18 and 20 mc.
6) An additional and higher day frequency should be provided, according to the propagational characteristics of the path, for use during years of maximum solar activity when the day frequency described in the preceding conclusion suffers excessively from echo interference. It would appear for most practical purposes that this frequency should lie as far above 22 mc as practicable. For very long circuits, for example circuits having short paths longer than about 14,000 km, on which the long path is nonauroral should receive considerable use, this additional frequency is probably unnecessary.

Acknowledgment

The author wishes to acknowledge the very helpful counsel received at Geneva from A. M. Humby, formerly of Cable and Wireless, Ltd., and now of the British Admiralty Signals Department, without whose insistence and vast fund of experience this investigation would not have been undertaken. He also expresses his thanks to P. J. Noiseux and to his company, Transradio Internacional, Compania Argentina de Telecomunicaciones S. A., without whose very competently analyzed reception logs it would have been impossible to demonstrate the observational side of echo in such a convincing manner.

Foreground Terrain Effects on Overland UHF Transmissions*

L. G. TROLESE† AND L. J. ANDERSON†

Summary—**This paper describes an experimental study of the influence of the shape of foreground terrain profiles near terminals of UHF links on the received field. A gently rounded shape of the foreground profile causes a marked diffraction pattern to be superimposed on the normal variation of field strength with height. The diffraction geometry shows similarity to knife-edge geometry and the rounded terrain feature appears to act geometrically as an equivalent knife edge. The amplitude of the spatial variations in signal are, however, much greater than knife-edge theory predicts. A sizeable foreground diffraction enhancement of received field can be realized by locating the antenna at the height of the first diffraction maximum. Changing refraction due to meteorological variations can change both the position in height and intensity of the diffraction pattern.**

Introduction

TERRAIN features which affect the propagation of UHF transmissions can be divided into several general classes. Large dominant obstacles such as mountains and mountain ridges have been studied in considerable detail, and many papers have appeared in the literature on this subject. The classical knife-edge theory has been used with reasonably good success in predicting the field to be expected in the shadow region behind such large obstacles.

Another class of terrain features which has received considerable attention is a terrain composed of irregularities which vary in a random way. For short wavelength transmissions the sea surface is usually considered to be of this type, and most overland paths have irregularities which are certainly random in nature.

This paper, however, is concerned with terrain features which are in neither of the two classes listed above. The experimental studies which are described concern the influence of the foreground terrain near the terminals of UHF links on the received field strength. The shape of the foreground terrain was found to have a marked influence on the manner in which the field strength varied with antenna height. The section of foreground terrain under study in this case is neither randomly irregular nor is it a dominant obstacle, but takes the form of a relatively smooth gently varying departure from a spherical earth. The data were all taken on paths in Arizona over relatively smooth desert terrain. Some of the foreground terrain effects on these paths were briefly mentioned in previous papers.[1,2] Ament and Katzin,[3] in microwave propagation studies in the Pacific, noted that foreground terrain features in the form of the moving ocean swells caused variations in the field strength received on a shore-based receiving terminal. The foreground terrain was pictured as being "coupled" to the receiving antenna.

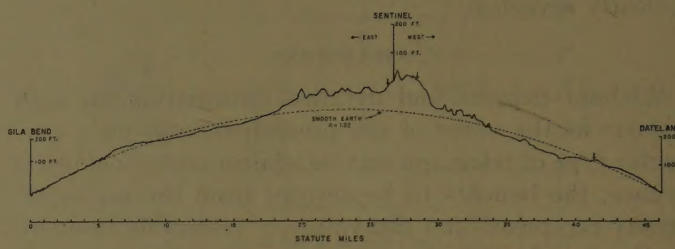

Fig. 1—Profile of Gila Bend to Dateland path.

In the present paper an attempt is made to relate a special shape of foreground terrain to a diffraction pattern noted in height-gain curves.

Experimental Site and Experimental Setup

The data presented in this paper were obtained at an experimental station located in the Gila Valley in southern Arizona. This experimental station was originally set up by the Navy Electronics Laboratory, San Diego, and a portion of the data presented was taken by the Navy Electronics Laboratory Staff. The experimental station is now under the cognizance of the Army Electronic Proving Ground, Fort Huachuca, Ariz. Three 200-foot towers on which elevator cabs were installed for hoisting antennas and associated equipment, are located at Gila Bend, Sentinel, and Dateland. Fig. 1 shows a profile of the East-West path from Gila Bend to Dateland, with the intermediate Sentinel tower indicated on the profile. Thus three paths could be set up: 1) a 46.3-mile path from Gila Bend to Dateland, 2) a 26.7-mile path from Gila Bend to Sentinel, and 3) a 19.5-mile path from Sentinel to Dateland. On path 1 the terminals are beyond line of sight for all antenna heights available on the 200-foot towers. For paths 2 and 3, on the other hand, the antennas are within line of sight except for the lower 20 or 30 feet of elevator height excursion. Later a fourth link was set up by extending the path eastward to Casa Grande, Ariz. A mobile transmitter with antenna at fixed height was set up at Casa Grande and height-gain measurements taken at Sentinel. This 83.9-mile path is dominated by a large mountain obstacle, as may be seen from the profile of Fig. 13.

For the tower terminals, antennas were installed on the face of the elevator cabs, and the receiving or transmitting equipment was installed inside the cab. Thus the

* Manuscript received by the PGAP, November 27, 1957.
† Smyth Research Associates, San Diego, Calif.

[1] M. D. Rocco and J. B. Smyth, "Diffraction of radio waves around the earth," PROC. IRE, vol. 37, pp. 1195–1203; October, 1949.

[2] J. P. Day and L. G. Trolese, "Propagation of short radio waves over desert terrain," PROC. IRE, vol. 38, pp. 165–175; February, 1950.

[3] W. S. Ament and M. Katzin, "Signal fluctuations in long-range over-water propagation," IRE TRANS. ON COMMUNICATIONS SYSTEMS, vol. CS-4, pp. 118–122; March, 1956.

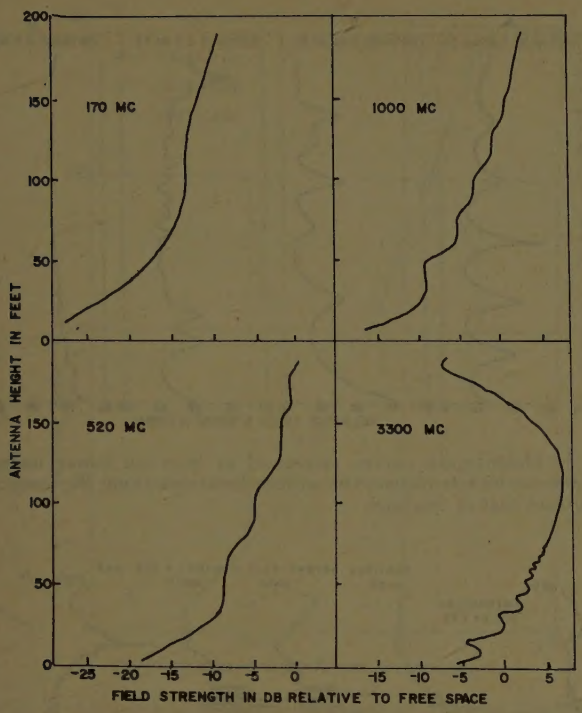

Fig. 2—Height-gain curves measured at Sentinel tower for 26.7-mile path from Gila Bend. Gila Bend terminal at fixed height of 190 feet.

field strength as a function of height could be recorded over a 190-foot height interval.

Experimental Data

Gila Bend-Sentinel Path—26.7 Miles

Some typical height-gain curves obtained at the Sentinel tower with the Gila Bend transmitter antennas at a fixed height are shown on Fig. 2 for frequencies of 170, 520, 1000, and 3300 mc. An examination of these curves indicates that a diffraction pattern suggestive of knife-edge diffraction is superimposed on the height-gain shape normally expected at these frequencies. At 3300 mc many small amplitude maxima and minima are present, with progressively closer spacing as the antenna height increases. For the other frequencies, the heights of the maxima and minima are more spread out in height as the frequency is lowered.

For a knife edge in free space the height, h, of successive maxima and minima of a knife-edge diffraction pattern is given by

$$h = \sqrt{\frac{bd\lambda n}{d - b}} \qquad (1)$$

where b is the distance from the probing antenna to the knife edge; d, the distance between the probing antenna and the source; λ, the wavelength; and n an integer which is odd for maxima and even for minima. If the diffraction phenomenon behaves geometrically like knife-edge diffraction, h should be proportional to the square root of λ, and also to the square root of n. On the other hand, if the maxima and minima are due to interference between a direct component and one reflected from a smooth reflecting ground, h would vary as the first power of λ and n according to

$$h = \frac{n\lambda}{4\psi} \qquad (2)$$

where ψ is the grazing angle of incidence of a plane wave on the ground.

Fig. 3 shows a plot of h^2 as a function of λ. For various values of n the experimental points lie on straight lines passing through the origin in agreement with (1). Fig. 4 illustrates the dependence of h on n for 3300-mc data.[4] The experimental points lie on a straight line with slope $\frac{1}{2}$ on this log-log plot, again indicating agreement with (1). If the maxima and minima were due to interference between a direct and a ground reflected component, the plot of h vs n should lie on a straight line of slope 1 rather than $\frac{1}{2}$. Thus the geometrical behavior of the diffraction effect is like that of knife-edge diffraction rather than of specular reflection.

Having noted the geometrical similarity of the data to knife-edge geometry, one can use (1) to compute the location of the apparent knife edge. However, since the reference from which height should be measured is somewhat uncertain, it seems better to recast (1) in terms of the difference in height between minima or maxima. If this is done one obtains, after solving for b,

$$b = \frac{d(h_j - h_i)^2}{d\lambda(\sqrt{n_j} - \sqrt{n_i})^2 + (h_j - h_i)^2} \qquad (3)$$

where h_j and h_i are the heights of any two maxima or minima of order n_j and n_i. Substituting values from the experimental data, an average value of b was found to be 0.47 mile. That is, the apparent knife edge should be located 0.47 mile east of the Sentinel tower. An examination of the profile shows the terrain to have a rounded drop-off rather than a sharp obstruction like a knife edge at this location.

In order to obtain a clue as to whether the terrain at this location was actually responsible for the knife-edge type of diffraction pattern, a mobile 3300-mc transmitter was set up at several points along the foreground terrain and height-gain curves recorded at the Sentinel tower. The results are shown in Fig. 5. Curve A, taken with the transmitter 0.32 mile from the Sentinel tower, has maxima and minima which are equally spaced in height; that is, h varies directly as n, as in (2), which described the geometry of an interference pattern resulting from a direct and ground reflected component. Curves B, C, and D, on the other hand, taken with the transmitter located 0.68 mile or more from the Sentinel tower, have a different character. The spacing of maxima and minima

[4] For the plots of both Figs. 3 and 4 a constant 17 feet was added to the measured heights in order to obtain better fit to straight lines. As long as the same constant is added to all heights, this does not seem unreasonable since the reference from which height should be measured and the angle of arrival of the wave is not known precisely.

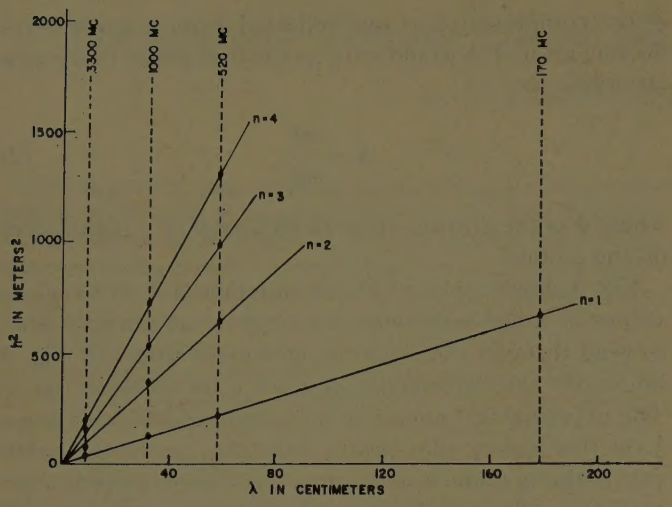

Fig. 3—Variation of square of height of maxima and minima of Sentinel height gain curves as function of wavelength. $n=1$ for first maximum, 2 for first minimum, etc.

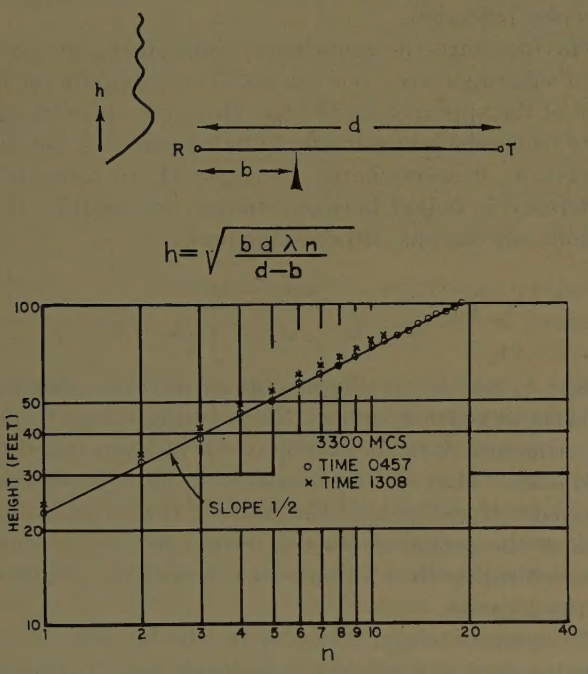

Fig. 4—Variation of height of Sentinel 3300-mc maxima and minima with the diffraction order number.

decreases with height more like knife-edge diffraction, with h proportional to the square root of n. Clearly the terrain between 0.32 and 0.68 mile is responsible for a diffraction effect which has geometrical characteristics like that of knife-edge diffraction even though the physical appearance of the terrain is smooth and rounded rather than sharp-edged.

Another facet of the effects of terrain on radio fields is the intensification of the knife-edge type diffraction pattern when meteorological conditions result in ducting phenomena. In this desert area a diurnal meteorological cycle is usually evident due to solar heating of the ground during day and radiational cooling of the ground at night.[2] This results in a nocturnal ground-based temperature inversion which reaches its maximum intensity during the early morning hours. Occasionally during the early morning hours a striking intensification of the diffraction pattern was noted, as illustrated by the height-gain curves of Fig. 6. Although the minima become much deeper, the pattern appears to be due to the same diffraction effect noted in the daytime. This is demonstrated by Fig. 4, which shows h plotted as a function of n. On this plot the crosses are daytime data and the circles, nighttime points. Both sets of data lie on straight lines with slope of $\frac{1}{2}$, but the nighttime diffraction pattern is shifted downward slightly. No doubt this is due to the fact that the additional refractive bending of the wave changes the angle of arrival slightly, thus moving the whole diffraction pattern slightly downward.

The deepening of the minima are believed to be attributable to a second wave component which is reflected from the section of terrain (Fig. 1) between 10 and 17 miles from Gila Bend. This component interferes with the direct wave only under conditions of strong surface ducting. At heights where destructive interference between the two waves reduces the field, the knife-edge oscillations become a larger fraction of the total field, thus increasing the depth of the knife-edge minima.

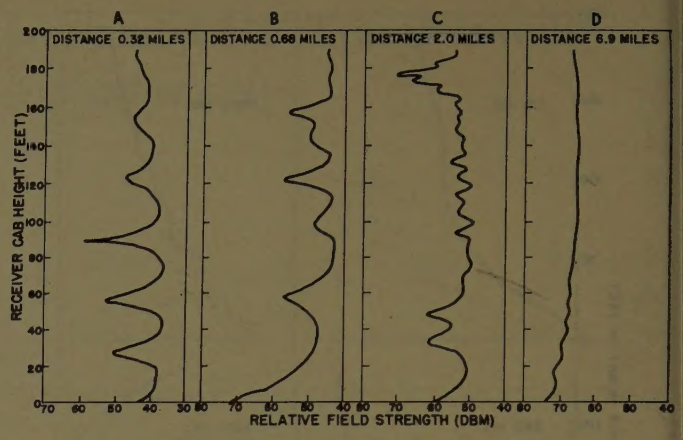

Fig. 5—Height-gain curves measured at Sentinel tower using the 3300-mc mobile transmitter at four locations along the foreground terrain east of Sentinel.

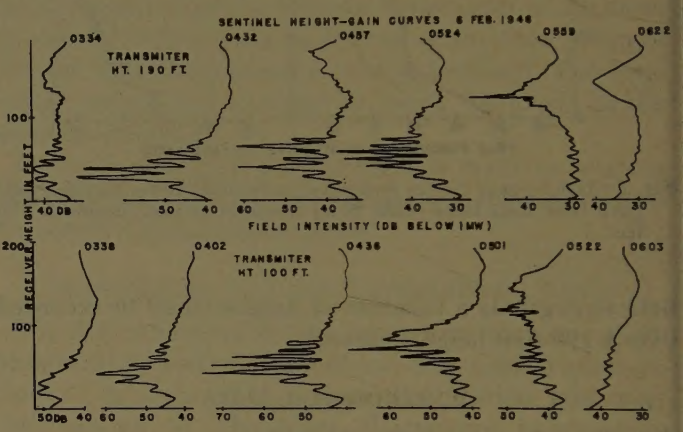

Fig. 6—Nighttime 3300-mc Sentinel height-gain curves for Gila Bend-Sentinel path.

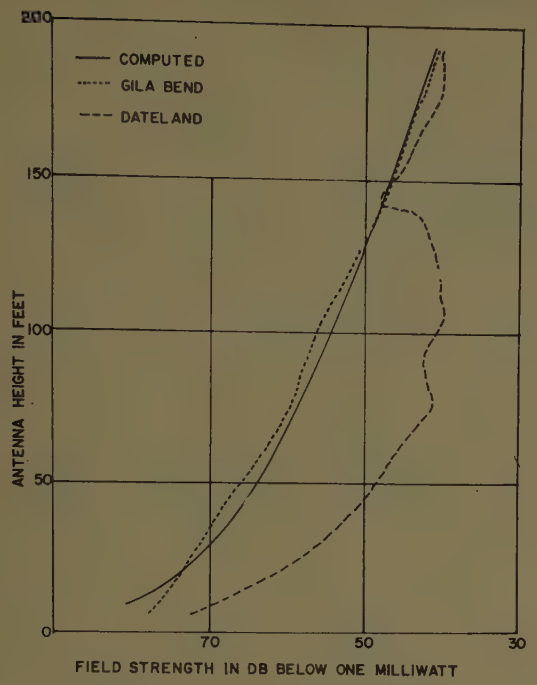

Fig. 7—Daytime Gila Bend and Dateland 3300-mc height-gain curves for Gila Bend-Dateland 46.3-mile path.

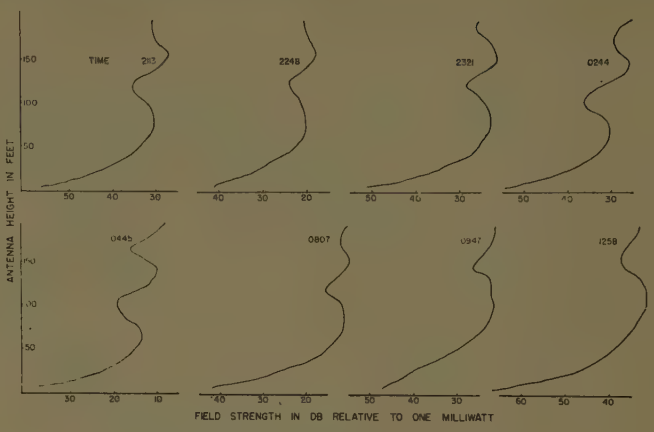

Fig. 8—Dateland 3300-mc height-gain curves for Gila Bend-Dateland 46.3-mile path.

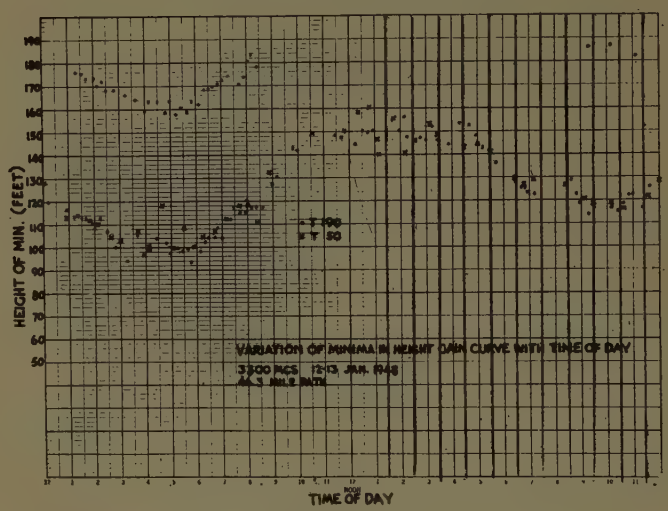

Fig. 9—Variation of height of Dateland diffraction minima with time of day.

Gila Bend-Dateland Path—46.3 Miles

Typical daytime height-gain curves obtained for 3300-mc transmissions over the 46.3-mile Gila Bend-Dateland path are shown in Fig. 7. The dashed curve is a height-gain curve taken at Dateland with the Gila Bend terminal at a fixed height of 194 feet. The dotted curve is a Gila Bend height-gain curve with the Dateland terminal at a fixed height of 194 feet. The solid line is a theoretical curve computed by use of standard diffraction theory for a smooth spherical earth. Since the atmosphere is essentially standard in the daytime in Arizona, both measured height-gain curves should agree with the computed curve if the path were truly spherical. The Gila Bend curve is quite similar to the theoretical curve, but the Dateland height-gain shows a bulging maximum near 100 feet and minimum at 140 feet. During the nighttime, when the nocturnal duct forms, the height-gain curve at Dateland varies considerably, as may be seen for the series of height-gain curves shown in Fig. 8. During the night and early morning hours, when the nocturnal duct is most intense, the maximum and minimum visible on the daytime height-gain curves drop in height and a second maximum and minimum are present in the 190-foot height interval. After sunrise the pattern returns to the normal daytime condition indicated by the curve for 1258. This effect is shown more clearly in Fig. 9, which is a plot of the height of the minima as a function of time of day for a 24-hour cycle. The height of the first minimum is fairly constant during the day and drops during the night, reaching a low value of 100 feet in the early morning hours. The second minimum drops in height during the night in synchronism with the first minimum. In this case the pattern is more spread out in height than was the case for the 3300-mc pattern at Sentinel. Thus if the phenomenon is similar to that at Sentinel, the apparent knife-edge location must be more distant. With the apparent knife edge located at greater distance, changes in angle of arrival due to changing refraction would shift the diffraction pattern up and down to a greater degree than was noted at Sentinel. Since a smaller portion of the diffraction pattern appears on the 190-foot height interval which is probed, it is more difficult to determine if a similarity to a knife-edge diffraction pattern exists. However, for the nighttime data, when more maxima and minima are present, a plot of h vs n can be made, as shown on Fig. 10. Points taken from the height-gain curves on Fig. 8, at time 0244, 0445, and 0805, are shown in Fig. 10. Each set of points lies quite close to a line with slope $\frac{1}{2}$ on the log-log plot, indicating a dependence of h on n similar to knife-edge diffraction.

If (3) is again used for values from the Dateland experimental data, an apparent knife-edge location 4.7 miles from the Dateland tower is obtained. In this calculation d was taken as the distance from the Dateland tower to the hill just west of Sentinel (see profile, Fig. 1) which is at the horizon.

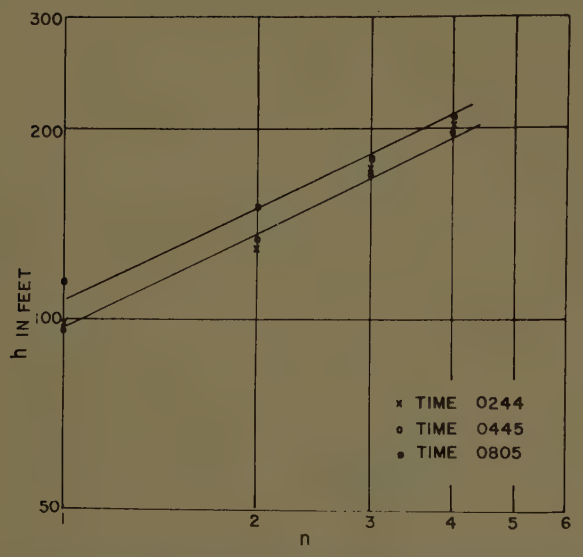

Fig. 10—Variation of height of Dateland 3300-mc maxima and minima with the diffraction order number.

Thus, just as in the East Sentinel foreground effect, the diffraction phenomenon is geometrically like knife-edge diffraction. However, the amplitude of the signal variations with height are much greater than knife-edge theory allows.

Sentinel-Dateland Path—19.5 Miles

An examination of the profile of Fig. 1 shows that a rounded section of terrain is present west of the Sentinel tower. If the diffraction patterns described previously are attributable to the rounded shape of the foreground terrain, one would expect a similar result from the rounded section west of Sentinel. To check this point, a 1725-mc link was set up on the Sentinel-Dateland path and height-gain curves were obtained at Sentinel for different fixed terminal heights at Dateland. Fig. 11 shows daytime height-gain curves at Sentinel with the Dateland terminal at different fixed heights. Most of the curves show two maxima and two minima which stay about fixed in height as the Dateland terminal height is set at different values. Only for the Dateland terminal at the greatest height, 197 feet, is this pattern not clearly present. For nighttime data, Fig. 12, the situation is similar except that the pattern is shifted downward in height slightly and the minima are deeper. Thus most of the height-gain curves appear to show a diffraction pattern similar to those previously described. If the location of the apparent knife edge is computed, as was done before using (3), a location 1.7 miles west of the Sentinel tower is obtained as a median value. This location is found on the rounded bulge in a position comparable to that in the other two cases.

Casa Grande-Sentinel Path—83.9 Miles

A profile of this path is shown on Fig. 13. Propagation studies over this path were made for about a one-week period to ascertain whether the foreground terrain ef-

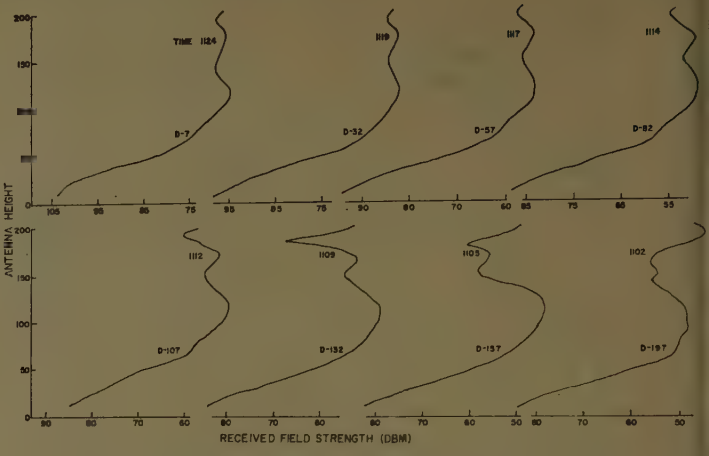

Fig. 11—Daytime 1725-mcs Sentinel height-gain curves for Sentinel-Dateland path.

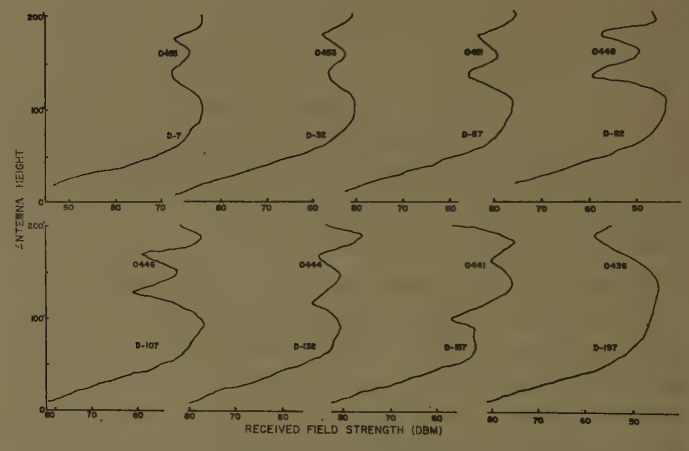

Fig. 12—Nighttime 1725-mc Sentinel height-gain curves for Sentinel-Dateland path.

fects noted at Sentinel would be present on this 83.9-mile path as well as on the much shorter Gila Bend-Sentinel path. As may be seen from the profile, this path is dominated by a large mountain obstacle, the Maricopa Mountains. The arrival angle of the wave reaching Sentinel should be a little greater than for the short path. The Casa Grande antenna was located at a fixed height of 10 feet and height-gain measurements were made at Sentinel. Over this path the general level of the signal seemed to be dominated most of the time by diffraction over the mountain obstacle rather than by tropospheric scattering. Occasionally rapid fluctuations characteristic of a scattered field signal were present, but most of the time they were absent. Typical height-gain curves are shown in Fig. 14. The maxima and minima of a characteristic knife-edge type diffraction pattern are clearly visible on the curves. The plot of h as a function of n, shown on Fig. 15, again indicates that the diffraction pattern obtained is geometrically like knife-edge diffraction but the amplitude variations are much larger than knife-edge theory predicts. A calculation of the location of the apparent knife edge would place the knife edge 0.39 mile east of the Sentinel tower,

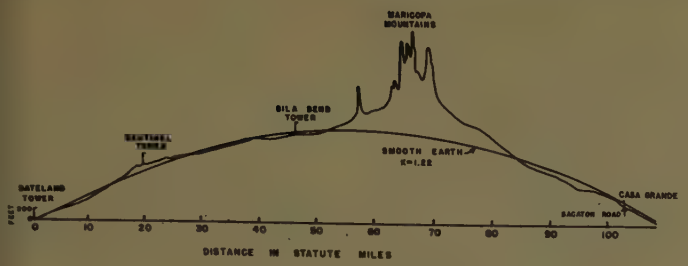

Fig. 13—Profile of Casa Grande to Sentinel path.

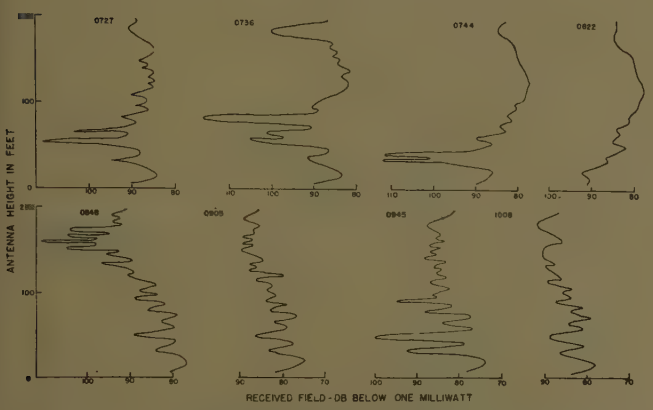

Fig. 14—Sentinel 1800-mc height-gain curves for Casa Grande to Sentinel 83.9-mile path.

compared to a value of 0.47 mile obtained from the previous data on the Gila Bend-Sentinel path. However, on the Casa Grande-Sentinel path, the energy arrives at a little higher angle due to the presence of the mountain obstacle, and one might expect the apparent knife edge to appear to be closer to the tower. This point will be discussed in more detail later.

General Summary of Experimental Results

The results from tests on the four paths described show diffraction effects which can be attributed to the shape of the foreground terrain on each of the paths. In order to show the similarities in the three sections of foreground, profiles plotted to expanded scales are indicated on Fig. 16. The Dateland foreground profile is at the top of the figure, the foreground west of Sentinel in the center, and that east of Sentinel at the bottom. The West-Sentinel profile distance scale is expanded three times the Dateland scale. The East-Sentinel profile is plotted on a distance scale expanded tenfold, relative to the Dateland plot. The arrows indicate the location computed for the apparent knife edge and in each case this turns out to be in the same general position on the rounded foreground profiles. It is logical to conclude that the three diffraction effects are phenomenologically alike. The similarity may be noted in another way by examining the Dateland 3300-mc height-gain curve of Fig. 7 and the 170-mc Sentinel curve of Fig. 2. The two curves are quite alike in general character, indicating that the diffraction effect is similar in each case except for geometric scale.

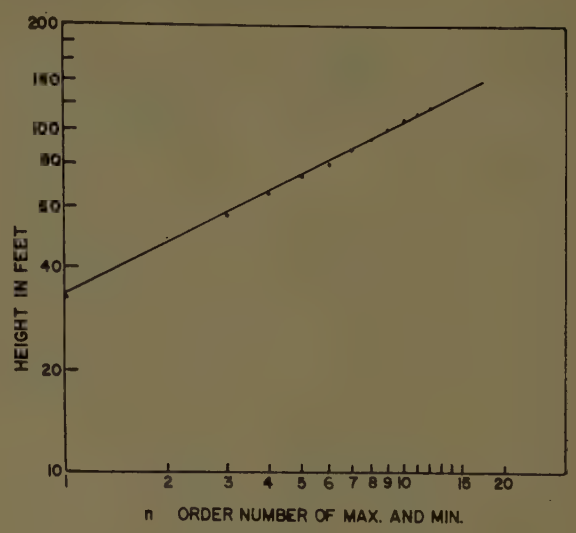

Fig. 15—Variation of height of Sentinel 1800-mc maxima and minima with diffraction order number.

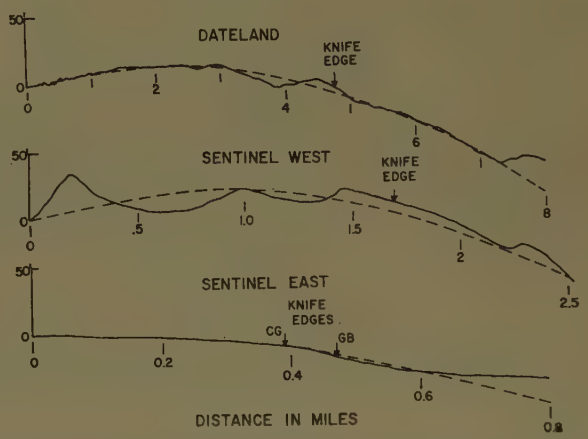

Fig. 16—Expanded scale plot of Dateland, Sentinel West, and Sentinel East foreground terrain profiles.

Since the geometry of the diffraction phenomenon from the rounded foreground apparently coincides with knife-edge geometry, it would be convenient to have an empirical method of estimating the location of the apparent knife edge. If this location is known, the height of the first maximum could be computed for a given wavelength to insure siting an antenna at optimum height.

In developing a method for predicting the location of the knife edge, it was felt desirable to express the distance from terminal to knife edge, b, in terms of parameters describing the shape of the terrain bulge and the angle of incidence of the energy on the terrain. Fig. 17 illustrates the concept chosen for this purpose. A cylinder of radius R is fitted to the actual foreground terrain profile. Radii are drawn from the center of curvature of the cylinder to 1) the terminal location, 2) the knife-edge location, and 3) normal to the incoming rays. The angles α and θ are defined as shown. Then the angular distance from terminal to knife edge $b/R=\alpha+\theta$. For the terrain features studied thus far, the measured parameters b, R, and α are indicated in Table I.

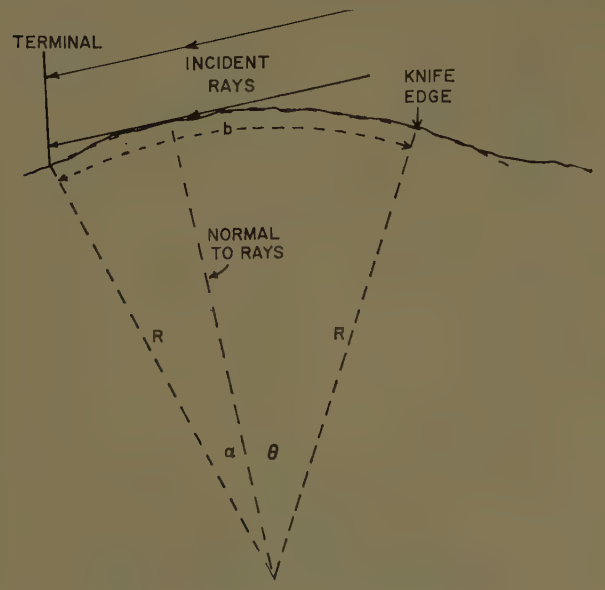

Fig. 17—Geometry of empirical foreground diffraction model.

TABLE I

Terrain Feature	R Feet $\times 10^{-6}$	b Feet	b/R (mr)	α(mr)	θ(mr)	$(1/R - 1/a)$ 10^6/Feet
Dateland	4.7	25,000	5.3	2.5	2.8	0.174
Sentinel West	0.49	9000	18.5	9.8	8.7	2.02
Sentinel East (to Gila Bend)	0.15	2500	16.7	1.2	15.5	6.63
(to Casa Grande)	0.15	2100	13.7	−1.4	15.1	6.63

From these parameters, θ has been calculated for each feature, together with $(1/R-1/a)$, (where a is the effective earth's radius). The effect of increasing ray inclination causing a closer knife-edge location is illustrated in the bottom two lines of the table. Although the angular distance to the knife edge is reduced 3 mr (16.7−13.7) in the mountain obstacle path, the increased ray inclination of 2.6 mr almost completely compensates this effect, such that θ remains essentially constant. If one now plots θ vs $(1/R-1/a)$, a straight line relationship is found on the log-log plot of Fig. 18. The parameter $(1/R-1/a)$, rather than R itself, was chosen to designate the shape of the bulge, since this parameter becomes zero as the bulge flattens down to the smooth spherical earth. Since θ should also become zero in this case, the log-log plot would be expected to be linear over a wider range of bulge radii than if R itself is used.

Using this empirical curve, one can now predict the location of a knife edge on any terrain bulge of radius R and ray inclination α. For example, if the bulge radius R is 1 million feet, $(1/R-1/a)$ would be $(1-0.039)$ $=0.96\times10^{-6}$/feet. According to Fig. 15, θ is 6.4 mr. If the ray inclination is 2 mr, then $b/R=8.4$ mr, or $b=8400$ feet. It remains to be seen whether this model is sufficiently general to cover most foreground terrain bulges. Work on similar features is continuing for the purpose of checking this point.

In order to obtain some indication of the practical importance of the foreground diffraction effects which have been described, the 3300-mc data available on the 46.3-mile Gila Bend-Dateland path were examined statistically. The data for this analysis were obtained

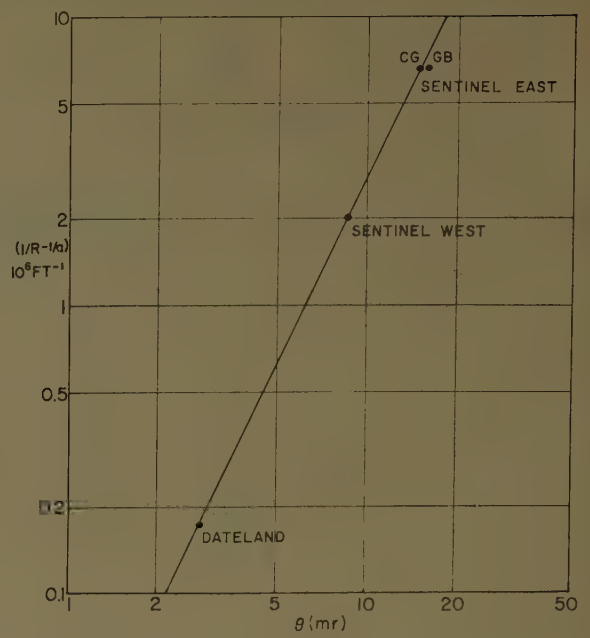

Fig. 18—Experimental relationship between $(1/R-1/a)$ and θ.

from a series of height-gain curves similar to those shown on Fig. 7. A height-gain measurement was made by recording the field strength as the Gila Bend terminal was moved in height with the Dateland terminal at a fixed height of 194 feet. Immediately thereafter the Gila Bend terminal was fixed at 194 feet and the Dateland terminal moved in height. Most of the Gila Bend height-gain curves agreed with the computed smooth earth curve and exhibited no foreground diffraction pattern. The Dateland curves, on the other hand, showed a consistent maximum in field strength at about 70 feet. The histogram of Fig. 19 was obtained by taking the ratio of the field strength received on the following two paths: 1) the Gila Bend terminal at 190 feet and Dateland at 70 feet; 2) the Gila Bend terminal at 70 feet and Dateland at 190 feet. Three histograms are shown on Fig. 19, one for daytime data with no duct present, a second with nighttime data when a duct was present, and a third with all of the data combined together. For a spherical earth the histograms should, of course, peak up at 0 db. However, the plots show that the field on the Gila Bend 190-Dateland 70 path consistently exceeds the field on the Gila Bend 70-Dateland 190 combination. For nonducting conditions the bias in favor of the Gila Bend 190-Dateland 70 is most pronounced, averaging close to 15 db.

If one terminal is set at a very low height of 5 feet instead of 190 feet, the results shown on Fig. 20 are obtained for the other terminal at either 50 or 100 feet. This shows the effect of the Dateland foreground diffraction pattern. By properly siting the antenna on the first maximum a diffraction enhancement is obtained due to the diffraction effect of the rounded foreground terrain.

On the 83.9-mile Casa Grande-Sentinel path the 1800-mc data serve to illustrate the effect of the foreground terrain east of the Sentinel tower for a link having rather low terminal heights. Fig. 21 shows a summary of the ratio of the fields for an antenna height at

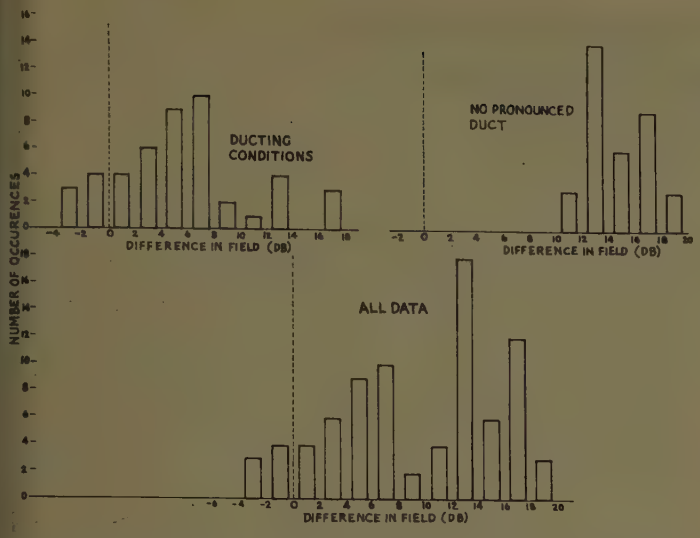

Fig. 19—Histograms of ratio in db of field received on Gila Bend 190 feet-Dateland 70 feet path to that received on the Gila Bend 70 feet-Dateland 190 feet path.

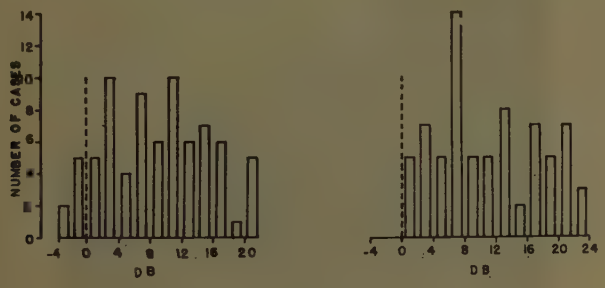

Fig. 20—(a) Histogram of ratio in db of field received on Gila Bend 5 feet-Dateland 100 feet path to that received on Gila Bend 100 feet-Dateland 5 feet path. (b) Histogram of ratio in db of field received on Gila Bend 5 feet-Dateland 50 feet path to that received on Gila Bend 50 feet-Dateland 5 feet path.

first maximum as compared to that at the first minimum of the foreground diffraction pattern. This is given in the form of a distribution curve which shows, for example, that 50 per cent of the time the signal for an antenna height on the maximum (19 feet) is 9 db higher than on the minimum (33 feet) and 10 per cent of the time it is 17 db higher. Furthermore the fading was more severe with the antenna at the height of the minimum than of the maximum. This point is illustrated in Fig. 22, which shows a sample of the signal record for antenna heights of 6 feet (below first maximum), 21 feet (near first maximum) and 31 feet (near first minimum). At the minimum the fading range is about 15 db and on the maximum less than 5 db. On this particular day the received signal appeared to be influenced by 3 different mechanisms: 1) diffraction over the dominant mountain obstacle, 2) scattering in the lower troposphere, and 3) diffraction due to the foreground terrain near Sentinel. Most of the time the influence of the scattered field component was less evident.

Conclusions

The experimental results which have been summarized indicate that gently rounded sections of foreground terrain can cause marked diffraction effects at UHF

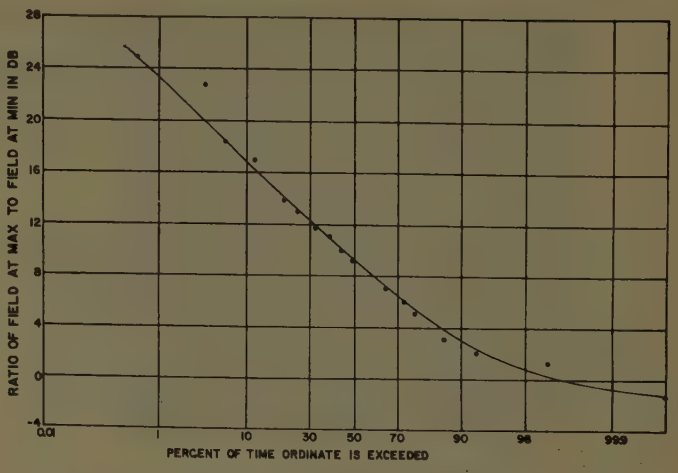

Fig. 21—Distribution curve of ratio of field at first maximum to that at first minimum. Casa Grande-Sentinel path—1800 mc.

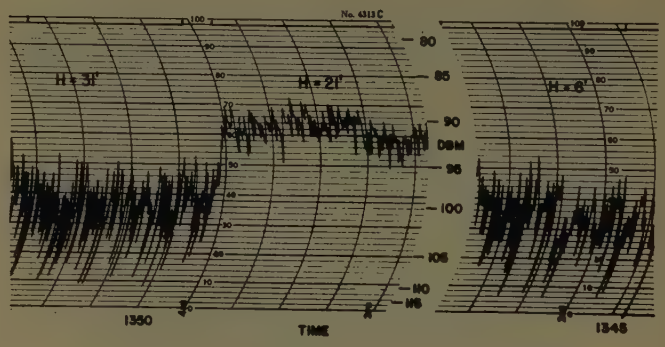

Fig. 22—Sample field strength record at Sentinel showing time fluctuations of 1800-mc signal with the antenna below the first maximum (6 feet), on the first maximum (21 feet), and on the first minimum (31 feet).

frequencies. The diffraction phenomena show a striking geometrical similarity to knife-edge diffraction. However, the amplitude of the spatial variations of field strength are considerably greater than for knife-edge diffraction.

Proper siting of antennas overlooking such foreground terrain features can lead to sizable diffraction enhancement of the received signal.

An empirical method for predicting the foreground diffraction geometry from foreground terrain profiles having the rounded shape has been devised. If this method can be verified experimentally for other cases, it should be useful as an aid in proper siting of terminals of UHF links.

Changing refraction due to meteorological variations can alter both the position in height and intensity of the diffraction pattern. The height variation due to refraction changes becomes less as the distance of the apparent knife edge from the terminal becomes smaller.

Acknowledgment

The authors are indebted to the Navy Electronics Laboratory for supplying a portion of the data utilized in this paper.

The work was sponsored by the Signal Communications Department of the Army Electronic Proving Ground, Fort Huachuca, Ariz.

A Rapid Beam-Swinging Experiment in Transhorizon Propagation*

ALAN T. WATERMAN, JR.†

Summary—**By using a broadside phased array for an antenna, a narrow beam can be swung rapidly and in quick succession through a limited sector by fast control of the phasing, rather than by movement of the entire antenna structure. This technique is used at the receiving end of a 101-mile beyond-the-horizon transmission path in order to probe the portion of the troposphere through which the signal is propagated. At the frequency employed of 3.12 kmc, a 0.49-degree beam is swung in azimuth through a 4.2-degree sector each tenth of a second.**

A variety of phenomena are observed with this technique which have not been directly apparent in slower beam-swinging experiments. The beam-broadening effect attributed to atmospheric scattering is not always evident on any one sector scan. However, the change from scan to scan is frequently rapid enough so that a time average would show the broadening. At times the scan-to-scan changes are systematic and show a continuity indicative of a motion of the scattering or reflecting regions; in some cases this motion is too rapid to be accounted for by transport of air, thus implying a wave motion rippling through the atmosphere. At other times the atmospheric structure is too fine to be resolved by the beamwidth employed, and the time variations are too rapid to reveal a continuity from one scan to the next.

NARROW-beam antennas have been used very effectively as devices for probing the atmosphere in transhorizon propagation experiments.[1–7] The unmanageable nature of the large physical structure required for a narrow beam is largely circumvented if a phased array is used and a mechanism provided for rapid variation of the phase of each radiating element.

The experiment described here utilizes such an array for the receiving antenna. A 3000-mc circularly polarized signal is transmitted, with sufficiently wide beamwidth (about 5 degrees) to illuminate the pertinent portion of the atmosphere. The receiving antenna[8] is an eight-element broadside array (Fig. 1). Each element in the array consists of an offset parabolic reflector and helical feed. The helix in each feed is connected to a syncrodrive so that the desired phase shifting can be accomplished by mechanical rotation of the helix about its axis. The syncros then are driven at multiple rates from a centrally located gear train. Thus, the over-all rate of beam swinging is controlled by the speed of the master motor driving the gear train.

Fig. 1—Phased array used as the receiving antenna in rapid beam-swinging experiment.

The horizontal beamwidth of the entire antenna depends on the lateral length of the over-all array. At 3000 mc, a 30-foot-long array has a beamwidth of about ½ degree. In the array which has been constructed each element (consisting of reflector and feed) is mounted along a pipe supported on an A-frame structure, so that the element can be slid laterally along the pipe, thus affording an adjustment of the length of the array and consequently of the width of the antenna pattern. The interval between successive principal maxima in the array pattern depends on the spacing between adjacent elements in the array or, for an array of fixed length, on the number of elements. This angular interval is also the sector over which the array can scan without ambiguity. The sector of interest in these transhorizon propagation experiments covers only 4 or 5 degrees in azimuth. Consequently only eight elements are needed in the array and these may then be placed at a 4-foot spacing. Utilization of a parabolic reflector in each element does not affect the array factor over this

* Manuscript received by the PGAP, June 30, 1958. This paper was presented at the URSI meeting, Washington, D. C.; April 26, 1958. The research reported was made possible through the support of the U. S. Army Signal Corps, under Contract DA36(039)SC-73151.

† Stanford Electronics Labs., Stanford University, Stanford, Calif.

[1] J. H. Chisholm, P. A. Portmann, J. T. deBettencourt, and J. F. Roche, "Investigations of angular scattering and multipath properties of tropospheric propagation of short radio waves beyond the horizon," PROC. IRE, vol. 43, pp. 1317–1335; October, 1955.

[2] W. S. Ament and M. Katzin, "Signal fluctuations in long-range overwater propagation," IRE TRANS. ON COMMUNICATIONS SYSTEMS, vol. CS-4, pp. 118–112; March, 1956.

[3] A. T. Waterman, Jr., N. H. Bryant, and R. E. Miller, "Some observations of antenna beam distortion in transhorizon propagation," IRE TRANS. ON ANTENNAS AND PROPAGATION, vol. AP-5, pp. 260–266; July, 1957. Also, Stanford Electronics Labs., Stanford, Calif., Tech. Rep. No. 461-2; February 25, 1957, under Signal Corps Contract DA-36(039)SC-63189.

[4] A. T. Waterman, Jr., "A Note on Microwave Reception Well Beyond the Horizon," Stanford Electronics Labs., Stanford, Calif., Tech. Rep. No. 8, October 15, 1953, under Contract Nonr 225-10.

[5] J. H. Chisholm, J. F. Roche, and W. J. Jones, "Experimental Investigations of the Angular Scattering and Multipath Delays for Transmission Beyond the Horizon," presented at URSI meeting, Washington, D. C.; May 22–25, 1957.

[6] L. H. Doherty, "A 216-Mile 2700-MC Scatter Link," presented at URSI meeting, Washington, D. C.; May 22–25, 1957.

[7] W. H. Kummer and D. C. Hogg, "Characteristics of Signals Received on a Large Aperture Antenna in Propagation Beyond-the-Horizon," presented at URSI meeting, Washington, D. C.; May 22–25, 1957.

[8] R. E. Miller, G. K. Durfey, and W. H. Huntley, Jr., "A Rapid-Scanning Phased Array for Propagation Measurements," Stanford Electronics Labs., Stanford, Calif., Tech. Rep. No. 461-5; July 30, 1958, under Signal Corps Contract DA36(039)SC-73151.

limited sector but does increase the capture area of the over-all antenna. It also establishes the vertical beamwidth, in this case about 5 degrees.

For operation in this frequency range, all the component parts are of convenient physical size. The helices[9] consist of 3.4 turns of No. 12 copper wire and are 7.8 cm long. The half-power beamwidth for each helical feed is 60 degrees, a convenient value for illuminating the offset section of paraboloidal reflector. This offset places the feed itself and associated syncrodrive out of the path of the reflected radiation and in a conveniently accessible position.

To provide a continuous azimuthal scan, the helical feeds are rotated at multiple rates—or rather, the right four helices are rotated at odd multiple rates in one sense and the left four at corresponding rates in the opposite sense. With this procedure, a rotation rate of 2100 rpm for the outermost helices corresponds to a scan rate in which one principal maximum moves on and the next moves into its place in one-tenth second (*i.e.*, ten sector scans per second). It is to be noted that this beam swinging is not a back-and-forth sector scan; the principal maxima in the array factor rotate uniformly like the spokes of a wheel and move one after another through the sector being scanned.

At the frequency employed, 3.12 kmc, the horizontal beamwidth of the array and the azimuthal sector scanned, as measured on a line-of-sight test range, are 0.49 degree and 4.2 degrees, respectively.

This equipment has been employed in propagation measurements which, though preliminary, are nevertheless startling enough in their implications to warrant reporting promptly. A CW transmitter was located 101 miles distant from the receiving array, well beyond line of sight, and the system response was observed as the receiving antenna beam scanned in azimuth through the great-circle bearing to the transmitter.

In the accompanying figures, which are pictures of an oscilloscope face, signal level is displayed as a vertical deflection and the azimuth in which the beam is pointing is synchronized with the horizontal sweep. Fig. 2 shows the response of this antenna system to a low-power test transmitter within the line of sight of the receiving location. It serves to illustrate the beamwidth (0.49 degree) and sidelobe level (better than 10 db down) of the array. It also provides an azimuth reference for the sector scan. The ten divisions of horizontal displacement in the figures correspond to the 4.2-degree sector. On this scale, the great-circle bearing to the 101-mile distant transmitter (not to the test source in Fig. 2) is 7.2 divisions from the left-hand edge.

Fig. 3 is an example of receiving-system response to a signal propagated over the 101-mile path. There the display is the same, except that a raster containing alternate antenna sector-scans is employed. Thus, each

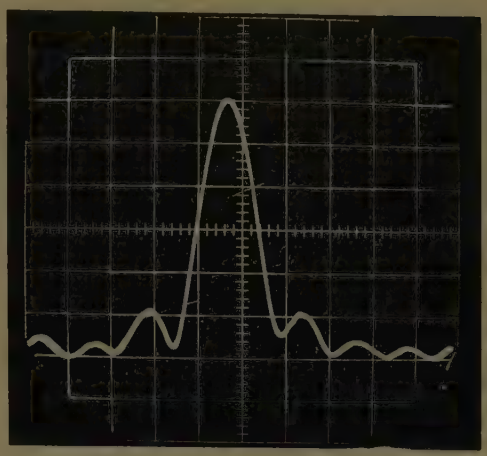

Fig. 2—Measured antenna pattern of the array over a 4.2-degree sector.

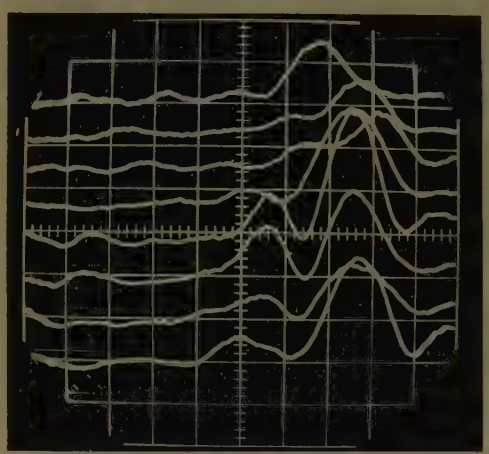

Fig. 3—Raster display of receiving-system response to 101-mile-distant transmitter. Each azimuth scan covers 4.2 degrees (10 divisions in the figures) in 0.1 second; successive scans displayed are 0.2 second apart. Great-circle bearing to transmitter is 7.2 divisions from left.

scan consumes one tenth of a second, but there is one fifth of a second between successive scans in the raster. It will be noticed that the effective antenna pattern obtained via the atmospherically scattered signal varies rapidly from scan to scan. The beam-broadening effect attributed to random scattering[1,3] is not very marked on any one scan, but if a succession of scans is averaged, the shift in angle of arrival plus the apparently discrete off-path contributions (which show up here looking like exaggerated sidelobes) result in considerable beam broadening.

An example in which there appears to be a small number of discrete scatterers which change quite rapidly is shown in Fig. 4. A slower beam-swinging experiment would not reveal this fine structure; only an average broadening would be observed.

The predominant characteristic evident in Fig. 5 is the rapid and continuous motion of one discrete scatterer. Such a motion, of course, does not necessarily imply a physical translation at this speed (which would correspond roughly to 600 or 800 mph), but might be caused by a wave motion in a reflecting layer.

By way of contrast, Fig. 6 shows a constant pattern

[9] W. H. Huntley, Jr., "A Helical Microwave Antenna Feed," Stanford Electronics Labs., Stanford, Calif., Tech. Rep. No. 461-3; September 20, 1957, under Signal Corps Contract DA36(039)SC-73151.

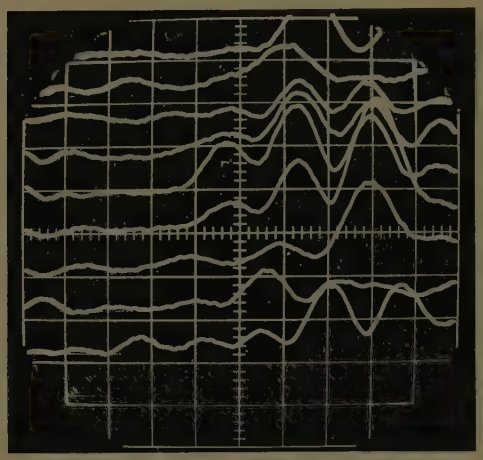

Fig. 4—Sample of received signal. (See Fig. 3 for interpretation.)

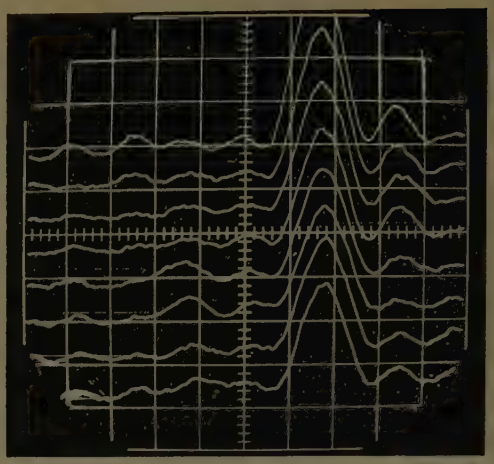

Fig. 6—Sample of received signal. (See Fig. 3 for interpretation.)

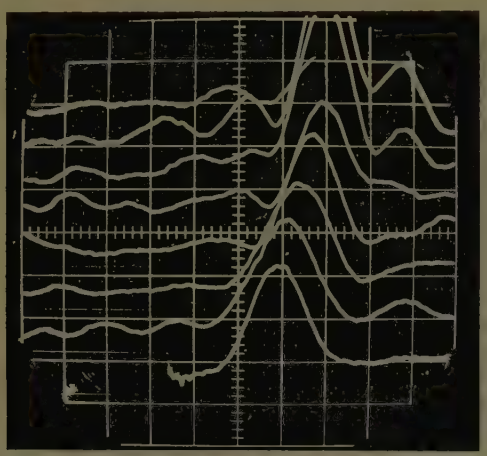

Fig. 5—Sample of received signal. (See Fig. 3 for interpretation.)

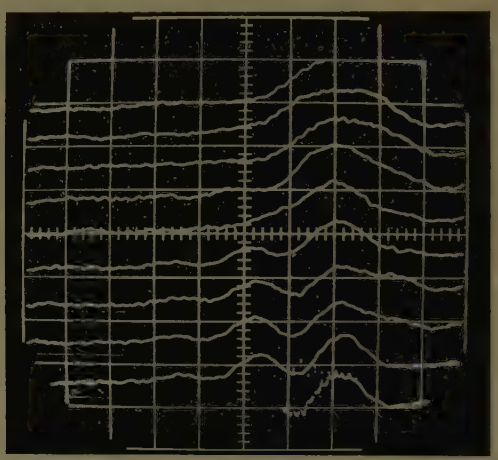

Fig. 7—Sample of received signal. (See Fig. 3 for interpretation.)

with very little beam broadening. This constancy, when observed, occurred at night, in contrast to the more wildly fluctuating patterns seen during daytime.

A final example has been selected for Fig. 7 in which several of the sweeps show an instantaneous beam broadening. This type of pattern, which so far has not been observed frequently, might be what one would expect if there were a large number of small incoherent scatterers.

These figures are samples of observations which have been made recently and have been repeated sufficiently to establish their reality. A detailed analysis of the results has not yet been undertaken. Nevertheless, some pertinent remarks can be made.

There are times when the antenna beam, though broad in elevation and only moderately narrow in azimuth, appears to have sufficient resolution to distinguish discrete scatterers. (The term "scatterer" is used here in its broadest sense; it might well refer to an appropriately oriented portion of a partially reflecting layer.) These scatterers, in such cases, are small in number (one to four); their resolvability implies a spatial separation of at least 500 to 1000 feet. At other times, the scatterers are not resolved, and few conclusions can be drawn at the moment.

Frequently, particularly in the daytime, the atmosphere changes structure in one fifth of a second to such an extent that little continuity can be found in the changes. In such cases one cannot distinguish a random type of turbulent process from a systematic wave motion. At other times, the one-fifth second interval between scans is sufficiently short to establish a continuity of change from one situation to another. In these cases, there are many instances in which the apparent motions are more rapid than can reasonably be accounted for in terms of tropospheric winds; a wave motion of some sort is implied, such as ripples along an interface.

Much of the beam broadening does not occur instantaneously but shows up in a time average owing to the rapid changes in the scattering or reflecting centers.

Acknowledgment

The author expresses his gratitude to R. E. Miller for his competent direction of the construction and operation of the array as well as other equipment, both transmitting and receiving. In addition, thanks are due other members of the Stanford Electronics Laboratories who took an active part in this work: W. H. Huntley, Jr., G. K. Durfey, D. B. Coates, C. L. Liston, and P. Brunetti.

Effect of Mountains with Smooth Crests on Wave Propagation*

I. P. SHKAROFSKY†, H. E. J. NEUGEBAUER†, AND M. P. BACHYNSKI†

Summary—**A new method of solving the problem of diffraction of EM waves by the smooth crest of a perfectly reflecting cylindrical mountain has been previously reported.[1] This paper presents the results in a form more suitable for practical applications. The theory is extended, and good agreement with model experiments is obtained for scattering angles up to 5 degrees. The procedure for including the effects of reflections from the ground on either side of the mountain is also indicated. A few examples illustrate cases encountered in practice, and exhibit effects up to 8 db compared with knife-edge diffraction.**

I. Introduction

In a previous paper,[1] the problem of diffraction of EM waves by a mountain with a smooth crest of approximately cylindrical shape has been solved and has been shown to give good agreement with measurements for small scattering angles. In that theory, additional halo terms were added to the usual knife-edge term to account for the effect of the smooth crest of the mountain. The appropriate polarization effects were obtained using coefficients previously determined by Fock.[2] The power behind a mountain agreed well with model experiments at K-band frequencies for a wide range of distances, radii of curvature, and a narrow range of angles of diffraction.

This paper presents numerical tables and graphs which are useful for quick calculation. The functions that determine the real and imaginary parts of the halo terms are tabulated. The real and imaginary parts of the halo and knife-edge terms are also plotted in graphs that serve to simplify calculations. These real and imaginary parts, rather than the absolute values, are required for calculating the additional effect of reflecting ground on either side of the mountain. This is accomplished in the usual manner[3] by assuming that the reflected waves from the ground originate from virtual images. The field is thus propagated in four ways and the sums of the real and imaginary parts of these four contributions are required to calculate the received power.

When the ground has no effect on the propagation and when diffraction occurs only from a smooth crest of a mountain, the real and imaginary parts of the knife-edge and halo terms can be combined to express the power as a function of two universal parameters, X and Z. These variables[4] are defined by

$$X = \psi_0(2ka)^{1/3}, \qquad Z = \psi_0(2kd/\pi)^{1/2} \tag{1}$$

where $2\psi_0$ is the angle of diffraction, $k = 2\pi/\lambda$, λ = wavelength, a is the radius of curvature at the crest of the mountain, and d is the harmonic mean between receiver and transmitter distances from the mountain. This will be defined explicitly later.

Comparisons of theory and experiment were given only for small diffraction angles up to 1.5 degrees.[1] It is now shown that experimental results agree up to angles of 5 degrees and in some cases 10 degrees, depending on the radius of curvature. Although the largest experimental value of ka is only 250, there is reason to believe that even better agreement is obtainable for larger ka. The theory is assumed to hold for all ka. The theoretical graphs of power vs scattering angle are represented in a universal manner by plotting power vs X for various (X/Z).

Finally, some numerical examples are given showing the ratio of received power behind a mountain with a smooth crest as compared to a knife-edge mountain.

II. Basis of Theory

The electric field diffracted by a smooth cylindrical mountain is given by (2) to (5), which are derived from (23) and (27) of the previous paper.[1] The field can be written as the sum of the real and imaginary components (K_{re}, K_{im}) of the knife-edge contribution and the components (H_{re}, H_{im}) of the halo contribution. These four components are functions of the two universal parameters X and Z.

$$E = [1/2(d_1+d_2)] \exp[-jk(d_1+d_2)(1+\psi_0^2/2)] \times \{[K_{re}(Z)+jK_{im}(Z)]+(X/Z)[H_{re}(X)+jH_{im}(X)]\} \tag{2}$$

where

$$K_{re}(Z) + jK_{im}(Z) = \{1 - (1+j)[C(Z) - jS(Z)]\} \exp(j\pi Z^2/2) \tag{3}$$

$C(Z)$ and $S(Z)$ are the Fresnel integrals

$$C(Z) = \int_0^Z \cos(\pi\xi^2/2)d\xi, \quad S(Z) = \int_0^Z \sin(\pi\xi^2/2)d\xi. \tag{3a}$$

* Manuscript received by the PGAP, February 25, 1958.
† Res. Lab., RCA Victor Co., Ltd., Montreal, Can.

[1] H. E. J. Neugebauer and M. P. Bachynski, "Diffraction by smooth cylindrical mountains," PROC. IRE, vol. 46, pp. 1619–1627; September, 1958. Some of the material in this paper was presented at the General Assembly of URSI in Boulder, Colo., August/September, 1957.

[2] V. Fock, "The distribution of currents induced by a plane wave on the surface of a conductor," *J. Phys.* (*USSR*), vol. 10, pp. 130–136; February, 1946.

[3] J. C. Schelling, C. R. Burrows, and E. B. Ferrell, "Ultra-short wave propagation," PROC. IRE, vol. 21, pp. 427–463; March, 1933.

[4] In the knife-edge diffraction theory of Fresnel-Kirchhoff, the Fresnel cosine and sine integrals have as a limit the parameter $v = 2\sqrt{kd_2/\pi}\sin\psi_0$ where d_2 is the distance from the knife edge. If the transmitter to the knife-edge distance approaches infinity, d in (1) becomes equal to $2d_2$. For this limit and for small ψ_0, the parameter v can be identified with the symbol Z used here.

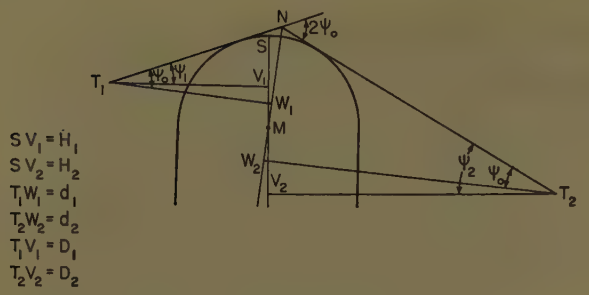

Fig. 1—Geometry for a mountain with a smooth crest.

Thus

$$K_{re}(Z) = [1 - C(Z) - S(Z)]\cos(\pi Z^2/2) - [S(Z) - C(Z)]\sin(\pi Z^2/2) \quad (3b)$$

$$K_{im}(Z) = [1 - C(Z) - S(Z)]\sin(\pi Z^2/2) + [S(Z) - C(Z)]\cos(\pi Z^2/2) \quad (3c)$$

where by (1)

$$Z = \psi_0(2kd/\pi)^{1/2}, \qquad X = \psi_0(2ka)^{1/3}.$$

Also

$$H_{re}(X) + jH_{im}(X) = (2^{3/2}/\pi)e^{j\pi/4}(2ka)^{2/3}\rho \cdot \left\{\int_0^\infty [\psi(3\psi + 2\psi_0)]^{1/2}\exp[-jka(5\psi_0\psi^2 + 2\psi^3)]d\psi + (\rho/2)\int_0^\infty \psi\exp[-2jka(7\psi_0\psi^2/2 + 2\psi^3)]d\psi\right\} \quad (4a)$$

or

$$H_{re}(X) + jH_{im}(X) = (2^{3/2}/\pi)\rho\left\{\int_0^\infty (\xi M)^{1/2}(\cos P - j\sin P)\cdot\exp[-5\sqrt{3}X\xi^2/4 - \xi^3]d\xi + (\rho/2^{5/3})\int_0^\infty \xi(\cos N - j\sin N)\cdot\exp[-7\sqrt{3}X'\xi^2/8 - \xi^3]d\xi\right\}, \quad (4b)$$

where

ρ is the polarization parameter,

$\rho = 0.7$ for vertical polarization,

$\rho = -1.0$ for horizontal polarization. (5a)

$$M^2 = (3\xi + X\sqrt{3})^2 + X^2,$$

$$P = \pi/12 - \mu/2 + 5X\xi^2/4 \quad (5b)$$

$$\tan\mu = X/(3\xi + X\sqrt{3})$$

$$X' = X2^{1/3},$$

$$N = \pi/12 + 7X'\xi^2/8. \quad (5c)$$

Fig. 1 defines the remaining symbols in the equations. The center plane NM through the crest of the mountain bisects the angle T_1NT_2 where T_1N and T_2N are the tangents to the mountain from the transmitter T_1 and receiver T_2. The vertical plane is SM.

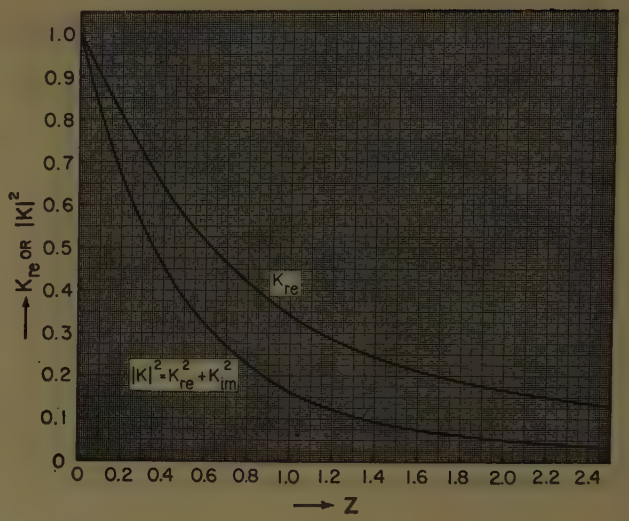

Fig. 2—Knife-edge contribution to the diffraction field behind a mountain: real part, K_{re}, vs parameter $Z = \psi_0(2kd/\pi)^{1/2}$. For comparison, $P_K = |K|^2/4(d_1+d_2)^2$ represents total power behind a knife-edge mountain.

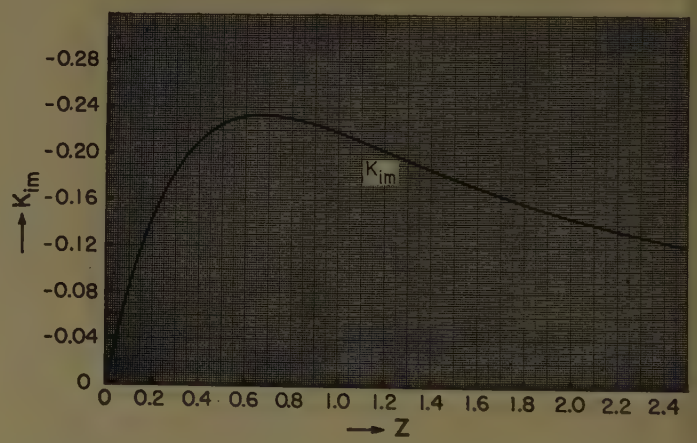

Fig. 3—Knife-edge contribution to the diffraction field behind a mountain: imaginary part, K_{im}, vs parameter $Z = \psi_0(2kd/\pi)^{1/2}$.

Let

$d_1, d_2 = T_1W_1, T_2W_2$ = respective transmitter and receiver distances measured to the plane NM.

$D_1, D_2 = T_1V_1, T_2V_2$ = distances from T_1 and T_2 to the plane SM.

$d = 2d_1d_2/(d_1+d_2)$ is the harmonic mean between distances d_1 and d_2.

$H_1, H_2 = SV_1, SV_2$ = distances below top of mountain for T_1 and T_2.

$2\psi_0$ = diffraction angle $= 180° - \angle T_1NT_2$. Also $\psi_0 = \angle NT_1W_1 = \angle NT_2W_2$.

$2\psi_0 = \Psi_1 + \Psi_2$ where $\Psi_1 = \angle NT_1V_1$ and $\Psi_2 = \angle NT_2V_2$.

That is, Ψ_1 and Ψ_2 are the angles subtended at T_1 and T_2, respectively, by the mountain. For small angles,

$$\Psi_1 \simeq H_1/D_1, \quad \Psi_2 \simeq H_2/D_2, \quad 2\psi_0 \simeq H_1/D_1 + H_2/D_2.$$

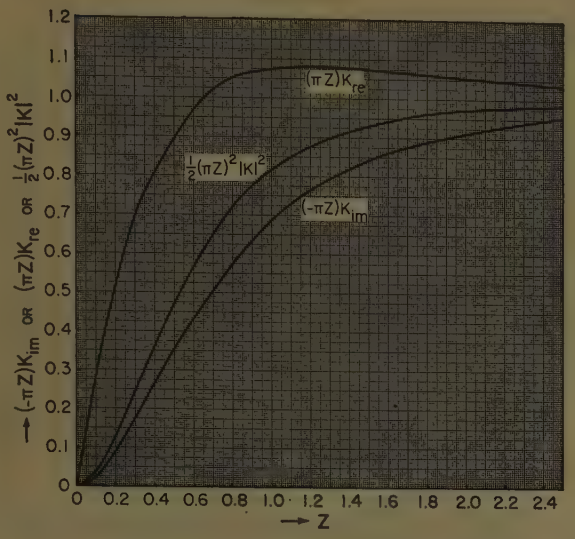

(a)

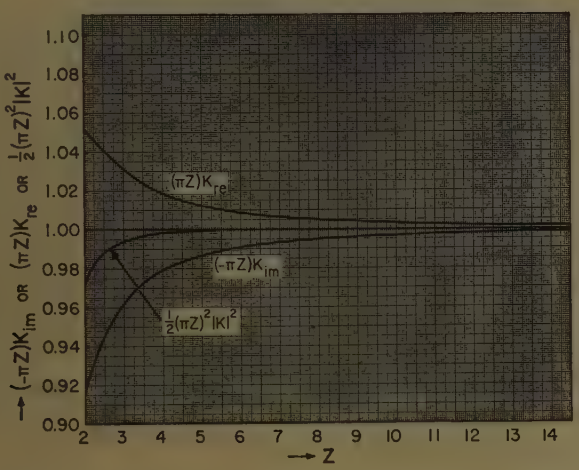

(b)

Fig. 4—(a) Knife-edge contribution to the diffraction field behind a mountain: curves represent (πZK_{re}), $(-\pi ZK_{im})$, and $[(\pi Z)^2|K|^2/2]$ against Z and are more accurate than those of Figs. 2 and 3 for large Z. (b) Knife-edge contribution to the diffraction field behind a mountain: same functions as in Fig. 4(a) for large values of Z. The functions tend towards unity.

A short note of explanation is appropriate. The transformation from (4a) to (4b) is accomplished by a change in variable, $\xi=\psi e^{i\pi/6}(2ka)^{1/3}$. After the transformation, it becomes evident that the halo term is a function of X only. The independence of the halo components H_{re}, H_{im}, on distance is obtained by approximating the F functions[1] by the integer 2. This is accurate if

$$2\psi_0 ka/kd < 0.8 \qquad (6)$$

which is justified for common values of kd.

III. Values for the Knife-Edge and Halo Components

The functions K_{re} and K_{im} are plotted in Figs. 2–4, and H_{re} and H_{im} are plotted in Figs. 5 and 6. Figs. 2 and 3 give more accurate values for the knife-edge components for $Z<0.7$ and Fig. 4(a) and 4(b) for $Z>0.7$. Also, the halo functions are tabulated in Table I, and the

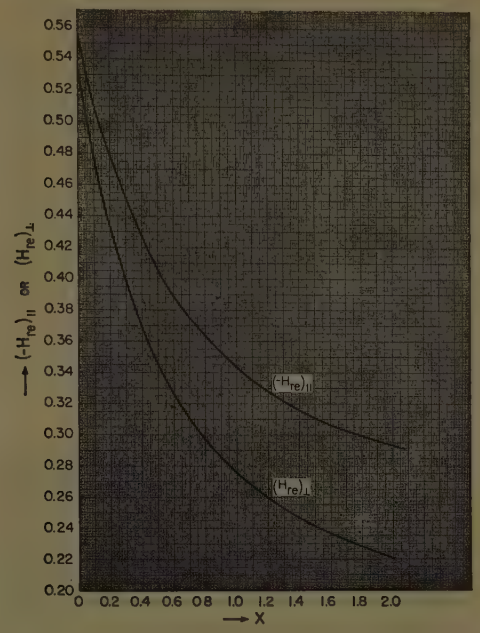

Fig. 5—Halo contribution to the diffraction field behind a mountain: real part $(-H_{re})_\parallel$ for horizontal and $(H_{re})_\perp$ for vertical polarization, vs parameter $X=\psi_0(2ka)^{1/3}$.

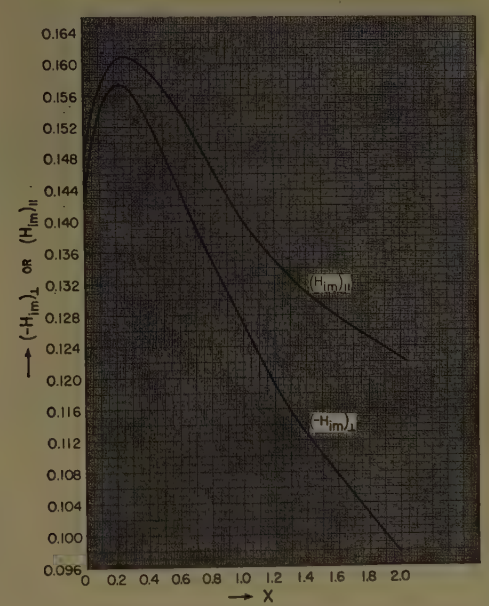

Fig. 6—Halo contribution to the diffraction field behind a mountain: imaginary part $(H_{im})_\parallel$ for horizontal and $(-H_{im})_\perp$ for vertical polarization, vs parameter $X=\psi_0(2ka)^{1/3}$.

knife-edge functions can be calculated by (3b) and (3c) with the help of Fresnel integral tables. None of these curves exhibit oscillations, most of them are monotonic. Although the individual components (1-S-C) and (S-C) oscillate, multiplication by the phase factor exp $(j\pi Z^2/2)$ removes the oscillations.

The ratio (X/Z) occurs in (2). It depends only on (a/λ) and (d/λ), but not explicitly on ψ_0. Fig. 7 is a plot of constant values of (X/Z) ranging from 0.05 to 2 vs values of (a/λ) and (d/λ).

The ranges of the parameters found in practice are $2\psi_0=0\cdots0.2$ radian, $ka=0\cdots10^6$, $kd=6\times10^3\cdots$

TABLE I

REAL AND IMAGINARY PARTS OF HALO COMPONENTS FOR HORIZONTAL (‖) AND VERTICAL (⊥) POLARIZATION

X	$(H_{re})_{\parallel}$	$(H_{im})_{\parallel}$	$(H_{re})_{\perp}$	$(H_{im})_{\perp}$
0	−0.554	0.148	0.534	−0.143
0.02	−0.544	0.150	0.521	−0.146
0.04	−0.539	0.153	0.512	−0.149
0.08	−0.518	0.155	0.487	−0.152
0.12	−0.505	0.158	0.468	−0.155
0.20	−0.479	0.161	0.432	−0.157
0.40	−0.427	0.159	0.370	−0.153
0.80	−0.364	0.147	0.297	−0.135
1.20	−0.328	0.135	0.260	−0.119
1.60	−0.306	0.128	0.237	−0.108
2.00	−0.293	0.123	0.221	−0.098

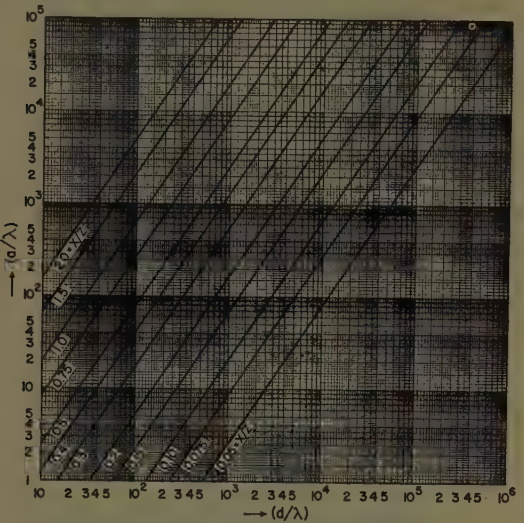

Fig. 7—Values for the parameter $(X/Z)=(2ka)^{1/3}/(2kd/\pi)^{1/2}$ vs (a/λ) and (d/λ).

2×10^6, $X=0\cdots3$, $Z=0\cdots12$ and $(X/Z)=0\cdots2.5$. The graphs cover most of these ranges.

IV. Effect of an Isolated Mountain

A. The Power of the Field

Eqs. (2), (3b), (3c), and (4b) yield the real and imaginary parts of the electric field. The intensity and phase of the field behind the mountain can be computed from these parts. When the mountain is the only obstacle between the stations, the effect of the ground between the stations and the mountain can be disregarded. This occurs when either the earth's surface is too rough to support reflections or when the antennas' directivities effectively discriminate against the earth-reflected path. The phase then is of no concern and an expression for the power is sufficient. From (2), the power diffracted by the mountain is[5]

$$P_0 = [1/4(d_1+d_2)^2]\{[K_{re}+(X/Z)H_{re}]^2 + [K_{im}+(X/Z)H_{im}]^2\}$$
$$= [1/4(d_1+d_2)^2]\{|K|^2+(X/Z)^2|H|^2 + 2(X/Z)[K_{re}H_{re}+K_{im}H_{im}]\} \quad (7)$$

[5] The basic transmission loss, L_b, is related to P_0 by $L_b=P_0(\lambda/4\pi)^2$.

where

$$|K|^2=K_{re}^2+K_{im}^2, \qquad |H|^2=H_{re}^2+H_{im}^2.$$

B. Procedure for Calculation

The procedure for the calculation of the power behind a mountain given k, a, D_1, D_2 and H_1, H_2, when ground reflections are unimportant, is as follows.

1) Calculate d_1, d_2, and ψ_0. From geometry, these parameters are related to the angles Ψ_1 and Ψ_2 subtended by the mountain at the transmitter and receiver.

$$d_1 = D_1\cos[(\Psi_2-\Psi_1)/2] + (a-H_1)\sin[(\Psi_2-\Psi_1)/2] \simeq D_1$$
$$d_2 = D_2\cos[(\Psi_2-\Psi_1)/2] - (a-H_2)\sin[(\Psi_2-\Psi_1)/2] \simeq D_2$$
$$2\psi_0=\Psi_1+\Psi_2\simeq H_1/D_1+H_2/D_2$$

2) Calculate the mean distance $d=2d_1d_2/(d_1+d_2)$.

3) Calculate three parameters in the following order.[6]

$$X=\psi_0(2ka)^{1/3}, \quad (X/Z)=(2ka)^{1/3}/(2kd/\pi)^{1/2}, \quad Z=X/(X/Z)$$

or use Fig. 7 for (X/Z).

4) Calculate K_{re} and K_{im} for the Z value from (3b) and (3c), or read off their values from Figs. 2 and 3 or 4.

5) Read off H_{re} and H_{im} for the X value from Figs. 5 and 6 or use Table I.

6) Perform the operations in (7) to obtain the power.

C. Numerical Examples

Several examples are included in Table II. In all cases, the condition $2\psi_0 a/d<0.8$ is satisfied. The example in which $a=10$ miles, $d=20$ miles, $2\psi_0=2°$, and $\lambda=2$ feet is calculated below in detail.

It is found that $ka=1.658\times10^5$, $kd=3.317\times10^5$, $X=1.208$, $(X/Z)=0.1505$, and $Z=8.03$. All these quantities are calculated. (X/Z) may also be read off Fig. 7. From Fig. 4, $\pi ZK_{re}=1.005$, $\pi ZK_{im}=-0.995$. Hence $K_{re}=0.0399$, $K_{im}=-0.0395$, $|K|^2=0.003145$. From Figs. 5 and 6, $H_{re}=(-0.328)_{\parallel}$, $(0.259)_{\perp}$; $H_{im}=(0.1348)_{\parallel}$, $(-0.1189)_{\perp}$ where $\parallel$ denotes horizontal and $\perp$ denotes vertical polarization.

$$K_{re}+(X/Z)H_{re}=(-0.00943)_{\parallel},\ (0.0788)_{\perp}$$
$$K_{im}+(X/Z)H_{im}=(-0.01917)_{\parallel},\ (-0.0574)_{\perp}.$$

From (7), $4(d_1+d_2)^2P_0=(0.000456)_{\parallel}$, $(0.00950)_{\perp}$.

If the mountain were replaced by a knife edge, the power would be $4(d_1+d_2)^2P_k=|K|^2=0.003145$. Hence the difference in db from knife edge introduced by the crest of the mountain is $(-8.38)_{\parallel}$, $(4.80)_{\perp}$ db. Often this calculation can be avoided by the use of Fig. 8 as will be explained in a following section.

[6] This sequence avoids an indeterminancy in (X/Z) when $X=Z=0$ for a diffraction angle ψ_0 equal to zero.

TABLE II

NUMERICAL EXAMPLES FOR THE EFFECT OF AN ISOLATED MOUNTAIN

Example	(a)	(b)	(c)	(d)	(e)	(f)
a miles	1	1	1	10	10	20
d miles	50	20	50	20	10	5
$2\psi_0$ degrees	6	2	6	2	0.5	0.5
λ feet	2	2	20	2	2	1
$ka/10^3$	16.6	16.6	1.66	166.	166.	663.
X	1.682	0.561	0.781	1.208	0.302	0.479
X/Z	0.0442	0.0698	0.0651	0.151	0.213	0.338
Z	38.0	8.03	12.0	8.03	1.42	1.42
$(P_0/P_K)_\parallel$ db	−6.27	−5.10	−6.83	−8.38	−3.22	−5.19
$(P_0/P_K)_\perp$ db	5.59	3.15	3.80	4.80	2.21	3.00

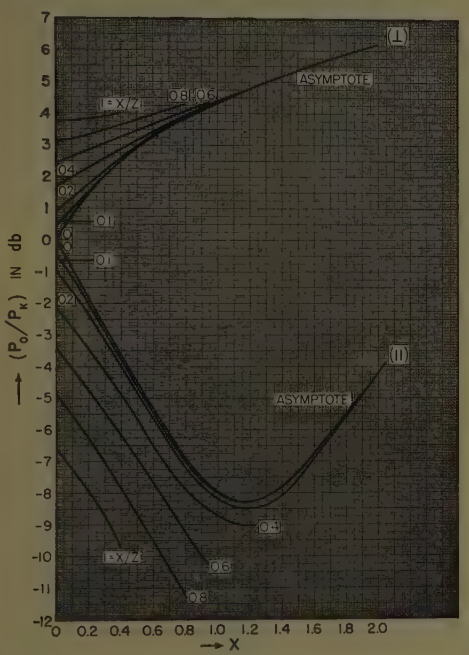

Fig. 8—Power ratio in db behind an isolated mountain compared to a knife edge vs parameter X for various X/Z. The top set of curves are for vertical ($\perp$) polarization and the bottom set for horizontal ($\parallel$) polarization. The asymptotic curves are for $Z\to\infty$ or $X/Z\to 0$.

D. Limiting Cases

Eq. (7) has an asymptotic behavior for large Z, say $Z\geq 2.5$. Large values of Z occur often as shown in the examples. In this limit, it can be seen from Fig. 4(b) that the knife-edge components approach

$$(-K_{im}) \to (K_{re}) \to (1/\pi Z). \tag{8}$$

The expression for the power can be simplified to

$$P_0 = \{1/[2(d_1+d_2)\pi Z]^2\}[(1+\pi X H_{re})^2 + (-1+\pi X H_{im})^2]$$
$$= 2\{1/[2(d_1+d_2)\pi Z]^2\}[1+(\pi^2X^2/2)\,|\,H\,|^2 + \pi X(H_{re}-H_{im})]. \tag{9}$$

The dependence of the power on X and Z separate as factors. Denote the square bracket in (9) by

$$2f(X) = (1+\pi X H_{re})^2 + (-1+\pi X H_{im})^2. \tag{10}$$

The function $f(X)$ gives the dependence on X and is tabulated in Table III for both polarizations. It is equal to the diffracted power relative to knife edge. Thus, for example (d) in Table II, the relative power can be found directly to be $(-8.3)_\parallel$ and $(4.8)_\perp$ *db* for $X=1.2$.

TABLE III

POWER FUNCTION $f(X)$ VS X (10)

X	$[f(X)]_\parallel$	$[f(X)]_\perp$
0	1.000	1.000
0.02	0.957	1.043
0.04	0.916	1.085
0.08	0.840	1.169
0.12	0.770	1.252
0.20	0.649	1.412
0.40	0.427	1.783
0.80	0.202	2.423
1.20	0.148	3.008
1.60	0.210	3.587
2.00	0.381	4.151

TABLE IV

POWER FUNCTION $g(X/Z)$ VS (X/Z) (12)

X/Z	$[g(X/Z)]_\parallel$	$[g(X/Z)]_\perp$
0	1.000	1.000
0.1	0.893	1.110
0.2	0.792	1.226
0.4	0.609	1.476
0.6	0.454	1.751
0.8	0.324	2.050
1.0	0.221	2.373
1.5	0.0778	3.289
2.0	0.0992	4.362

Another limiting case of (7) occurs for a zero diffraction angle, that is for grazing angles.

$$X/Z = (2ka)^{1/3}/(2kd/\pi)^{1/2}, \quad X = Z = K_{im} = 0, \quad K_{re} = 1$$

$$P_0 = [1/4(d_1+d_2)^2][1 + A_{\perp,\parallel}(X/Z) + B_{\perp,\parallel}(X/Z)^2] \tag{11}$$

where $A_{\perp,\parallel}=1.068,\ -1.108;\ B_{\perp,\parallel}=0.305,\ 0.329$. Eq. (11) is the same as (38) in the previous paper,[1] and has been shown to agree well with experiment.

Let

$$g(X/Z) = 1 + A_{\perp,\parallel}(X/Z) + B_{\perp,\parallel}(X/Z)^2. \tag{12}$$

The function $g(X/Z)$ is tabulated in Table IV.

E. Graphs for the Power and Comparison with Experiment

In general, the power in (7) multiplied by $4\times(d_1+d_2)^2$ is a function only of X and (X/Z), or X and Z. The ratio of the power relative to that obtained for a knife edge is plotted in Fig. 8 vs X for various (X/Z) values. The manner in which the power approaches the asymptotes for small (X/Z) or large Z is evident. These curves in Fig. 8 can replace steps 4 to 6 in the procedure under Section IV-B if a high accuracy is not required.

The total power relative to $[1/4(d_1+d_2)^2]$ is given in Fig. 9 vs X for various (X/Z). This graph is obtained by adding the contribution in db for the knife edge to the values in Fig. 8. These curves in Fig. 9 are effectively a plot of power vs scattering angle $\psi_0 \propto X$. When the

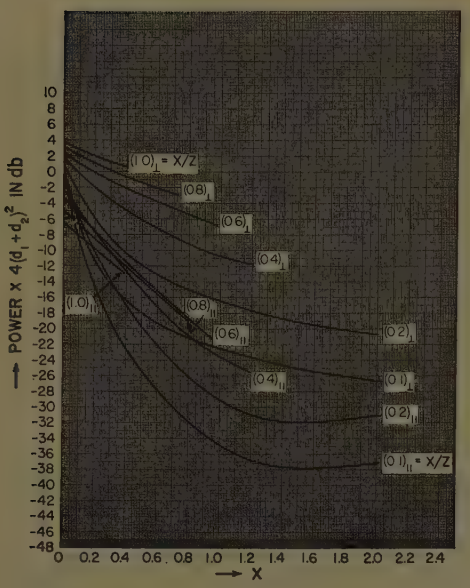

Fig. 9—Power multiplied by $4(d_1+d_2)^2$ in db behind an isolated mountain vs parameter X for various X/Z.

radius of curvature or (X/Z) is large, as is usually the case in rolling country with relatively small differences in altitude, the theory can be used only for small diffraction angles, because of the approximation given by (6) in the analysis. This is not a serious limitation because in rolling country large angles are rarely encountered. Conversely, in an area with high mountains, larger scattering angles may occur. Usually at the same time the radius of curvature is smaller, and the theory is applicable to this combination of small radius and large angle of diffraction.

The curves in Fig. 9 are redrawn on a larger scale in Fig. 10 and are compared with experimental measurements of the power vs scattering angles up to 19 degrees for both polarizations. The experimental apparatus has already been described.[1] The experimental range of ka is 0 to 250, of X is 0 to 0.8, and of (X/Z) is 0.1 to 0.51. In all cases, the initial slopes agree well with theory up to 5 degrees and in some cases 10 degrees depending on radius of curvature.

For larger scattering angles the experimental curves continue as straight lines and the theoretical curves slope upward.

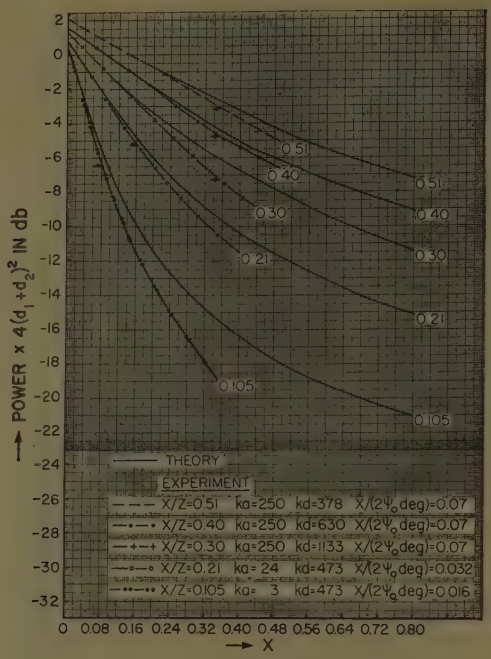

(a)

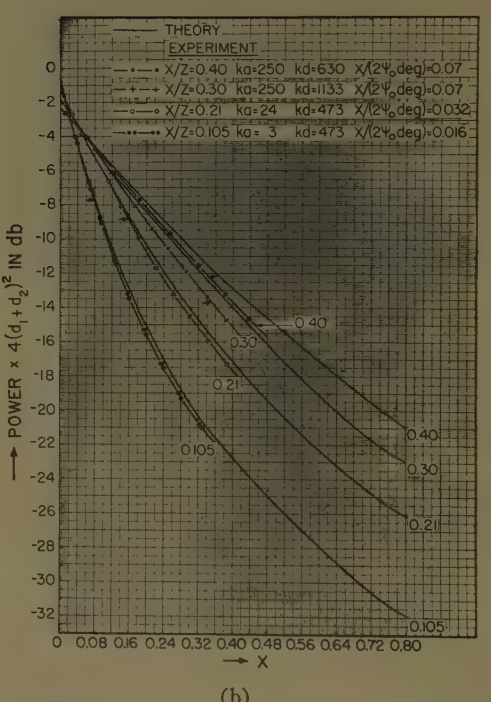

(b)

Fig. 10—(a) Comparison of theory and experiment for the power behind an isolated, perfectly reflecting cylindrical mountain up to diffraction angles of 19 degrees (vertical polarization). (The illumination factors for the transmitter-receiver antennas have been taken into account.) The arrows at the experimental curves indicate the value of X for which $2\psi_0=5$ degrees. (b) Similar to Fig. 10(a) (horizontal polarization).

V. Effect of Ground Reflections

A. Amplitude and Phase of Field

In cases when reflections occur from the ground between stations and the mountain, more elaborate calculations are required corresponding to the well known four-ray theory.[3] Then Table I and Figs. 2 to 6 for the real and imaginary parts have to be used. The expressions for the power in Section IV are inadequate.

The method for including reflections is as follows. The flat ground is eliminated by assuming that the reflected rays from the ground come from virtual images T_1' and T_2', shown in Fig. 11, for the transmitter and receiver. The four paths that the field is propagated, namely T_1CT_2, $T_1G_1CT_2$, $T_1CG_2T_2$, and $T_1G_1CG_2T_2$ are replaced by four other paths, namely T_1CT_2, $T_1'CT_2$, T_1CT_2' and $T_1'CT_2'$. The total field may then be calculated by combining the four components, taking into account their phases and amplitudes and the reflection properties of the ground.

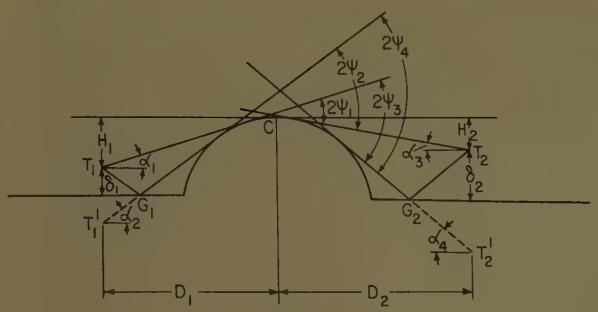

Fig. 11—Geometry for a mountain with a reflecting ground.

Let α_1, α_2, α_3 and α_4 be the angles subtended by the mountain with the horizon at T_1, T_1', T_2, T_2', respectively; H_1 and H_2 be the heights below the top of the mountain for T_1, T_2; D_1 and D_2 be the distances from T_1 and T_2 to a vertical line through the peak of the mountain; δ_1 and δ_2 be the heights above the ground for T_1 and T_2 or below the ground for T_1' and T_2'; $2\psi_1$, $2\psi_2$, $2\psi_3$ and $2\psi_4$ be the scattering angles for the four paths mentioned above, respectively.

Then the following relations are obtained:

$$2\psi_1 = \alpha_1 + \alpha_3 \quad 2\psi_2 = \alpha_2 + \alpha_3$$
$$2\psi_3 = \alpha_1 + \alpha_4 \quad 2\psi_4 = \alpha_2 + \alpha_4 = 2(\psi_2 + \psi_3 - \psi_1) \tag{13a}$$

$$\alpha_1 = \sin^{-1}\left\{\frac{a}{[D_1^2 + (a - H_1)^2]^{1/2}}\right\} - \sin^{-1}\left\{\frac{a - H_1}{[D_1^2 + (a - H_1)^2]^{1/2}}\right\} \tag{13b}$$

For α_2, α_3, and α_4, respectively, use $H_1+2\delta_1$, H_2, $H_2+2\delta_2$ and D_1, D_2, D_2 instead of H_1 and D_1 in (13b). For each of the four paths, there are different values for d_1 and d_2. Since d_1 and d_2 occur in the phases, they must be calculated accurately and cannot be approximated by D_1 and D_2.

Let

$$\beta_1 = (\alpha_3 - \alpha_1)/2 \quad \beta_2 = (\alpha_3 - \alpha_2)/2$$
$$\beta_3 = (\alpha_4 - \alpha_1)/2 \quad \beta_4 = (\alpha_4 - \alpha_2)/2. \tag{13c}$$

Then the distances are given by

$$\begin{aligned} d_{1i} &= D_1 \cos\beta_i + (a - H_1)\sin\beta_i \quad \text{for } i = 1, 3 \\ &= D_1 \cos\beta_i + (a - H_1 - 2\delta_1)\sin\beta_i \text{ for } i = 2, 4 \\ d_{2i} &= D_2 \cos\beta_i - (a - H_2)\sin\beta_i \quad \text{for } i = 1, 2 \\ &= D_2 \cos\beta_i - (a - H_2 - 2\delta_2)\sin\beta_i \text{ for } i = 3, 4. \end{aligned} \tag{13d}$$

The average distance can be calculated by

$$d_i = 2d_{1i}d_{2i}/(d_{1i} + d_{2i}). \tag{13e}$$

For each path, values can be calculated from (13) for ψ_0, d, d_1, and d_2, and then for X and Z. The total field is the sum of these four rays.

Let R_1 and R_2 be the magnitudes of the reflection coefficients of the grounds on the transmitter and receiver sides of the mountain. Let ϕ_1 and ϕ_2 be the respective phase advances at reflection. Then the total field E is given by

$$E = E_1 + R_1E_2e^{-j\phi_1} + R_2E_3e^{-j\phi_2} + R_1R_2E_4e^{-j(\phi_1+\phi_2)}. \tag{14a}$$

For a perfectly smooth reflecting ground, the equations reduce to

$$R_1 = R_2 = 1,$$
$$\phi_1 = \phi_2 \begin{cases} = 0 \text{ for } \perp \text{ polarization} \\ = \pi \text{ for } \parallel \text{ polarization,} \end{cases}$$

and

$$E = E_1 \pm E_2 \pm E_3 + E_4 \tag{14b}$$

where the plus sign must be taken for $\perp$ and the minus sign for $\parallel$ polarization.

In (14), the expression for E_i, $(i=1, 2, 3, 4,)$ is given by

$$2(D_1 + D_2)E_i \simeq \exp[-jk(d_{1i} + d_{2i})(1 + \psi_i^2/2)] \times \{K_{re}(Z_i) + jK_{im}(Z_i) + (X_i/Z_i)[H_{re}(X_i) + jH_{im}(X_i)]\}. \tag{14c}$$

The expression for the electric field already includes the amplitude and phase lag introduced by diffraction and the phase changes due to different path lengths d_1 and d_2. Since these expressions are combined in (14b), the phase factor $k(d_1+d_2)(1+\psi_0^2/2)$ must be included in the analysis in addition to the knife edge and halo terms.

B. Procedure for Calculation

The procedure for calculating the power behind a mountain, given k, a, D_1, D_2, H_1, H_2, δ_1, and δ_2 and including reflections from a perfectly reflecting ground is as follows:

1) Calculate d_{1i}, d_{2i}, and ψ_i for the four rays from (13).
2) Calculate the mean distances d_i by (13e).
3) Calculate the parameters X_i, $(X/Z)_i$ and Z_i for each ray.
4) Read off $(K_{re})_i$ and $(K_{im})_i$ from Figs. 2 to 4.
5) Read off $(H_{re})_i$ and $(H_{im})_i$ from Figs. 5 and 6, for each ray.
6) Calculate for each ray the real and imaginary parts of the electric field given by the right hand side of (14c), including the extra phase introduced by the exponential factor.
7) Sum the real parts and the imaginary parts of the four electric fields according to (14b).
8) Square the sum of the real parts and the sum of the imaginary parts, and add the squares. The result gives the value for $16(D_1+D_2)^2P_0$.

VI. Conclusion

The theory for diffraction by a mountain with a smooth cylindrical crest is shown to agree with experimental results up to larger angles of diffraction. The smaller the radius of curvature, the larger the angle. This situation usually is encountered in practical cases.

When the stations are far enough away the integrals previously derived[1] depend only on one parameter. Hence the results of numerical calculations can be presented by simple graphs and tables that simplify the application of the theory to practical problems.

For some typical cases, numerical results are given and it is shown that the diffraction field may be up to 3 or 4 db greater than behind a knife-edge mountain of equal height, when the field is vertically polarized, and up to 7 or 8 db smaller when it is horizontally polarized.

This theory is one step nearer to explaining the experimental evidence found in field practice. Irregular shape of the mountain, vegetation or roughness of the ground, conductivity, etc., are other determining factors which have yet to be taken into account.

Pattern of an Antenna on a Curved Lossy Surface*

J. R. WAIT† and A. M. CONDA†

Summary—**Extensive numerical results are presented for the radiation fields of electric and magnetic type antennas mounted on smooth curved surfaces of finite conductivity. The model chosen is a circular cylinder whose surface impedance is specified. A residue series representation is employed for the portion of space deep in the shadow while a geometrical-optical representation is used in the "lit" region. In the penumbra, the fields are expressed in terms of the "Fock functions." The results are also applicable to other smoothly varying curved surfaces such as spheres, parabolic cylinders, and paraboloids. As an application, the *E*-plane patterns are computed for a small loop antenna on a spherical earth for both sea and land illustrating the so-called cut-back effect.**

Introduction

DESPITE the fact that the formal solution of the electromagnetic diffraction by a homogeneous sphere was obtained a half century ago, certain numerical aspects of the problem have yet to be completely resolved. The difficulty usually originates in the extremely poor convergence of the rigorous harmonic series solution when the circumference of the sphere, *ka*, expressed in wavelengths, is large. Employing function-theoretic means Watson[1] demonstrated in 1918, for a vertical electric dipole source, that this harmonic series could be converted to a more rapidly convergent series in certain regions of space. This representation has become known as the residue series as each term corresponds to a residue of a complex pole. This particular method has been exploited and refined in the late 1930's by Vvedensky[2] in Russia, Millington in England, and Van der Pol and Bremmer[4] in Holland The latter two authors in particular developed a highly accurate method to compute the values of the complex poles occurring in the residue series. Essentially, this is based on a representation for spherical wave functions by Hankel functions of order one third, and for this reason it has become known as the Hankel approximation. It is more precise, although more involved, than the so-called tangent approximations of Vvedensky and Millington which were based on a second order representation of the spherical wave functions due to Debye. Van der Pol and Bremmer have also demonstrated in an elegant fashion that a geometrical-optical representation for the fields can be derived as a special case which is valid when the source and observer are well within "line of sight." In 1939 Gray[5] extended the Van der Pol-Bremmer treatment to a vertical magnetic dipole source.

In 1941, Norton[6] presented a systematic method for calculating the ground wave field for both vertical and horizontal polarization. Using a number of graphs, the

* Manuscript received by the PGAP, April 27, 1958.

† Radio Propagation Eng. Div., Natl. Bur. of Standards, Boulder, Colo.

[1] G. N. Watson, "The diffraction of radio waves by the earth," *Proc. Roy. Soc. London*, vol. A95, pp. 83–99, October, 1918; pp. 546–563, July, 1919.

[2] B. Vvedensky, "The diffractive propagation of radio waves," *Tech. Phys., U.S.S.R.*, vol. 2, pp. 624–639, June, 1935; vol. 3, pp. 915–925, November, 1936; vol. 4, pp. 579–591, August, 1937.

[3] G. Millington, "The diffraction of wireless waves round the earth," (a summary of the diffraction analysis, with a comparison between the various methods), *Phil. Mag.*, ser. 7, vol. 27, pp. 517–542; May, 1939.

[4] B. Van der Pol and H. Bremmer, "The diffraction of electromagnetic waves from an electrical point source round a finitely conducting sphere, with applications to radiotelegraphy and the theory of the rainbow; the propagation of radio waves over a finitely conducting spherical earth," *Phil. Mag.*, ser. 7, vol. 24, pp. 141–176, July, 1937; vol. 24, pp. 825–864, suppl., November, 1947; vol. 25, pp. 817–834, suppl., June, 1938; vol. 27, pp. 261–275, March, 1939.

[5] M. C. Gray, "Diffraction and refraction of a horizontally polarized electromagnetic wave over a spherical earth," *Phil. Mag.*, ser. 7, vol. 27, pp. 421–436; April, 1939.

[6] K. A. Norton, "The calculation of ground-wave field intensity over a finitely conducting spherical earth," Proc. IRE, vol. 29, pp. 623–639; December, 1941.

method was in a form suitable for use by radio engineers. In 1949, Bremmer,[7] in a monograph, presented a comprehensive outline of the theory of ground wave propagation, listed a number of formulas for field computations, and gave certain illustrative examples.

For most applications of ground wave propagation, the above mentioned methods of Norton and Bremmer are satisfactory. The exception is when a line joining the receiving antenna and the transmitting antenna just grazes the earth. Norton has proposed that this case be treated by interpolating between geometrical optics and the field computed in the shadow from the first term of the residue series. Often this is quite adequate. In this instance, Bremmer recommends that the complete residue series representation should be employed. Unfortunately, it becomes very poorly convergent near the boundary of light and shadow, particularly if the antenna heights are large. The convergence of the residue series is also poor at short distances at low and medium radio frequencies even when the transmitter and receiver are both on or near the ground. In the latter case, an alternative series has been developed[7,8] which contains inverse powers of ka and the leading term is the flat earth formula of Sommerfeld.

A more direct approach to the evaluation of the field near the light shadow boundary is to return to the original complex integral representation which is actually the first stage in the Watson transformation. This is the line of attack adopted by Fock and Leontovich[9,10] in the U.S.S.R. By making approximations to the spherical wave functions which were equivalent to the "Hankel approximation" of Van der Pol and Bremmer,[11] the integral for the field was put in a form suitable for numerical integration. Fock[12] gave numerical results only for perfect conductivity. Fock has shown that the same integral arises in the diffraction of a plane wave by a paraboloid and in any generally convex surface if the radius of curvature is large and smoothly varying.

It is the purpose of this paper to further exploit Fock's method to the computation of the field of a source on a curved surface whose conductivity is finite. Particular attention is paid to the case where the receiving antenna is at a large distance from the surface and the transmitting antenna is on or near the surface. By utilizing reciprocity, the results will also apply when the location of the receiving and transmitting antennas are interchanged. For purposes of presentation, a so-called cut-back factor is introduced which is essentially the E-plane radiation pattern of a small loop antenna located on the curved surface. The term "cut-back" has been used to describe the rather pronounced reduction of the field at low angles.

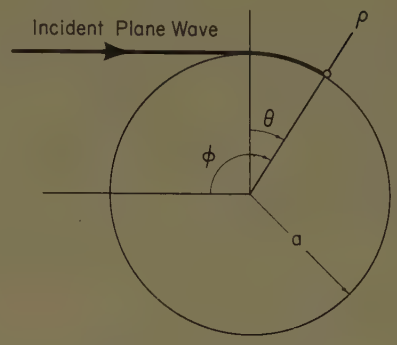

Fig. 1—Plane wave incident on a circular cylinder.

Formulation

The model chosen as a basis for calculation is an infinitely long circular cylinder of radius a as illustrated in Fig. 1 along with the appropriate cylindrical coordinate system. (The surface of the cylinder is defined by $\rho = a$ and the z axis is directed into the paper.) The incident plane wave which is incident normally on the cylinder has a z component of the magnetic field only. It is given by

$$H_z^{\text{inc}} = H_0 e^{ik\rho \cos \phi}. \tag{1}$$

The boundary condition on the surface of the cylinder is

$$E_\phi = -ZH_z]_{\rho=0}$$

where Z is by definition the surface impedance. For a homogeneous cylinder of conductivity σ, dielectric constant ϵ, and permeability μ, Z can be well approximated by

$$Z \cong \sqrt{\frac{i\mu\omega}{\sigma + i\omega\epsilon}} = \eta \tag{2}$$

where η is the intrinsic impedance of the medium. The boundary condition in this form is usually ascribed to Leontovich[13] who showed that for plane wave incidence it is valid if $|\eta/\eta_0| \ll 1$ where $\eta_0 \cong 120\pi$ is the intrinsic impedance of free space. More recently, Monteath,[14] and Wait and Surtees[15] have shown a more general re-

[7] H. Bremmer, "Terrestrial Radio Waves," Elsevier Publishing Co., New York, N. Y.; 1949.

[8] J. R. Wait, "Currents excited on a conducting surface of large radius of curvature," IRE Trans. on Microwave Theory and Techniques, vol. MTT-4, pp. 143–145; July, 1956, and "Radiation from a vertical antenna over a curved stratified ground," *J. Res. NBS*, vol. 56, pp. 230–240; July, 1956.

[9] V. A. Fock, "Diffraction of radio waves around the earth's surface," *J. Phys. U.S.S.R.*, vol. 9, pp. 256–266; April, 1945, and *J. Theoret. Exp. Phys.*, vol. 15, pp. 480–490; June, 1945.

[10] M. A. Leontovich and V. A. Fock, "Propagation of electromagnetic waves along the earth's surface," *J. Phys. U.S.S.R.*, vol. 10, pp. 13–24; January, 1946.

[11] Fock used Airy integrals which are simply related to Hankel functions of order one third. (See following text.)

[12] V. Fock, "Distribution of currents induced by a plane wave on the surface of a conductor," *J. Phys. U.S.S.R.*, vol. 10, pp. 130–140, 399–409; February, 1946, and A. S. Goriainov, "Diffraction of plane electromagnetic waves on a conducting cylinder," *Radioteknika i Electronika*, vol. 3, pp. 603–614; May, 1958.

[13] M. A. Leontovich, "Approximate boundary conditions for the electromagnetic field on the surface of a good conductor," *Bull. Acad. Sci., U.S.S.R.*, serie physique, vol. 9, p. 16; January, 1944. (In Russian.)

[14] G. D. Monteath, "Application of the compensation theorem to certain radiation and propagation problems," *Proc. IEE*, vol. 98, pt. 4, pp. 23–30; January, 1951.

[15] J. R. Wait and W. J. Surtees, "Impedance of a top-loaded antenna of arbitrary length over a circular grounded screen," *J. Appl. Phys.*, vol. 25, pp. 553–555; May, 1954.

striction in that the tangential fields should vary slowly in a distance equal to $|\gamma^{-1}|$ where

$$\gamma = [i\mu\omega(\sigma + i\omega\epsilon)]^{1/2}$$

is the propagation constant of the conductor. Actually, a somewhat improved formula for Z for ground wave propagation is given by

$$Z \cong \eta[1 - \eta^2/\eta_0^2]^{1/2}$$

for vertical polarization.[8]

Formal Solution

To obtain the field scattered from the cylinder, the incident field is first written in the form

$$H_z^{\text{inc}} = H_0 \sum_{n=0}^{\infty} \epsilon_n e^{in\pi/2} J_n(k\rho) \cos n\phi \tag{3}$$

using a well-known addition theorem in Bessel functions. In the above $\epsilon_0 = 1$, $\epsilon_n = 2 (n \neq 0)$ and $J_n(k\rho)$ is the Bessel function of the first kind of integral order n. Since the secondary field H_z^{sec} is to be a solution of the wave equation and is to give rise to outgoing waves at infinity it is written in the form

$$H_z^{\text{sec}} = \sum_{n=0}^{\infty} A_n H_n^{(2)}(k\rho) \cos n\phi \tag{4}$$

where $H_n^{(2)}(k\rho)$ is the Hankel function of the second kind. The secondary field, H_z^{sec}, is now chosen to satisfy the approximate boundary condition which can be rewritten

$$\left[E_\phi = \frac{i}{\omega\epsilon}\frac{\partial H_z}{\partial \rho} = -ZH_z\right]_{\rho=a} \tag{5}$$

noting that $H_z = H_z^{\text{inc}} + H_z^{\text{sec}}$. It readily follows that

$$A_n = -H_0\epsilon_n e^{in\pi/2}\frac{J_n'(x) + GJ_n(x)}{H_n^{(2)\prime}(x) + GH_n^{(2)}(x)} \tag{6}$$

where $x = ka$ and $G = -iZ/\eta_0$. On the surface of the cylinder, the field can be written in the form

$$H_z]_{\rho=a} = H_0 F(x, \phi) \tag{7}$$

where

$$F(x, \phi) = \frac{2}{\pi i x}\sum_{n=0}^{\infty}\frac{\epsilon_n e^{in\pi/2}\cos n\phi}{H_n^{(2)\prime}(x) + GH_n^{(2)}(x)}. \tag{8}$$

The voltage induced in a small loop placed at $\rho = a$ is proportional to $H_z]_{\rho=a}$; thus $F(x, \phi)$ can be regarded as the radiation pattern of the loop in the principal or E plane.

Complex Integral Representation

Unfortunately, (8) for the pattern function $F(x, \phi)$ is very cumbersome for purposes of calculation unless x is reasonably small. For example, something of the order of $2x$ terms are required to secure 5 per cent accuracy. When x is large, it is desirable to represent $F(x, \phi)$ as a complex integral which can be either evaluated directly, or by deforming the contour around the complex poles of the integrand. Such procedures have been used by Watson, Van der Pol and Bremmer, and Fock for treating the problem of ground wave propagation from a vertical dipole on the surface of the earth. The application of these same techniques to cylinder problems (which for large curvatures are essentially the same as the sphere problems), has been carried out by Franz,[16–18] Sensiper,[19] Baillin,[20] and Wait.[21,22] In most of this work, with the exception of Fock's, the complex integral was evaluated only by a saddle point method yielding useful expressions for the field in the "lit" region of space (*i.e.*, $|\phi| < \pi/2$). On the other hand, the residue series representation is only useful deep in the shadow (*i.e.*, $|\phi| > \pi/2$). In 1946, Fock evaluated the complex integral for the perfectly conducting cylinder by numerical means and thus bridged the gap between the geometric-optical domain and the residue series solution deep in the shadow. The extension to imperfectly conducting cylinders is carried out in what follows. These results enable the pattern $F(x, \phi)$ to be evaluated for the whole domain of ϕ.

The complex integral representation of the function F for large cylinders can be written (see Appendix) as

$$F \cong e^{-ika\theta} g(X) \tag{9}$$

where

$$g(X) \cong \frac{1}{\sqrt{\pi}}\int_{\Gamma_2}\frac{e^{-iXt}}{W_1'(t) - qW_1(t)}\,dt \tag{10}$$

where Γ_2, the integration contour, runs from $\infty e^{-i2\pi/3}$ to 0, then out along the real axis to ∞. The other symbols are defined as follows:

$W_L(t)$ is the Airy integral defined in the appendix,

$$X = \left(\frac{ka}{2}\right)^{1/3}\theta = \left(\frac{ka}{2}\right)^{1/3}\left(\phi - \frac{\pi}{2}\right)$$

and

$$q = -i\left(\frac{ka}{2}\right)^{1/3} Z/\eta_0.$$

[16] W. Franz, "The green's functions of cylinders and spheres," *Z. Naturforsch.*, vol. 9A, pp. 705–716; September, 1954.

[17] W. Franz and R. Galle, "Semiasymptotic series for the diffraction of a plane wave by a cylinder," *Z. Naturforsch.*, vol. 10A, pp. 374–378; May, 1955.

[18] W. Franz and P. Beckman, "Creeping waves for objects of finite conductivity," IRE Trans. on Antennas and Propagation, vol. AP-4, pp. 203–208; July, 1956.

[19] S. Sensiper, "Cylindrical radio waves," IRE Trans. on Antennas and Propagation, vol. AP-5, pp. 56–70; January, 1957.

[20] L. L. Bailin and R. J. Spellmire, "Convergent representations for the radiation fields from slots in large circular cylinders," IRE Trans. on Antennas and Propagation, vol. AP-5, pp. 374–382; October, 1957.

[21] J. R. Wait, "Radiation characteristics of axial slots on a conducting cylinder," *Wireless Engr.*, vol. 32, pp. 316–323; December, 1955, and "Pattern of a flush mounted microwave antenna," *NBS J. Res.*, vol. 59, pp. 255–259; October, 1957.

[22] J. R. Wait and J. Kates, "Radiation Patterns of Circumferential Slots on Moderately Large Conducting Cylinders," Monograph No. 167 R, *IEE, London;* February, 1956, republished in *Proc. IEE*, pt. C, pp. 289–296; February, 1956.

The above formula for F is only valid if $(ka/2)^{1/3}\pi \gg 1$ and $|\phi| \ll 1$. This means that attention, at least for the moment, is restricted to large cylinders and to the region near the shadow boundary (*i.e.*, the penumbra). In terms of the electrical constant ϵ and σ the complex factor q is conveniently written

$$q = A2^{1/6}e^{-i\pi/4}\left[1 + i\frac{\epsilon\omega}{\sigma}\right]^{-1/2}$$

where

$$A = (ka)^{1/3}\left(\frac{\epsilon_0\omega}{2\sigma}\right)^{1/2}. \tag{11}$$

When the conductivity is sufficiently large (*i.e.*, $\sigma \gg \epsilon\omega$)

$$q \cong A2^{1/6}e^{-i\pi/4}.$$

The geometrical-optics approximation for the function F can be written

$$F = [1 + R]e^{-ika \sin \theta} \tag{12}$$

where $R(\phi)$ is taken equal to the Fresnel reflection coefficient for a plane wave incident on a plane boundary whose surface impedance is Z. Therefore,[23]

$$R = \frac{\sin\theta + Z/\eta_0}{\sin\theta - Z/\eta_0} \cong \frac{\theta + Z/\eta_0}{\theta - Z/\eta_0} \tag{13}$$

and consequently,

$$F \cong e^{-ika\theta}e^{ika\theta^3/3!}\frac{2\theta}{\theta - Z/\eta_0} \tag{14}$$

for small values of θ. This equation can also be found from a saddle point evaluation of the integral $g(X)$ when X is negative and not near zero.

In terms of X and the electrical constants σ and ϵ, the preceding equation becomes

$$F = e^{-ika\theta}e^{iX^3/3}\frac{2(1-i)X}{(1-i)X - 2^{2/3}A\left(1 + i\frac{\epsilon\omega}{\sigma}\right)^{-1/2}} \tag{15}$$

remembering that $X = (ka/2)^{1/3}\theta$.

Up to this point the discussion has referred specifically to a circular cylinder of infinite length. On intuitive grounds one would expect the function F to characterize the pattern in the penumbral region of an antenna on any smooth surface whose radius of curvature is large. The quantity a is then regarded as the principal radius of curvature. It appears to be difficult to justify the proceeding statements on a rigorous basis, for an arbitrary smooth surface. As shown by Fock, however, the concept is valid when applied to a perfectly conducting paraboloid and a similar demonstration was made by Rice[24] for the parabolic cylinder.

[23] It should be noted that if Z is replaced by $(\eta^2 - \eta_0^2\cos^2\theta)^{1/2}$, R becomes the Fresnel reflection coefficient for a homogeneous half space.

[24] S. O. Rice, "Diffraction of plane radio waves by a parabolic cylinder," *Bell Sys. Tech. J.*, vol. 33, pp. 417–502; March, 1954.

For applications to antenna radiation over a spherical earth, it would be more logical to employ a model of a vertical electric dipole located on a homogeneous sphere with a specified surface impedance Z. This was the approach used essentially in the work of Van der Pol and Bremmer, Norton, and Fock. In the present notation, the Hertz function (which has only a radial component) Π of the vertical dipole of unit strength located on the earth's surface is given by

$$\Pi = \frac{e^{-ika\bar{\theta}}}{a\bar{\theta}}V \tag{16}$$

where $\bar{\theta}$ is the angle at the center of the earth subtended by the source dipole and the receiver at height h. In the above,

$$V = \sqrt{\frac{ix}{\pi}}\int_{\Gamma_2} e^{-ixt}\frac{W_1(t-y)}{W_1'(t) - qW_1(t)}dt \tag{17}$$

is an attenuation function and

$$x = \left(\frac{ka}{2}\right)^{1/3}\bar{\theta} \tag{18}$$

and

$$y = \left(\frac{2}{ka}\right)^{1/3}kh. \tag{19}$$

Now when y is large, the Airy integral function $W_1(t-y)$ can be replaced by the first term of its asymptotic expansion for the important range of t in the integration. Furthermore, if x is large in such a way that $x - \sqrt{y}$ is finite then

$$V \cong \frac{x^{1/2}}{y^{1/4}}e^{-i(2/3)y^{3/2}}g(X) \tag{20}$$

when $X = x - \sqrt{y}$ is a finite parameter. It is thus shown that Π expressed as a ratio to the free space Hertz function Π_0 can be written

$$\frac{\Pi}{\Pi_0} \cong F \tag{21}$$

where F is identical to the cut-back factor for the circular cylinder and X has the same geometrical meaning.

If the source dipole were at finite height (say h_0) then the function in (17) should be replaced by[9,10]

$$\bar{V} = \frac{1}{2}\sqrt{\frac{x}{\pi i}}\int_{\Gamma_2} e^{-ixt}W_1(t-y_0)\left[W_2(t-y) + \frac{W_2'(t) - qW_2(t)}{W_1'(t) - qW_1(t)}W_1(t-y)\right]dt \tag{22}$$

where

$$y_0 = \left(\frac{2}{ka}\right)^{1/3}kh_0 \tag{23}$$

and $W_2(t)$ is an Airy integral function. It was shown in an earlier communication,[8] however, that quite generally

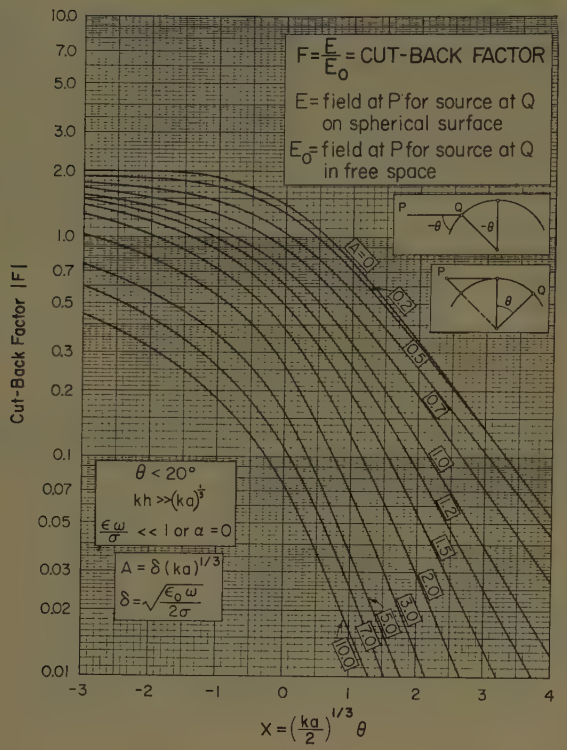

Fig. 2.

$$\overline{V} \cong V\left[1 + i\frac{Z}{\eta_0} kh_0\right] \tag{24}$$

subject to y_0 being small compared with unity and h_0 small compared with $a\bar{\theta}$.

Summarizing, it can be said that the cut-back factor is applicable to a transmitting vertical dipole at height h_0 and a receiving vertical dipole at height h subject to

$$kh_0 \ll \left|\frac{\eta_0}{Z}\right|$$

and

$$kh \gg (ka)^{1/3}.$$

When kh_0 becomes comparable to $|\eta_0/Z|$ it is desirable to define a modified cut-back factor F_m as follows

$$F_m \cong \left[1 + i\frac{Z}{\eta_0} kh_0\right] F \tag{25}$$

which is valid if $kh_0 \ll (ka)^{1/3}$ and $h_0 \ll a\bar{\theta}$.

Discussion of the Cut-back Factor

Using the preceding formulas for $\epsilon\omega/\sigma = 0$ or $\alpha = 0$, the function $|F|$ described as the cut-back factor, is plotted in Fig. 2 as a function of the angular parameter X for A ranging from 0 to 10. The geometrical optics representation is used for large negative X and the residue series representation (see Appendix) for large positive X while in the intermediate range, the integral $g(X)$ was evaluated numerically. The corresponding

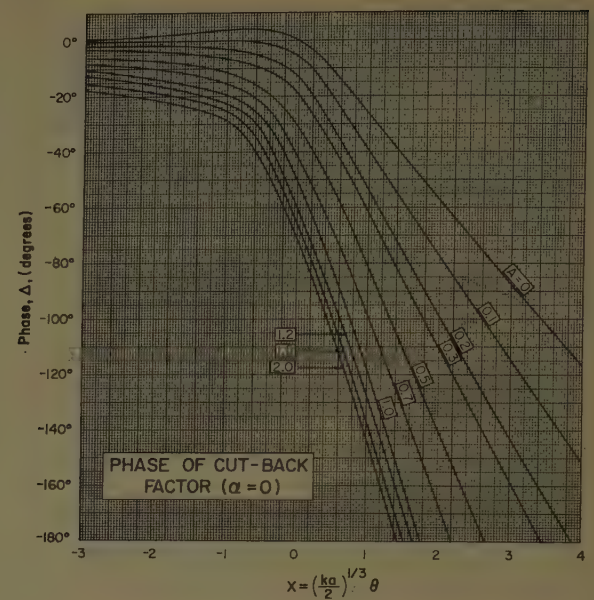

(a)

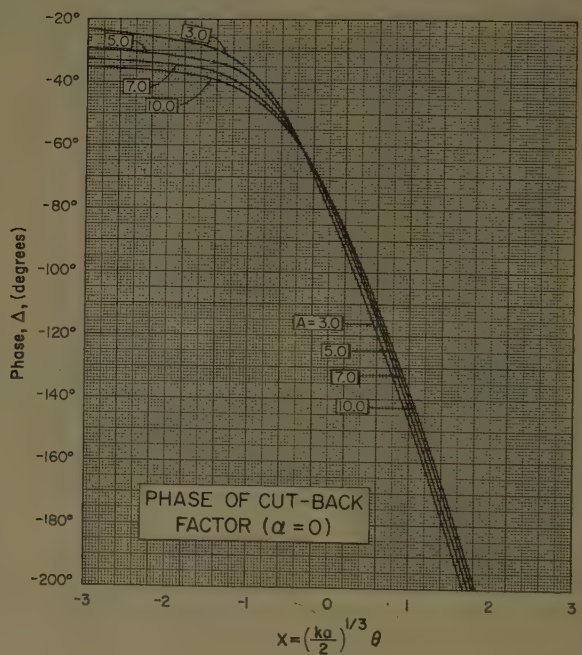

(b)

Fig. 3.

phase factor Δ is plotted in Fig. 3(a) and 3(b). It is defined as follows

$$F = |F| e^{-ika\theta} e^{iX^3/3} e^{i\Delta} \text{ for } \theta < 0 \tag{26}$$

and

$$F = |F| e^{-ika\theta} e^{i\Delta} \text{ for } \theta > 0. \tag{27}$$

This method of normalizing the phase enables one to regard Δ as a phase difference between that of the incident field and that of the resultant field in the lit region (*i.e.*, $\theta < 0$). On the other hand, Δ is the phase difference between the electrical arc length $ka\theta$ and the re-

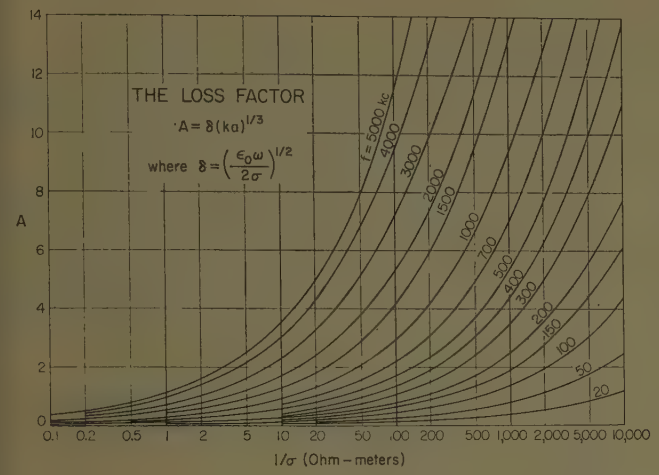

(a)

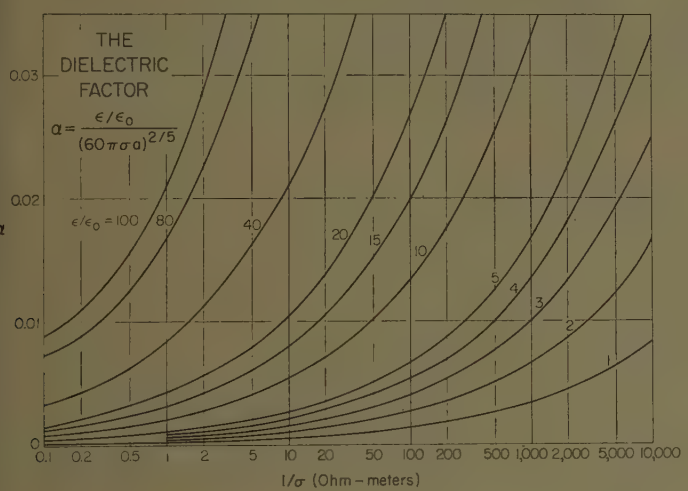

(b)

Fig. 4.

sultant field in the shadow (*i.e.*, $\theta > 0$). To facilitate the application of these curves to radiation pattern computation for a source on a spherical earth, the loss factor A is shown plotted in Fig. 4(a) as a function of the reciprocal of the ground conductivity, $1/\sigma$, for frequencies from 20 to 5000 kc. To allow for normal atmospheric refraction the radius a is replaced by 4/3 times the actual earth radius.

At the higher frequencies and when the earth is poorly conducting, the displacement currents in the ground can be appreciable. Following Belkina[25] the complex factor q is rewritten in the form

$$q = \frac{-ip^{5/6}}{(\alpha p - i)^{1/2}} \tag{28}$$

which is equivalent to (11) if

$$p = [2A^6]^{1/5}$$

and

$$\alpha = \frac{\epsilon}{\epsilon_0}\left(\frac{2}{\sigma a \eta_0}\right)^{2/5} = \frac{\epsilon/\epsilon_0}{(60\pi\sigma a)^{2/5}} .$$

This seemingly complicated representation for q has the advantage that the displacement currents are described by the parameter α which is independent of frequency.

To facilitate the conversion from the electrical constants σ and ϵ, the factor α is plotted as a function of $1/\sigma$ for various values of the relative dielectric constant ϵ/ϵ_0 again assuming an effective earth radius factor of 4/3. Numerical values of $|F|$ and Δ are listed in Tables I and II respectively for A ranging from 0 to 10 and α from 0 to 0.03. For the smaller A values, the influence of α is negligible and, consequently, only the results for $\alpha = 0$ need be shown.

The cut-back factor $|F|$ is shown plotted in Fig. 5(a) and 5(b) for sea water and average land respectively. The frequency varies from 20 to 5000 kc. The electrical constants for sea water are taken as $\sigma = 5$ and $\epsilon/\epsilon_0 = 80$ and for land they are taken as $\sigma = 0.005$ and $\epsilon/\epsilon_0 = 15$. As an interesting illustration $|F|$ is shown plotted in Fig. 5(c) for both land and sea at 100 kc. The corresponding geometrical-optical approximation for $|F|$ is also shown. At the larger negative values of θ, the two sets of curves merge together as they should. As θ approaches zero, however, they diverge significantly. It is noted that geometrical-optics would predict that $|F|$ tends to zero at the shadow boundary (*i.e.*, as $\theta \to 0$).

Extension to *E*-Parallel Polarization

Up to this point, the incident wave is polarized such that the magnetic field is parallel to the axis of the cylinder. The other case of interest is when the electric field is parallel to the axis of the cylinder. The conversion of the former to the latter is simply obtained by replacing H_z by E_z and Z/η_0 by η_0/Z. Therefore, if the incident field is given by

$$E_z^{\text{inc}} = E_0 e^{ik\rho \cos\phi} = E_0 e^{-ik\rho \sin\theta} \tag{29}$$

the resultant tangential field on the cylinder is

$$E_z]_{\rho=a} = E_0 F^* \tag{30}$$

where

$$F^* \cong \left[\frac{1}{\sqrt{\pi}} \int_{\Gamma_2} \frac{e^{-iXt}}{W_1'(t) - q^* W_1(t)}\, dt\right] e^{-ika\theta} \tag{31}$$

with

$$q^* = -i\left(\frac{ka}{2}\right)^{1/3} \frac{\eta_0}{Z} .$$

Since in most applications $|Z/\eta_0| \ll 1$ and $ka \gg 1$, the quantity $|q^*|$ is a very large number and F^* can be well approximated by

[25] M. G. Belkina, "Tables to calculate the electromagnetic field in the shadow region for various soils," Soviet Radio Press, Moscow, U.S.S.R.; 1949.

TABLE I

NUMERICAL VALUES OF $|F|$

X	$A=0$ $\alpha=0$	$A=0.1$ $\alpha=0$	$A=0.2$ $\alpha=0$	$A=0.3$ $\alpha=0$	$A=0.5$ $\alpha=0$	$A=0.7$ $\alpha=0$	$A=1.0$ $\alpha=0$	$A=1.0$ 0.03	$A=1.2$ $\alpha=0$	$A=1.2$ $\alpha=.03$	$A=1.5$ $\alpha=0$	$A=1.5$ $\alpha=0.03$	$A=2.0$ $\alpha=0$	$A=2.0$ $\alpha=0.03$
−3.0	1.998	1.95	1.90	1.85	1.75	1.67	1.55	1.54	1.48	1.47	1.38	1.37	1.24	1.23
−2.5	1.994	1.94	1.88	1.82	1.71	1.61	1.47	1.47	1.39	1.38	1.28	1.28	1.14	1.13
−2.0	1.982	1.92	1.84	1.78	1.65	1.53	1.38	1.37	1.29	1.28	1.17	1.16	1.02	1.01
−1.5	1.948	1.87	1.79	1.71	1.56	1.41	1.25	1.24	1.14	1.13	1.02	1.01	0.869	0.868
−1.0	1.861	1.82	1.70	1.61	1.44	1.26	1.13	1.12	0.968	0.962	0.850	0.840	0.707	0.706
−0.5	1.682	1.59	1.54	1.43	1.27	1.09	0.918	0.917	0.771	0.765	0.669	0.664	0.539	0.537
0	1.400	1.34	1.27	1.15	1.01	0.901	0.711	0.710	0.579	0.570	0.490	0.485	0.386	0.384
0.5	1.059	1.00	0.952	0.904	0.801	0.659	0.500	0.499	0.401	0.389	0.317	0.316	0.301	0.300
1.0	0.738	0.722	0.692	0.661	0.563	0.446	0.316	0.315	0.251	0.248	0.181	0.180	0.119	0.117
1.5	0.488	0.477	0.466	0.444	0.384	0.290	0.196	0.195	0.152	0.149	0.102	0.0997	0.0608	0.0608
2.0	0.315	0.312	0.308	0.296	0.249	0.184	0.117	0.116	0.0838	0.0829	0.0528	0.0523	0.0282	0.0288
2.5	0.202	0.202	0.202	0.194	0.162	0.114	0.0668	0.0664	0.0453	0.0449	0.0266	0.0261	0.0122	0.0127
3.0	0.130	0.130	0.130	0.127	0.104	0.0706	0.0384	0.0376	0.0246	0.0243	0.0129	0.0127	0.00489	0.00522

X	$A=3$ $\alpha=10$	$A=3$ $\alpha=0.03$	$A=5$ $\alpha=0$	$A=5$ $\alpha=0.03$	$A=7$ $\alpha=0$	$A=7$ $\alpha=0.03$	$A=10$ $\alpha=0$	$A=10$ $\alpha=0.01$	$A=10$ $\alpha=0.02$	$A=10$ $\alpha=0.03$
−3.0	1.02	1.01	0.768	0.743	0.588	0.586	0.444	0.442	0.450	0.455
−2.5	0.919	0.916	0.651	0.647	0.512	0.510	0.379	0.382	0.388	0.394
−2.0	0.804	0.797	0.558	0.555	0.432	0.431	0.315	0.317	0.322	0.326
−1.5	0.664	0.662	0.459	0.457	0.344	0.344	8.246	0.248	0.253	0.256
−1.0	0.520	0.518	0.355	0.354	0.255	0.257	0.181	0.183	0.185	0.187
−0.5	0.685	0.684	0.249	0.249	0.175	0.182	0.122	0.124	0.126	0.127
0	0.267	0.266	0.158	0.159	0.110	0.115	0.0742	0.0760	0.0778	0.0791
0.5	0.139	0.142	0.0779	0.0788	0.0535	0.0560	0.0368	0.0375	0.0386	0.0399
1.0	0.0646	0.0661	0.0339	0.0355	0.0229	0.0246	0.0158	0.0162	0.0166	0.0176
1.5	0.0306	0.0311	0.0149	0.0156	0.0103	0.0111	0.00639	0.00668	0.00695	0.00714
2.0	0.0129	0.0132	0.00603	0.00617	0.00389	0.00426	0.00257	0.00263	0.00275	0.00288
2.5	0.00528	0.00547	0.00247	0.00261	0.00204	0.00216	0.00105	0.00108	0.00112	0.00115
3.0	0.00219	0.00225	0.000898	0.000949	0.000689	0.000693	0.000361	0.000369	0.000385	0.000407

The third significant figure is doubtful in some cases.

TABLE II

NUMERICAL VALUES OF Δ (IN DEGREES)
(VALUES ARE NEGATIVE EXCEPT WHERE INDICATED BY +)

X	$A=0$ $\alpha=0$	$A=0.1$ $\alpha=0$	$A=0.2$ $\alpha=0$	$A=0.3$ $\alpha=0$	$A=0.5$ $\alpha=0$	$A=0.7$ $\alpha=0$	$A=1.0$ $\alpha=0$	$A=1.0$ 0.03	$A=1.2$ $\alpha=0$	$A=1.2$ 0.03	$A=1.5$ $\alpha=0$	$A=1.5$ 0.01	$A=1.5$ 0.02	$A=1.5$ 0.03	$A=2.0$ $\alpha=0$	$A=2.0$ 0.01	$A=2.0$ 0.02	$A=2.0$ 0.03
−3.0	+0.52	0.94	2.2	3.6	6.1	8.4	10.9	10.7	13.1	13.0	15.6	15.3	15.1	14.8	18.1	18.0	17.8	17.6
−2.5	+0.85	0.91	2.4	3.9	7.0	9.1	12.6	12.4	14.4	14.2	17.2	16.9	16.7	16.4	19.6	19.5	19.4	19.3
−2.0	+1.5	0.85	2.7	4.4	8.0	10.3	14.4	14.1	15.2	14.9	19.0	18.8	18.6	18.3	21.9	21.7	21.5	21.2
−1.5	+2.4	0.74	3.0	5.3	9.4	12.9	17.0	16.6	19.2	18.8	21.7	21.5	21.3	21.0	24.6	24.1	23.5	23.0
−1.0	+3.7	0.63	4.1	7.1	12.2	16.1	20.3	19.8	23.2	22.8	25.8	25.5	25.3	25.0	29.0	28.3	27.6	26.9
−0.5	+3.9	1.2	6.3	10.3	18.1	23.2	28.2	27.5	33.0	32.6	38.7	38.4	38.1	37.8	44.5	43.0	41.5	40.0
0	0	6.0	13.7	19.8	31.5	41.8	50.9	49.7	60.8	59.3	68.3	67.6	66.9	66.2	69.0	68.1	67.2	66.1
0.5	11.4	20.7	32.0	38.8	53.5	67.3	83.0	79.0	92.3	90.8	100.0	101.1	102.2	103.4	106.2	104.1	102.7	101.3
1.0	26.6	40.3	53.9	61.3	81.2	98.4	119.0	116.0	128.4	124.4	137.6	136.0	134.8	133.1	144.1	141.8	140.0	138.9
1.5	42.7	59.5	76.9	86.3	112.4	132.8	158.8	155.5	170.0	166.8	178.2	178.2	177.0	175.5	186.5	184.6	182.7	180.9
2.0	58.0	77.9	99.0	110.7	141.1	167.4	198.6	195.0	212.0	210.0	221.5	220.3	219.1	217.9	227.1	225.5	223.9	222.4
2.5	72.9	96.5	116.0	134.8	170.5	202.0	236.8	234.8	251.0	249.2	262.1	263.9	262.5	261.1	269.8	268.2	266.6	265.1
3.0	87.6	114.9	142.7	158.7	199.9	236.3	276.9	274.5	293.2	290.5	309.2	307.6	306.0	304.4	313.5	311.6	309.4	307.5

X	$A=3.0$ $\alpha=0$	$A=3.0$ 0.01	$A=3.0$ 0.02	$A=3.0$ 0.03	$A=5.0$ $\alpha=0$	$A=5.0$ 0.01	$A=5.0$ 0.02	$A=5.0$ 0.03	$A=7.0$ $\alpha=0$	$A=7.0$ 0.01	$A=7.0$ 0.02	$A=7.0$ 0.03	$A=10$ $\alpha=0$	$A=10$ 0.01	$A=10$ 0.02	$A=10$ 0.03
−3.0	23.4	22.8	22.2	21.4	29.1	27.6	26.1	24.5	33.0	30.9	28.8	26.7	35.4	31.2	27.1	23.5
−2.5	25.2	24.4	23.6	22.9	30.7	29.1	27.5	25.8	33.6	31.5	29.4	27.3	36.5	32.0	27.8	24.1
−2.0	27.1	26.3	25.5	24.7	32.2	30.6	29.0	27.3	34.7	32.6	30.5	28.4	37.2	32.6	28.3	24.5
−1.5	29.2	28.6	28.0	26.3	33.2	31.5	29.9	28.2	36.1	34.0	31.9	29.8	38.0	33.2	29.0	24.6
−1.0	37.0	36.1	35.2	34.2	37.6	36.1	34.6	33.2	42.2	40.1	38.0	35.9	43.2	39.1	33.8	28.9
−0.5	54.2	52.5	50.8	49.1	50.8	48.9	47.0	45.0	55.3	53.1	51.0	48.9	56.0	51.2	45.7	42.6
0	81.2	79.5	77.8	76.0	75.7	73.1	70.5	68.0	77.2	75.1	72.9	70.8	77.2	72.1	67.2	63.9
0.5	118.0	116.0	114.0	113.7	107.9	105.2	102.6	99.9	106.8	104.7	102.5	100.4	104.9	99.9	94.5	89.5
1.0	146.0	143.9	142.0	140.2	143.0	140.4	137.8	135.1	140.2	136.8	133.4	130.0	138.2	134.1	128.0	122.9
1.5	187.0	184.0	181.4	180.3	181.1	178.5	175.9	173.3	178.2	174.5	170.8	167.1	176.8	171.2	165.3	159.9
2.0	226.0	224.0	221.8	219.8	219.7	216.8	213.7	210.9	215.8	212.0	208.1	204.4	213.6	206.5	202.1	197.2
2.5	268.1	265.5	263.0	260.0	257.6	254.3	251.0	247.8	253.9	249.8	245.7	241.6	250.8	243.9	238.5	232.2
3.0	306.2	304.1	302.0	300.1	296.1	292.9	289.7	286.4	290.7	296.4	292.1	277.9	286.4	280.1	274.3	269.1

The third significant figure is doubtful in some cases.

$$F^* \cong -\frac{1}{q^*\sqrt{\pi}}\, U(X)e^{-ika\theta} \tag{32}$$

where

$$U(X) \cong \frac{1}{\sqrt{\pi}} \int_{\Gamma_2} \frac{e^{-iXt}}{W_1(t)}\, dt. \tag{33}$$

The integral $U(X)$ has been evaluated numerically by Rice.[24] Noting that

$$H_\phi = \frac{1}{Z} E_z \text{ at } \rho = a$$

it is seen that

$$\frac{\eta_0(ka/2)^{1/3}H_\phi}{E_0} \cong -ie^{-ika\theta}U(X) \cong h_\phi$$

where h_ϕ is the normalized magnetic field. For purposes of presentation, it is useful to introduce a phase factor Δ_h, in analogy to Δ, as follows

$$h_\phi \cong |\, U(X)\,|\, e^{-ika\theta}e^{iX^3/3}e^{i\Delta_h} \text{ for } \theta < 0 \tag{34}$$

and

$$h_\phi \cong |\, U(X)\,|\, e^{-ika\theta}e^{i\Delta_h} \text{ for } \theta > 0. \tag{35}$$

According to geometrical-optics

$$H_\phi = -(\sin\theta)(E_0/\eta_0)e^{-ika\sin\theta} \text{ at } \rho = a \tag{36a}$$

$$\cong -\theta(E_0/\eta_0)e^{-ika\theta}e^{ika\theta^3/3!} \tag{36b}$$

which is equivalent to

$$h_\phi \cong -2X. \tag{37}$$

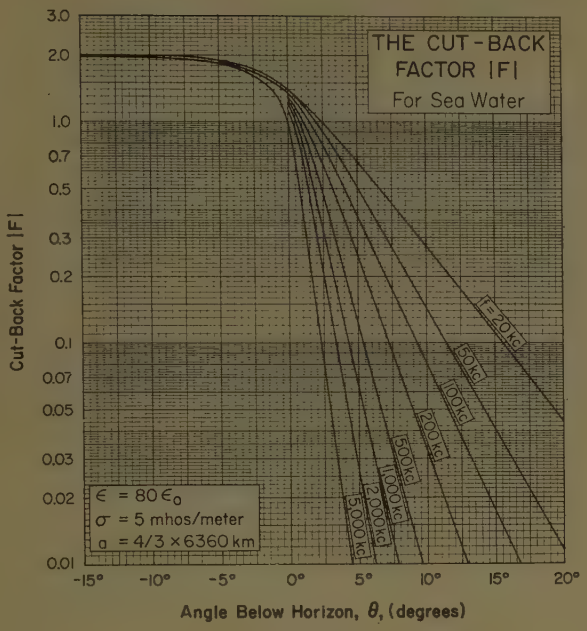

(a)

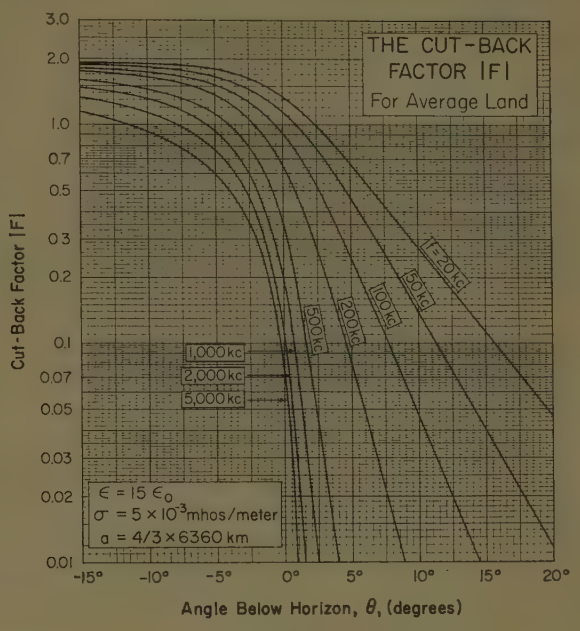

(b)

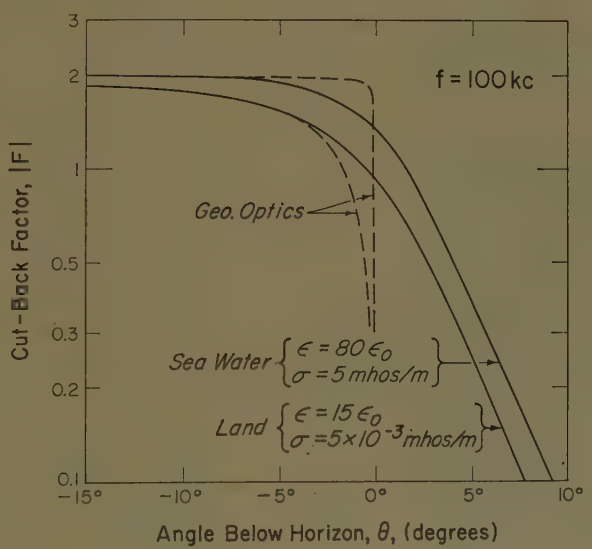

(c)

Fig. 5—The cut-back factor as a function of angle above or below the horizon. (For great heights this angle can be determined adequately by ray tracing methods.)

The function $|U(X)|$ which is proportional to the amplitude of the tangential magnetic field, $|H_\phi|$ is shown plotted in Fig. 6(a) as a function of X on a semi-log scale. The corresponding geometrical-optics approximation is also shown. The function $|U(X)|$ along with the phase factor Δ_h is plotted in Fig. 6(b) using linear scales. In this case, the geometric-optics result is simply a straight line and the phase is zero.

Application to Moderately Large Cylinders

In all the preceding discussion the domain of θ and the radius of curvature is large enough that the tangential magnetic field is described adequately by (9). When ka is not excessively large, the formula for F should be replaced by (53) in the Appendix. The leading term of this expression which is usually adequate, reads

$$F \cong e^{-ika\theta} g\left[\theta\left(\frac{ka}{2}\right)^{1/3}\right] + e^{-ika(\pi-\theta)} g\left[(\pi-\theta)\left(\frac{ka}{2}\right)^{1/3}\right] \tag{38}$$

and is valid for the domain

$$\pi/2 \geqq |\theta| > -\Delta\theta \quad \text{where} \quad (\Delta\theta)^3 \ll 1.$$

The second factor in the above equation can be interpreted as a wave which has "crept" around from the rear of the cylinder. To illustrate the behavior for cylinders of moderate size $|F|$ and Δ based on (38) are plotted in Fig. 7(a) and 7(b) respectively for $ka = 8$ using the normalization for phase defined by (16) and (17). Calculated points from the rigorous harmonic

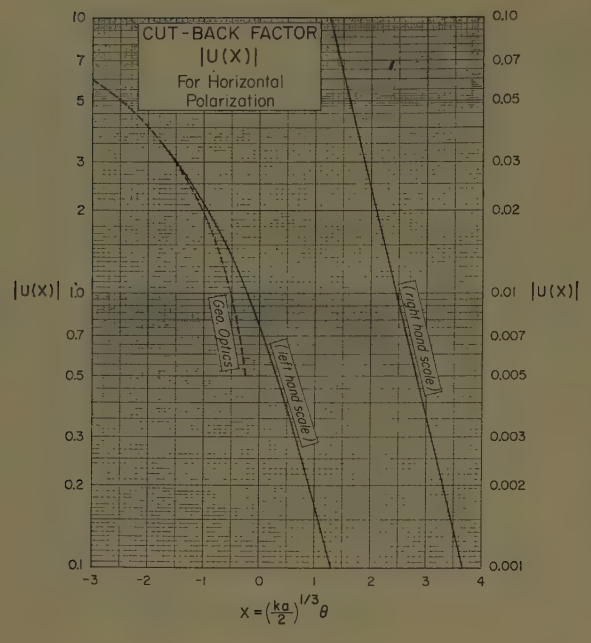

(a)

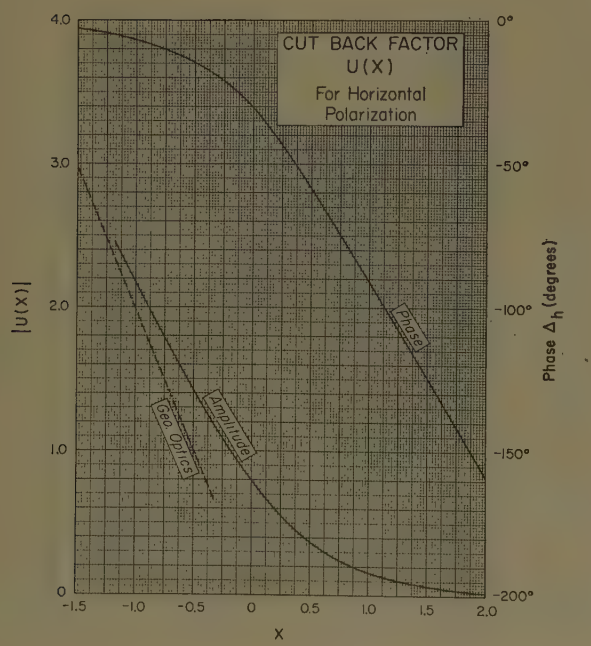

(b)

Fig. 6.

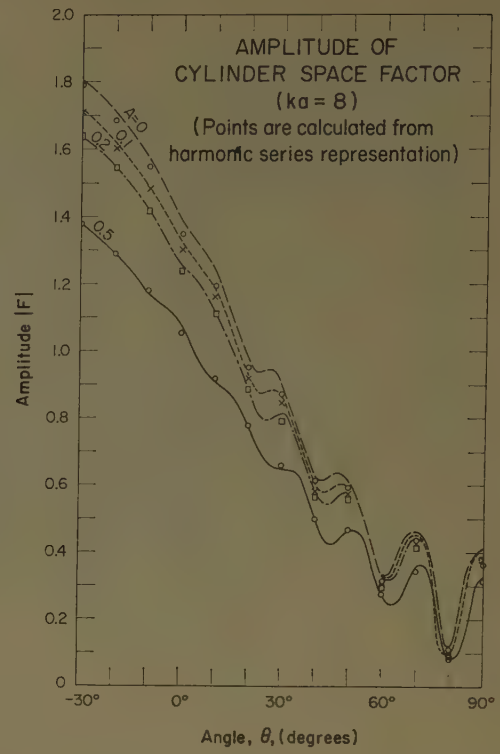

(a)

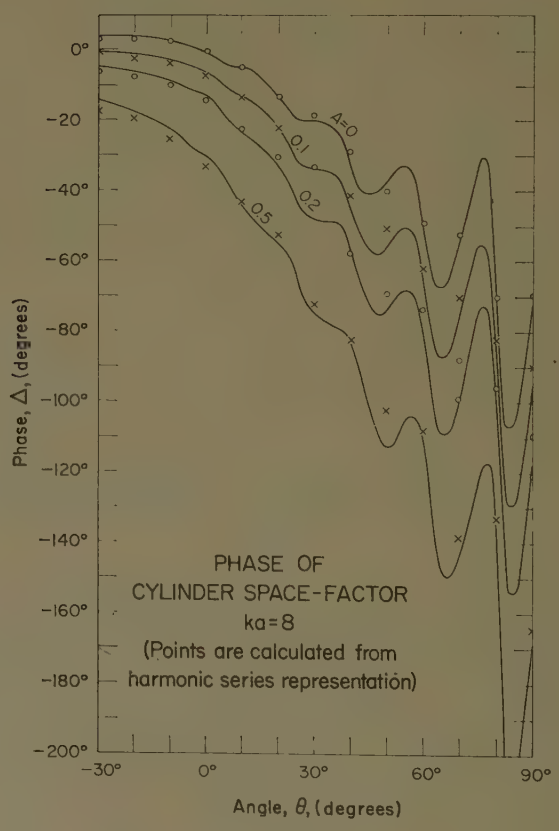

(b)

Fig. 7.

series solution [*i.e.*, (8)] are shown in Fig. 7(a) and 7(b). In view of the fact that ka is not large, the agreement between the two sets of calculations is very reasonable. The corresponding curves for $ka = 21$ are shown in Fig. 8(a) and 8(b) where the agreement between the approximate and the rigorous theory is much improved.

Concluding Remarks

The numerical results presented herein can be used to predict the radiation patterns of electric and magnetic type antennas located on smooth curved surfaces of finite conductivity. For example, in certain investigations of ionospheric wave propagation, it is of importance to know the amplitude of the incident wave at the lower edge of the ionosphere. The curves of the cut-back factor can be used to estimate this quantity. Furthermore, the field measured at the receiving an-

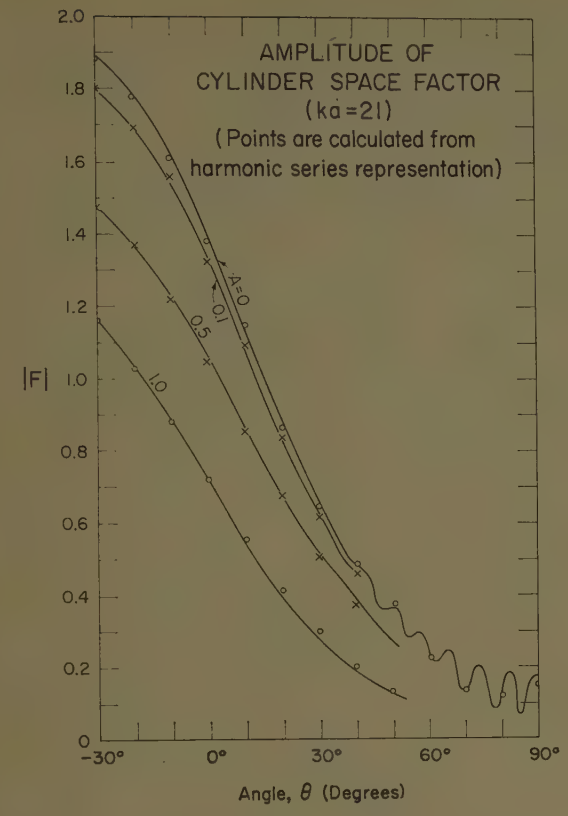

(a)

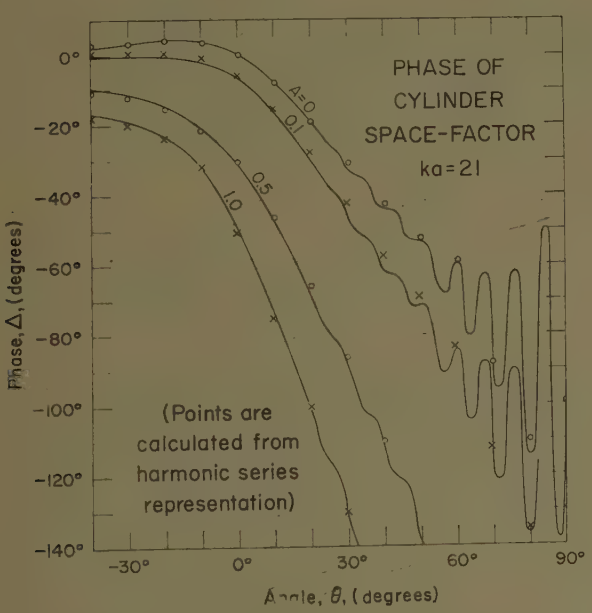

(b)

Fig. 8.

tenna on the ground can also be estimated from the cut-back factor assuming of course, that the amplitude of the downcoming wave is known. It is particularly important to use these antenna cut-back factors in the interpretation of long distance ionospheric sky wave propagation at low radio frequencies. Considerable error may result if the radiation patterns are simply computed on the basis of a flat earth.

An excellent discussion of the application of cut-back factors to the calculation of sky wave field strength has been presented recently by Norton.[26]

Mathematical Appendix[27]

The far field pattern in the equatorial plane or E plane located on the surface of circular conducting cylinders was shown to be described by the function $F(x, \phi)$ where $x = ka$ and ϕ is the angular or azimuthal coordinate. This function is given by

$$F(x, \phi) = \frac{2}{i\pi x} \sum_{n=-\infty}^{+\infty} \frac{e^{in\pi/2} e^{in\phi}}{H_n^{(2)\prime}(x) + GH_n^{(2)}(x)} \tag{39}$$

where $G = -i(Z/\eta_0)$, Z is the surface impedance and $\eta_0 \cong 120\pi$.

The summation is over both positive and negative integers. $H_n^{(2)}(x)$ is a Hankel function of the second kind and the prime indicates a derivative with respect to x. The first step is to express $F(x, \phi)$ as a contour integral in the complex ν plane. The contours chosen are the lines C_2 and C_1 which are located just above and just below the real axis of ν as shown in Fig. 9(a). Some consideration shows[28] that

$$F(x, \phi) = \left(-\frac{1}{2i}\right)\frac{2}{i\pi x} \cdot \int_{C_1+C_2} \frac{e^{-i\nu\pi/2} e^{i\nu\phi}}{[H_\nu^{(2)\prime}(x) + GH_\nu^{(2)}(x)] \sin \nu\pi} \, d\nu. \tag{40}$$

This integral has poles at $\nu = 0, \pm 1, \pm 2, \pm 3, \cdots$ as indicated in Fig. 9(a) as equispaced points on the real axis of ν. It can readily be verified that the sum of residues of the integrand at these poles leads back to the series expression.

Replacing ν by $-\nu$ in the integral over C_2, it is seen that

$$\int_{C_2} \frac{d\nu}{\sin \nu\pi} \frac{e^{i\nu(\phi-\pi/2)}}{[H_\nu^{(2)\prime}(x) + GH_\nu^{(2)}(x)]} = \int_{C_1} \frac{d\nu}{\sin \nu\pi} \frac{e^{-i\nu(\phi-\pi/2)}}{[H_{-\nu}^{(2)\prime}(x) + GH_{-\nu}^{(2)}(x)]} \tag{41}$$

and since

$$H_{-\nu}^{(2)}(x) = e^{-i\nu\pi} H_\nu^{(2)}(x)$$

the integral over C_2 is equal to

$$\int_{C_1} \frac{d\nu}{\sin \nu\pi} \frac{e^{i\nu(3\pi/2-\phi)}}{H_\nu^{(2)\prime}(x) + GH_\nu^{(2)}(x)} \cdot \tag{42}$$

[26] K. A. Norton, "Low and medium frequency ionospheric propagation," sec. 4.2 in "Transmission Loss in Radiowave Propagation," to be published. See also A. D. Watt *et al.*, "Observations on some LF propagation paths in Arctic areas," to be published.

[27] MKS units and a time factor exp $(i\omega t)$ are employed.

[28] J. R. Wait, "Electromagnetic Radiation from Cylindrical Structures," to be published as a monograph.

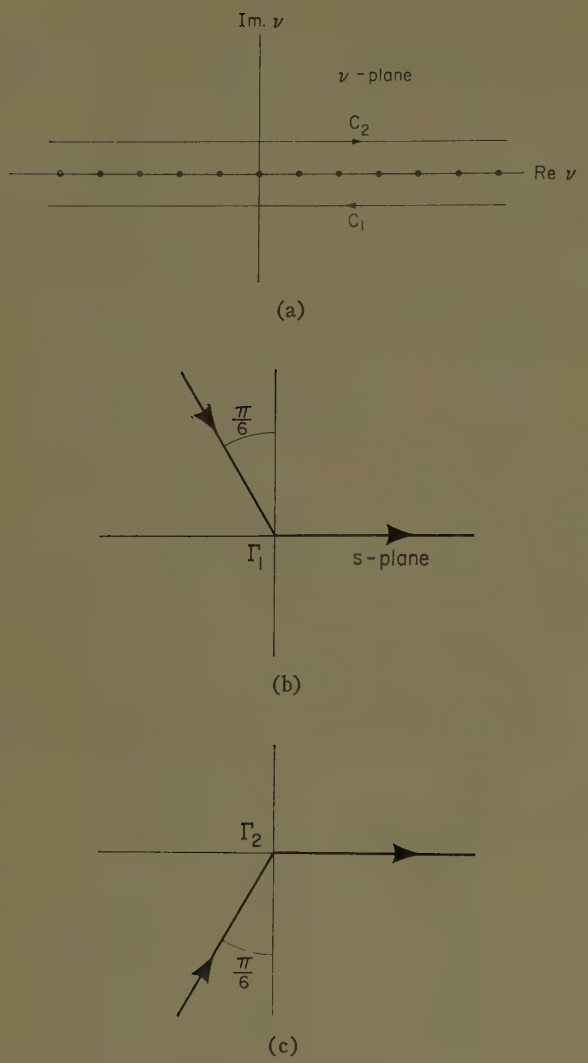

Fig. 9—Contours in complex plane.

Consequently,

$$F(x,\phi) = \frac{1}{\pi x}\int_{C_1} \frac{e^{i\nu\pi}}{\sin \nu\pi}\left[\frac{e^{-i\nu(\phi-\pi/2)} + e^{-i\nu(3\pi/2-\phi)}}{H_\nu^{(2)\prime}(x) + GH_\nu^{(2)}(x)}\right] d\nu. \quad (43)$$

For this contour, Im.$\nu<0$ and therefore, it is permissible to write

$$\frac{e^{i\nu\pi}}{\sin \nu\pi} = 2i\sum_{m=0}^{\infty} e^{-i\nu 2\pi m} \quad (44)$$

which leads to

$$F(x,\phi) = \frac{2i}{\pi x}\sum_{m=0}^{\infty}\left[T_m\left(\phi-\frac{\pi}{2}\right) + T_m\left(\frac{3\pi}{2}-\phi\right)\right] \quad (45)$$

where

$$T_m(\beta) = \int_{C_1} \frac{e^{-i\nu(\beta+2\pi m)}}{H_\nu^{(2)\prime}(x) + GH_\nu^{(2)}(x)}\, d\nu \quad (46)$$

with β being either $\phi-\pi/2$ or $3\pi/2-\phi$.

The so-called third order approximation for the Hankel functions is now introduced. This enables one to write[9,28]

$$H_\nu^{(2)}(x) \cong +\frac{i}{\pi^{1/2}}\left(\frac{2}{x}\right)^{1/3} W_1(t) \quad (47)$$

and

$$H_\nu^{(2)\prime}(x) \cong -\frac{i}{\pi^{1/2}}\left(\frac{2}{x}\right)^{1/3} W_1'(t) \quad (48)$$

where $W_1(t)$ and $W_1'(t)$ are Airy integrals defined by[29]

$$W_1(t) = \frac{1}{\pi^{1/2}}\int_{\Gamma_1} ds e^{st-s^3/3} \quad (49)$$

and

$$W_1'(t) = \frac{1}{\pi^{1/2}}\int_{\Gamma_1} sds e^{st-s^3/3} \quad (50)$$

in the notation of Fock where the quantity t is defined by

$$t = \left(\frac{2}{x}\right)^{1/3}(\nu - x).$$

In the foregoing text a function $W_2(t)$ was also employed. It has the same form as $W_1(t)$ but the contour Γ_1 is replaced by Γ_2 shown in Fig. 9(b) and 9(c), respectively. The function $T_m(\beta)$ can now be written

$$T_m(\beta) \cong -i\frac{\pi x}{2} e^{ix(\beta+2\pi m)} g(X_m) \quad (51)$$

where

$$g(X) = \frac{1}{\sqrt{\pi}}\int_{\Gamma_2} \frac{e^{-iXt}dt}{W_1'(t) - qW_1(t)} \quad (52)$$

with

$$q = -i(x/2)^{1/3}Z/\eta_0$$

and

$$X_m = (\beta + 2\pi m)\left(\frac{x}{2}\right)^{1/3}.$$

Therefore,

$$F(x,\phi) \cong \sum_{m=0}^{\infty} e^{-ika((\phi-\pi/2)+2\pi m)}\, g\left[\phi - \frac{\pi}{2} + 2\pi m\left(\frac{x}{2}\right)^{1/3}\right] + \sum_{m=0}^{\infty} e^{-ika((3\pi/2-\phi)+2\pi m)}\, g\left[\frac{3\pi}{2} - \phi + 2\pi m\left(\frac{x}{2}\right)^{1/3}\right] \quad (53)$$

[29] The Airy integral is related to the Hankel function of order $\frac{1}{3}$ by

$$W_1(t) = e^{-2\pi i/3}\sqrt{\frac{\pi}{3}}\,(-t)^{1/2}H_{1/3}^{(2)}\left[\left(\frac{2}{3}\right)(-t)^{3/2}\right].$$

which is valid for $\pi \geqq |\phi| \geqq \pi/2 - \Delta\phi$ where $(\Delta\phi)^3 \ll 1$. It is also readily shown that if $\pi(x/2)^{1/3} \gg 1$, only the term for $m=0$ need be retained.

For the shadow region ($X>0$) it is desirable to calculate the integral for $g(X)$ by the evaluation of the residues at the poles of the integrand. The poles t_s of the integrand are determined from

$$W_1'(t_s) - qW_1(t_s) = 0. \tag{54}$$

Expanding the denominator in a series around the pole $t=t_s$, leads to

$$W_1'(t) - qW_1(t) \cong [W_1''(t_s) - qW_1'(t_s)](t - t_s)$$

when terms containing $(t-t_s)^2$, $(t-t_s)^3$ have been omitted. But since

$$W_1''(t_s) - t_sW_1(t_s) = 0$$

and

$$W_1'(t_s) - qW_1(t_s) = 0$$

one may write

$$W_1''(t_s) - qW_1'(t_s) = (t_s - q^2)W_1(t_s) \tag{55}$$

and consequently

$$W_1'(t) - qW_1(t) \cong (t_s - q^2)W_1(t_s)(t - t_s) + \tag{56}$$

higher order terms in $(t-t_s)$.

For $X>0$, C can be deformed to a path enclosing the poles which are contained (as will be shown) in the fourth quadrant of the t plane. $g(X)$ is thus equal to the sum of the residues of the poles at $t=t_s$. Thus

$$g(X) = -2\sqrt{\pi}i \sum_s \frac{e^{-iXt_s}}{(t_s - q^2)W_1(t_s)}. \tag{57}$$

The numerical evaluation of the poles t_s, being a solution of

$$W_1'(t) - qW_1(t) = 0$$

has been discussed in detail by Fock. Actually, however, the task had been completed by Van der Pol and Bremmer a decade earlier. (The equation for the roots t_s arises also in the problem of a dipole located on the surface of an imperfectly conducting sphere.) Van der Pol and Bremmer's equation is

$$\delta e^{i\pi/3} \frac{H_{2/3}^{(2)}[(\frac{1}{3})(-2\tau_s)^{3/2}]}{H_{1/3}^{(2)}[(\frac{1}{3})(-2\tau_s)^{3/2}]} = -(-2\tau_s)^{-1/2} \tag{58}$$

where

$$\delta \cong -i\frac{(\eta_0/Z)}{(ka)^{1/3}}.$$

$H_{2/2}^{(2)}$ and $H_{1/1}^{(2)}$ are Hankel functions of the second kind of order 2/3 and 1/3. But, since

$$W_1(t) = e^{-2\pi i/3}\sqrt{\frac{\pi}{3}}(-t)^{1/2}H_{1/3}^{(2)}\left[\left(\frac{2}{3}\right)(-t)^{3/2}\right] \tag{59}$$

it readily follows that

$$t_s = 2^{1/3}\tau_s. \tag{60}$$

Although the notation of Van der Pol and Bremmer should have a historical priority, the Russian notation will be retained in the remainder of this Section. When $q=0$, the roots are determined simply from

$$W_1'(t_s) = 0$$

[or from $H_{2/3}^{(2)}[\frac{1}{3}(-2\tau_s)^{3/2}] = 0$].

These particular roots designated t_s^0 are well known.[4] The first five are given by

$$t_1^0 = 1.01879e^{-i\pi/3} \qquad t_4^0 = 6.16331e^{-i\pi/3}$$
$$t_2^0 = 3.24820e^{-i\pi/3} \qquad t_5^0 = 7.37218e^{-i\pi/3}.$$
$$t_3^0 = 4.82010e^{-i\pi/3}$$

A series expansion for t_s in terms of ascending powers of q can be obtained readily. For example, since

$$\frac{d}{dq}\left[\frac{dW_1(t)}{dt} - qW_1(t)\right]$$

$$W_1''(t)\frac{dt}{dq} - W_1(t) + qW_1'(t)\frac{dt}{dq} = 0 \tag{61}$$

and

$$W_1''(t) = +tW_1(t), \qquad W_1'(t) = qW_1(t)$$

it is seen that the differential equation for t_s is

$$\frac{dt}{dq} = \frac{1}{t - q^2}. \tag{62}$$

The resulting expansion is

$$t_s = t_s^0 + \frac{1}{t_s^0}q - \frac{1}{2(t_s^0)^3}q^2 + \left(\frac{1}{3(t_s^0)^2} + \frac{1}{2(t_s^0)^5}\right)q^3 \tag{63}$$

+ higher terms in q.

Other expansions for t_s and a very extensive tabulation is given in a monograph by Belkina.[25] The results given here should be adequate for most conditions in practice. There is some difficulty however, when X becomes small; this is near the shadow boundary. Here one must resort to a numerical integration of the integral for $g(X)$ since the residues converge poorly for small positive X and not at all for negative X.

ACKNOWLEDGMENT

The authors would like to thank K. A. Norton for his suggestions, John Harman and Mrs. Barbara Bolton for the drawing of the illustrations, and Mrs. Patricia Murdock for preparation of the manuscript.

Nonresonant Slotted Arrays*

ANDRE DION†

Summary—**The distribution of slot conductance of nonresonant arrays is obtained by considering the array as a continuous line source. Distributions of conductance per unit length for three Taylor aperture distributions are thus obtained. However, the discreteness of the array is retained for a discussion of second-order beams and for the development of a method leading to their suppression. The performance of an experimental array is described.**

Introduction

THE DESIGN of linear arrays having lengths of about ten wavelengths or more is generally facilitated by considering the array as a continuous line radiator. Also, provided the array is not too long, it is permissible to neglect the effects of small losses occurring inside the feeding arrangement, which further simplifies the design. However, because the array is made of discrete elements, it is possible that more than a single principal maximum will appear in the radiated field;[1] therefore it is necessary to retain the discrete elements representation of the array at least for a discussion on secondary maxima. Slotted arrays of lengths conforming to the above description are considered here. Design data for these arrays are presented in convenient forms and an experimental array based on them agrees well with expectation.

Second-Order Beams of Linear Arrays

The radiation pattern of linear arrays of discrete noninteracting elements may be expressed analytically as the product of two factors. One, the element factor, is the radiation pattern of a single element and generally has little directivity. The other, the space factor, is the radiation pattern of a similar array of point sources and is the factor controlling the directivity of the antenna. Referring to Fig. 1, where a linear array of N identical radiators with spacing d is considered, the product of these two factors is[2]

$$F(\phi,\theta)\sum_{n=0}^{N} C_n \exp\left[jn\left(\delta-\frac{2\pi}{\lambda}d\cos\phi\right)\right] \qquad (1)$$

with $F(\phi, \theta)$ as the element factor and the summation as the space factor. In this expression, C_n is the excitation coefficient of the nth radiator, δ is the phase difference between the exciting field of adjacent radiators, and λ is the free-space wavelength. The factor $(\delta-(2\pi/\lambda)d\cos\phi)$ in (1) is readily seen to be the phase difference between the far-field signals of two adjacent elements. The space factor is maximum when this difference corresponds to an integral number of wavelengths, *i.e.*,

$$\delta-\frac{2\pi}{\lambda}d\cos\phi_m=2\pi m \qquad (2)$$

where $m=0, \pm1, \pm2, \cdots$ and ϕ_m is the direction of the corresponding field maximum. Rearranging the terms, this direction is obtained from

$$\cos\phi_m=\frac{\lambda}{d}\left(\frac{\delta}{2\pi}-m\right). \qquad (3)$$

There may be more than one value of m yielding real values of ϕ_m, the amplitude of each of the resulting beams in the radiation pattern being proportional to the element factor. In general, the unwanted beams, called second-order beams, are appreciably reduced by this factor. However, in some designs the second-order beams may still be many times larger than the specified sidelobe level and therefore a method of eliminating or reducing them is required. Gruenberg[3] has proposed some methods of suppressing second-order beams, but in the following analysis the simpler method of limiting slot spacing is used and is shown to be practicable.

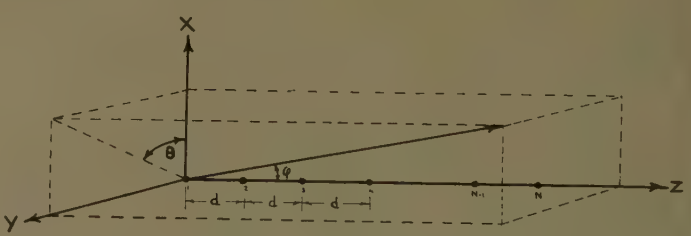

Fig. 1—Geometry of array of N identical elements.

In a slotted array antenna it is generally required to have the beam directed in some specified direction with respect to the array axis. This requirement is met by a proper choice of δ, d, and m in (3). The direction of the secondary beams nearest to the principal one is then obtained by replacing m by $m+1$ and $m-1$ in the same equation. Then

$$\cos\phi_{m+1}=\frac{\lambda}{d}\left[\frac{\delta}{2\pi}-(m+1)\right]=\cos\phi_m-\frac{\lambda}{d} \qquad (4)$$

* Manuscript received by the PGAP, February 9, 1958; revised manuscript received, June 23, 1958.

† Canadian Armament Res. and Dev. Establ., Valcartier, Quebec, Can.

[1] D. W. Fry and F. K. Goward, "Aerials for Centimeter Wavelengths," Cambridge Univ. Press, Cambridge, Eng., pp. 101–107; 1950.

[2] See, for example, S. Silver, "Microwave Antenna Theory and Design," M.I.T. Rad. Lab. Ser., McGraw-Hill Book Co., Inc., New York, N. Y., vol. 12, ch. 9; 1949.

[3] H. Gruenberg, "Second-order beams of slotted waveguide arrays," *Can. J. Phys.*, vol. 31, pp. 55–69; January, 1953.

and

$$\cos \phi_{m-1} = \frac{\lambda}{d}\left[\frac{\delta}{2\pi} - (m-1)\right] = \cos \phi_m + \frac{\lambda}{d} \qquad (5)$$

where ϕ_{m+1} and ϕ_{m-1} are the directions of the second-order beams situated one on the positive side, the other on the negative side of the principal beam, respectively. It is seen that the modulus of (4) and (5) may be larger than unity provided λ/d is large enough, and then the second-order beams are suppressed as they are in the imaginary region. For arrays made of elements radiating zero energy in the direction of the array axis, second-order beams can be avoided by choosing the slot spacing so that the second-order beam closest to the principal beam will be directed along this axis. The spacing d_0 corresponding to this condition is

$$d_0 = \frac{\lambda}{1 + |\cos \phi_m|} \qquad (6)$$

and is seen to be dependent on the direction of the principal beam. This dependence is illustrated in Fig. 2. Limiting the slot spacing to this chosen value will be a practical method of suppressing second-order beams, provided that the principal beam direction as given by (3) is practically obtainable by a proper choice of δ. This is generally the case, as the following discussion shows.

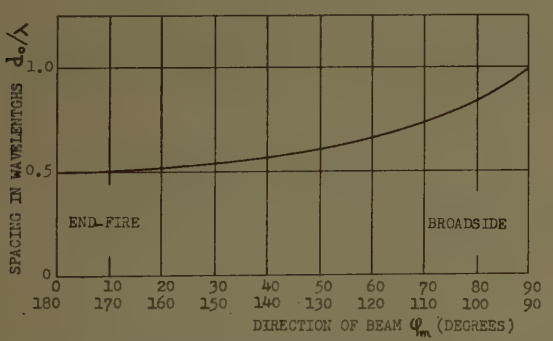

Fig. 2—Spacing between elements of a linear array vs principal beam direction.

In a slotted array fed from one end (negative z axis in the present analysis) and terminated by a matched load at the other end, the phase difference δ between the exciting field of adjacent slots is

$$\delta = \frac{2\pi d}{\lambda_g} \qquad (7)$$

where λ_g is the guide wavelength.

Subjecting d to the relation expressed by (6), the required value of δ may then be obtained by a proper choice of the guide wavelength. Substitution of (6) and (7) in (3) yields the following expressions for λ/λ_g:

$$\lambda/\lambda_g = \cos \phi_m + m(1 + \cos \phi_m) \qquad (8)$$

for 0 degrees $< \phi_m <$ 90 degrees, *i.e.*, for a beam tilted toward the load end of the array (forward-looking beam) and

$$\lambda/\lambda_g = \cos \phi_m + m(1 - \cos \phi_m) \qquad (9)$$

for 90 degrees $< \phi_m <$ 180 degrees, *i.e.*, for a beam tilted toward the generator end of the array (backward-looking beam).

The relations expressed by (8) and (9) are plotted in Fig. 3. These plots give the relation that must exist between λ/λ_g, m, and ϕ_m in order that the nearest second order beam be directed along the 0-degree axis for a beam tilted toward the generator end, or along the 180-degree axis for a beam tilted toward the load end of the array.

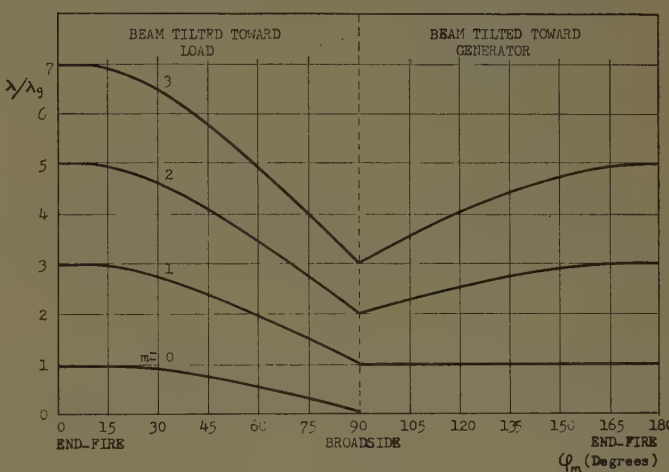

Fig. 3—The relation between λ/λ_g, the beam order m and the direction ϕ_m of the beam.

It is noted that for $m=0$ the method is useful for forward-looking beams only. For $m>0$ it can be used for all directions of the beam. The value $m=1$ has a peculiarity in that for a backward-looking beam the required ratio λ/λ_g is equal to unity for all values of ϕ_m. In effect for these particular values of m and λ/λ_g the second-order beam is directed along the 0-degree axis independently of λ/d. This can be seen by substituting in (5) the value of δ from (7) to give

$$\cos \phi_{m-1} = \frac{\lambda}{\lambda_g} - \frac{\lambda}{d}(m-1) = 1.$$

Practical values for m are 0 and 1. It is not advisable to use values of m much larger than 1 as loading of the guide with a high dielectric constant material would be required to produce the extra phase shift in the line and such material presents losses that are generally objectionable.

For a forward-looking beam, the choice between $m=0$ and $m=1$ depends on practical considerations. For instance, for a near-broadside beam, taking $m=0$ would be impractical as it corresponds to large values of guide

wavelength where sensitivity to frequency shift is high. The choice of $m=1$ is then logical.

The required value of λ/λ_g is obtained by a proper choice of the guide dimensions and of the dielectric constant of the material filling the guide. For the particular case of rectangular waveguides operated in the dominant mode, the ratio of the wavelength in the unbounded medium of dielectric constant ϵ to the wavelength in the guide is normally near 0.7 and therefore the ratio of free-space wavelength to guide wavelength is

$$\lambda/\lambda_g = 0.7\sqrt{\epsilon}, \tag{10}$$

a relation from which the dielectric constant is determined. The availability of low-loss dielectric materials of adjustable dielectric constant makes the above method of eliminating second-order beams practicable, at least for arrays of lengths such that dielectric losses are not prohibitive.

Amplitude Distribution

The shaping of the radiation pattern of a linear array is generally done by exciting the elements of the array in a distribution such as Taylor or Dolph-Tchebycheff. A Taylor[4] distribution, which implies that the array of discrete elements is considered as a line source, was selected for this investigation. This approximation is well justified in arrays made of about twenty elements or more. Eq. (1) for the radiation pattern of linear arrays is easily converted into the form studied by Taylor. Consider the array of Fig. 1 to be replaced by a line source of length $2l$ and having a similar but continuous phase and amplitude distribution. The amplitude of the field produced at a distant point in a direction ϕ, θ, by a distribution $f(x)$ of the amplitude along such a line source, where x is the distance from the center of the line source, is proportional to

$$F(\phi, \theta) \int_{-l}^{l} f(x) \exp\left[\frac{j2\pi x}{\lambda}(\cos\phi_m - \cos\phi)\right] dx \tag{11}$$

where ϕ_m is the direction of the beam maximum obtained from (2) and $F(\phi, \theta)$ is the element factor.

Substituting

$$u = \frac{2l}{\lambda}(\cos\phi_m - \cos\phi) \tag{12}$$

and

$$p = \frac{\pi x}{l} \tag{13}$$

yields for the space factor an expression proportional to

$$\int_{-\pi}^{\pi} f(p) e^{jpu} dp$$

which is the form studied by Taylor. The Taylor amplitude distributions of line sources have been computed for space factors of 20, 25, and 30 db sidelobe ratio and are:

$$(p)_{20\text{db}} = 1 + 0.260\cos p + 0.043\cos 2p - 0.049\cos 3p + 0.026\cos 4p \tag{14a}$$

$$f(p)_{25\text{db}} = 1 + 0.443\cos p - 0.011\cos 2p - 0.013\cos 3p + 0.010\cos 4p \tag{14b}$$

$$f(p)_{30\text{db}} = 1 + 0.581\cos p - 0.030\cos 2p + 0.003\cos 3p + 0.002\cos 4p. \tag{14c}$$

The parameter $\bar{n}$ of Taylor's paper, which determines the boundary of the region of uniform sidelobes, was taken as 5 for reasons given in his paper. This parameter also determines the term at which the Fourier series representing the amplitude distribution $f(p)$ terminates.

Beamwidth of Nonresonant Arrays

The beamwidth of a line source antenna of optimum design and with broadside radiation (resonant array) was shown by Taylor to be a function of the sidelobe ratio and of the parameter $\bar{n}$. The beamwidth of nonbroadside arrays, however, also depends on the squint angle of the beam. As the beam direction departs from the normal to the array, its beamwidth increases. The amount of broadening may be obtained from (12). The space factor $\int_{-\pi}^{\pi} f(p)e^{jpu}dp$ is maximum for u equal to zero or $\phi=\phi_m$ and symmetrical about the $u=0$ axis. Let u_0 be the value of u for which the space factor is halved and β the corresponding beamwidth; then

$$u_0 = \frac{2l}{\lambda}\left[\cos\phi_m - \cos\left(\phi_m + \frac{\beta}{2}\right)\right]$$

and

$$-u_0 = \frac{2l}{\lambda}\left[\cos\phi_m - \cos\left(\phi_m - \frac{\beta}{2}\right)\right]$$

and for small values of the beamwidth the above expressions yields

$$\beta = \frac{\lambda\mu_0}{l\sin\phi_m} = \frac{\beta_0}{\sin\phi_m} \tag{15}$$

where β_0 is the beamwidth of a similar broadside array.

The ratio of beamwidth β of nonresonant arrays to the beamwidth β_0 of equivalent broadside arrays as a function of the squint angle, ϕ_m, is shown in Fig. 4.

Conductance of Elements of Nonresonant Arrays

The computation of the conductance of the slots of a waveguide array to produce a given aperture distribution is a tedious task when performed for each slot in succession. Considerable effort is saved if the array is considered again as a continuous radiator and the con-

[4] T. T. Taylor, "Design of line-source antennas for narrow beamwidths and low sidelobes," IRE Trans. on Antennas and Propagation, vol. AP-3, pp. 16–28; January, 1955.

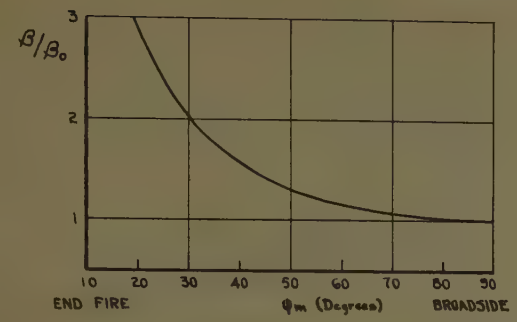

Fig. 4—Beamwidth of nonresonant arrays as a function of the direction of the beam.

ductance per unit length calculated. This is permissible for nonresonant arrays made up of elements having small or no mutual interaction (*e.g.*, longitudinal shunt slots) and comprising a sufficient number of slots. The conductance of each slot is then small and each one produces only negligible reflection. When such an array is terminated in a matched load, it can be considered to be matched throughout its length; under this condition, the conductance may be found from the relation[5]

$$g(x) = \frac{P(x)}{P_0(x)} \tag{16}$$

where $P(x)$ is the power radiated per unit length, $P_0(x)$ is the power in the guide, and $g(x)$ is the normalized conductance per unit length at a distance x from the center of the array.

The power radiated per unit length is obtained from the desired amplitude distribution $f(x)$ and may be written

$$P(x) = K[f(x)]^2 \tag{17}$$

where K is a constant. The power in the guide at a distance x from the center of the array may be immediately written

$$P_0(x) = 1 - \int_{-l}^{x} K[f(x)]^2 dx \tag{18}$$

where unit input power to the array is assumed and the guide is considered to be lossless. In order that the slot conductance be small, it is necessary that the power radiated by a given slot be small when compared to the power in the guide at this slot position. This imposes the condition that some power be absorbed in a load terminating the array. If r is the fraction of power absorbed by this load, the following relation may be written

$$1 - r = \int_{-l}^{l} K[f(x)]^2 dx \tag{19}$$

from which the proportionality constant K is evaluated. Substituting this value in (17) and (18) and using the resulting expressions with

$$p = \frac{\pi x}{l}$$

in (16) yields the following expression for the normalized conductance per unit length times half the array length:

$$lg(p) = \frac{\pi[f(p)]^2}{\frac{1}{1-r}\int_{-\pi}^{\pi}[f(p)]^2 dp - \int_{-\pi}^{p}[f(p)]^2 dp}. \tag{20}$$

This result, it is recalled, applies only to cases where the guide is filled with nonlossy material and where wall losses are assumed to be negligible. Substitution in (20) of the expressions for $f(p)$ given by (14) yields, after integration, expressions for the normalized conductance per unit length of slotted waveguide arrays of optimum design with sidelobe ratios of 20, 25, or 30 db. The expressions thus obtained for the conductance per unit length multiplied by half the array length are plotted in Figs. 5–7 for various percentages of power absorbed in the terminating load.

The normalized conductance of a given slot of the array is obtained by multiplying the normalized conductance per unit length at that slot position by the spacing d_0, between two consecutive slots, or

$$\text{slot normalized conductance} = lg(p)\frac{d_0}{l} = \frac{lg(p)}{N/2} \tag{21}$$

where N is the total number of slots. Therefore, to obtain the normalized conductance of each slot of the array from the graphs of Figs. 5–7, it is only necessary to divide the abscissa between $-\pi$ and π into a number of spacings equal to the number of slots minus one and to read the corresponding ordinate divided by a number equal to half the total number of slots.

Voltage Standing Wave Ratio of Terminating Load

It is necessary, for reasons expressed above, to terminate a nonresonant array into a matched load. When this load is not perfectly matched, a reflected wave propagates in the reverse direction in the waveguide and is partly radiated outside, thus interfering with the field produced by the direct wave and deteriorating the pattern. Because of the reversal of the direction of propagation, the reflected wave produces a radiation pattern with a beam pointing in a direction opposite (with respect to the array normal) to the design beam direction but tilted by the same amount. In this direction the amount of interference is largest and the total field is the phasor addition of the sidelobes generated by the direct wave and of the beam generated by the reflected wave. An estimate of the maximum VSWR allowable may be obtained by calculating the load VSWR for which the beam produced by the reflected wave is equal in amplitude to the design sidelobe level. The result of

[5] Fry and Goward, *op. cit.*, p. 113.

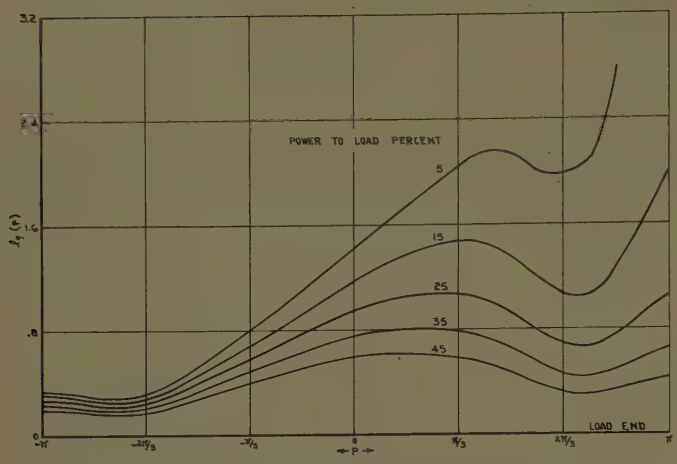

Fig. 5—Conductance distribution of elements of a nonresonant slotted array designed for 20-db sidelobe ratio.

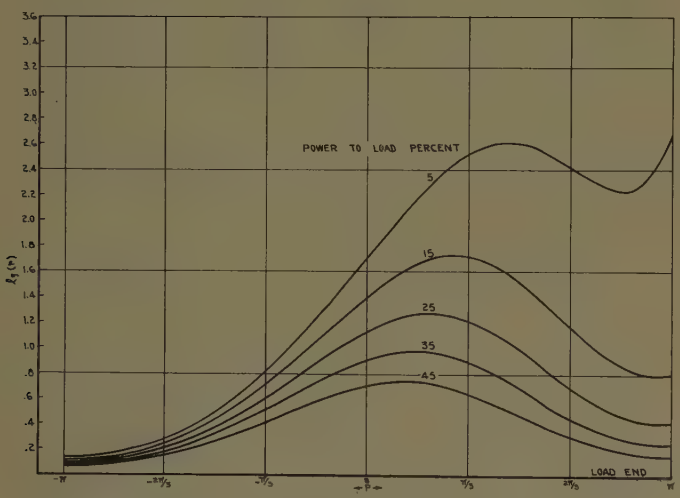

Fig. 6—Conductance distribution of elements of a nonresonant slotted array designed for 25-db sidelobe ratio.

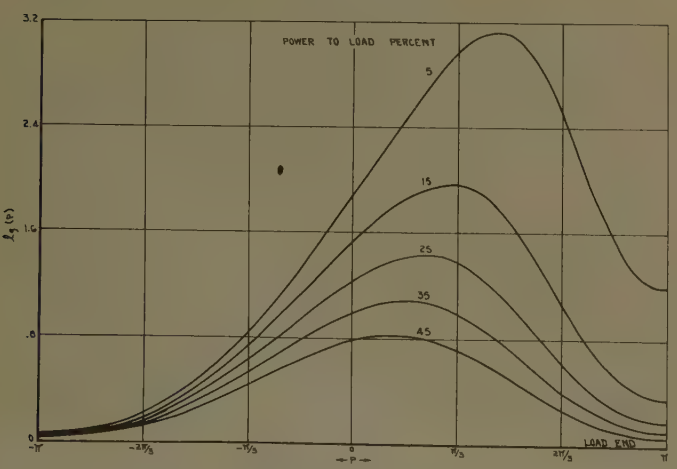

Fig. 7—Conductance distribution of elements of a nonresonant slotted array designed for 30-db sidelobe ratio.

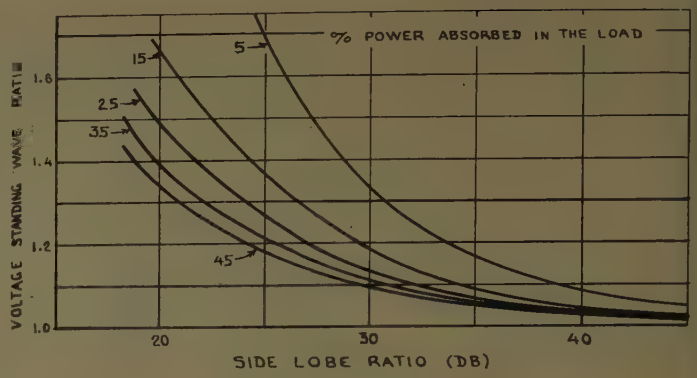

Fig. 8—VSWR of load vs sidelobe ratio for different percentages of power to load.

this calculation is shown in Fig. 8 which indicates that, except for large sidelobe ratios and low efficiencies, the VSWR is not too critical.

Experimental Results

A slotted waveguide array was constructed to determine the errors introduced by considering the array of discrete elements as a line source. The design parameters chosen for this array are: sidelobe ratio 30 db, beamwidth 6 degrees, tilt angle 30 degrees, *i.e.*, $\phi_m = 60$ degrees, efficiency 65 per cent, frequency X band.

The array was made of resonant slots cut longitudinally in the wide face of a guide, the spacing between the slots obtained from (5) or Fig. 2 being $2\lambda/3$. For this value of spacing, the second-order beam is directed along the array axis and its amplitude is reduced to zero since the radiation of a longitudinal slot in this direction is zero. However, because of the relatively large beamwidth of the second-order beam in this direction and because the field of a slot is still appreciable at angles close to the array axis, it is necessary to make the spacing between slots a little less than the value indicated above. Thus the second-order beam may be thrown further into the imaginary region so that no part of it greater than the design sidelobe level remains in the visible range. The amount by which the spacing must be decreased depends on the sidelobe ratio, on the beamwidth, and on the radiation pattern of a single element, and is generally small in most cases. It is not advisable to make the slot spacing much less than the value obtained from these considerations because of the increased amount of interaction which results when the slots are too close. Higher order waves inside the guide are excited by the slots. Increased interaction results when the higher order waves are not sufficiently attenuated in the distance between two consecutive slots.

The tilt angle of the beam determines the ratio of free-space wavelength to guide wavelength. From Fig. 3 it is seen that a value of $\frac{1}{2}$ for this ratio satisfies the requirement. For this particular value the required guide wavelength was easily obtained by a suitable

choice of the guide dimensions at the design frequency. No dielectric loading was required.

The design beamwidth was found to be realizable with an array of 20 slots. The displacement y of a slot from the center of the guide was obtained from Stevenson's formula,[6,7]

$$g = 2.09 \frac{a\lambda_g}{b\lambda} \cos^2\left(\frac{\pi\lambda}{2\lambda_g}\right) \sin^2\left(\frac{\pi y}{a}\right) \qquad (22)$$

where a and b are the wide and narrow dimensions of the guide and the conductance g is obtained from the proper curve of Fig. 7. The distance between two consecutive slots was too small to permit introducing another slot midway between them and displaced on the other side of the center line, and therefore the array was single-row.

The experimental H-plane pattern of the antenna is presented in Fig. 9 where it is compared with the theoretical pattern. This pattern was taken in the longitudinal plane perpendicular to the guide surface (*i.e.*, $\theta = 0$). Measurements taken in planes inclined with respect to this last plane were also taken and did not reveal the presence of second-order beams. Because the radiation is omnidirectional in one plane, the accurate measurement of small sidelobes was awkward due to the difficulty of eliminating small reflections from the ground and surrounding objects. These reflections may be responsible for the small discrepancies observed close to the beam. At large angles from the beam, agreement is not to be expected because the theoretical pattern is derived on the basis of a continuous line source, a derivation which does not reveal the effect of second-order beams and therefore cannot predict the behavior at large angles. The proper matching of the terminating load is indicated by the absence of an increase of radiation at an angle of 120 degrees which is the direction where the beam produced by a load reflection should be found.

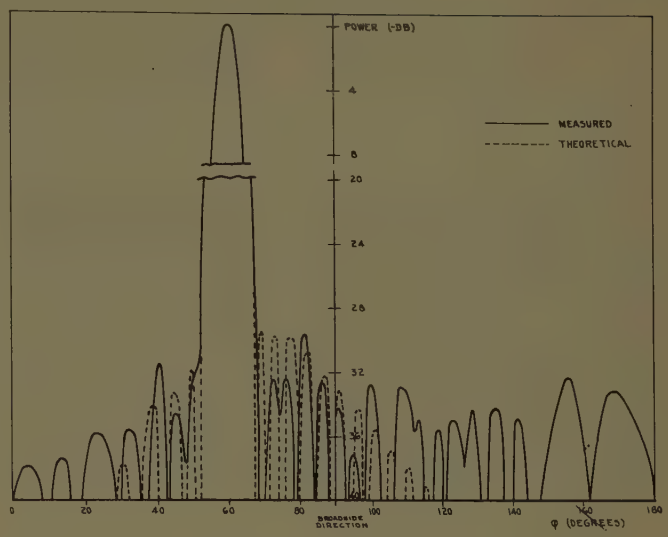

Fig. 9—Principal H-plane pattern of experimental array.

Conclusion

Data useful to the design of nonresonant arrays have been developed and presented in convenient form. It has also been shown that limiting the slot spacing is an appropriate method for suppressing second-order beams. In cases where dielectric loading of the guide is needed, the method is still practicable for arrays of lengths in which dielectric losses are not prohibitive.

Acknowledgment

The permission of Canadian Armament Research and Development Establishment to publish this paper is gratefully acknowledged. The author wishes to thank J. J. Maroney and his group for carrying out some of the computation involved in this paper, and M. Rouillard for his assistance in measuring the radiation patterns. He also wishes to express his sincere appreciation to Drs. R. E. Collin and W. J. Surtees for their interest and useful comments.

[6] A. F. Stevenson, "Theory of slots in rectangular waveguides," *J. Appl. Phys.*, vol. 19, pp. 24–38; January, 1948.

[7] A. A. Oliner, "The impedance properties of narrow radiating slots in the broad face of rectangular waveguide," parts I and II, IRE Trans. on Antennas and Propagation, vol. AP-5, pp. 4–20; January, 1957.

Gains of Finite-Size Corner-Reflector Antennas*

H. V. COTTONY† AND A. C. WILSON†

Summary—An experimental corner reflector was erected at the Table Mesa antenna range near Boulder. The aperture angle of this antenna was made adjustable to any value between 20 and 180 degrees. The widths and lengths of the reflecting surfaces were each adjustable from 0.4 to 5.0 wavelengths. Measurements of gain were made for numerous combinations of lengths and widths of reflecting surfaces. These measurements were made with a half-wave dipole in the first, second and third maximum positions. The aperture angle was adjusted to maximize the gain. The principal results are presented in the form of contours of constant gain plotted for a range of widths and lengths of reflecting surfaces from 0.4 to 5.0 wavelengths. These graphs should be useful to a designer of corner-reflector antennas.

Introduction

VARIOUS aspects and applications of corner-reflector antennas have been described in numerous papers. The literature[1–3] presents the more important features of this type of antenna. While the volume of technical literature dealing with this antenna is extensive, a systematic and detailed investigation of the effect of the lengths and widths of reflecting surfaces on the gain realizable from a corner-reflector antenna has not been reported. Neither is there any record of experimental measurements on corner-reflector antennas having values of aperture angle other than those obtained by dividing 180 degrees by an integer, *i.e.*, 90, 60, 45, etc., degrees.

In 1952 and 1953 measurements of gain of various corner-reflector antennas were carried out at the NBS model antenna range at Sterling, Va. The purpose of these measurements was to aid in selecting the size of reflecting surfaces and the value of the aperture angle for corner-reflector antennas to be used with some of the VHF ionospheric scatter circuits, then being installed for the U. S. Air Force. Because the corner-reflector antenna continues to be a useful type for this application, additional measurements were carried out in 1956. These experiments combine the study of the size of reflecting surfaces with the value of aperture angle required to maximize the gain.

The term "gain" as employed here denotes power gain as defined by IRE (1948). However, a half-wave dipole rather than an isotropic radiator is used as the standard.

* Manuscript received by the PGAP, March 26, 1958. This work has been carried out on behalf of and has been supported by the U. S. Air Force Communication System, Strategic Communication System Engineering Organization. The results represent a part of the supporting work of the Natl. Bur. of Standards in connection with establishment of the U. S. Air Force transatlantic VHF ionospheric scatter system.

† Natl. Bur. of Standards, Boulder, Colo.

[1] J. D. Kraus, "The corner-reflector antenna," PROC. IRE, vol. 28, pp. 513–519; November, 1940.

[2] E. B. Moullin, "Radio Aerials," Oxford University Press, London, Eng.; 1949.

[3] J. D. Kraus, "Antennas," McGraw-Hill Book Co., Inc., New York, N. Y., pp. 324–352; 1950.

Experimental Procedure

The measurements were carried out at 400 mc. The corner reflector consisted of two lattice-type wooden frames, each five wavelengths (12.28 feet) wide by five wavelengths long, supporting the reflecting surfaces. The reflecting surfaces were made of overlapping strips of sheet aluminum fastened to these frames in such a manner that each strip added 0.2 wavelength to the length of the reflecting surface. Fig. 1 illustrates the terminology.

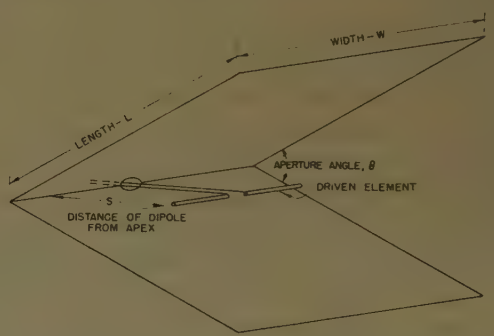

Fig. 1—Diagram of a corner-reflector antenna showing the nomenclature and the symbols used in the text.

Fig. 2 is a view of the experimental corner-reflector antenna employed in these measurements. The lengths of the reflecting surfaces were varied by adding or removing the strips. The width was varied by trimming the lengths of the strips. The two frames were pivoted along the same axis and the aperture angle was adjustable from 20 to 180 degrees.

The driven element was a folded half-wave dipole. Its position within the corner, S, measured from the apex could be varied from approximately 0.07 to 2.5 wavelengths. The support for the dipole served also as a balun transformer. It was designed to transform the impedance of the dipole to approximately 50 ohms. A two-stub tuning unit was employed to attain an exact match to the 50-ohm line. The gain of the corner-reflector antenna was measured by comparing its response with that of an antenna, the gain of which was accurately known. Corrections for variations in system sensitivity with time were made by comparison with a nearby reference antenna. The details of the method of gain measurement were described in a recent paper.[4]

The bulk of the measurements consisted of determinations of gains realizable with the reflecting surfaces of given widths and lengths, with the dipole in each of the first three positions which gave maximum response and with the aperture angle adjusted to maximize the

[4] H. V. Cottony, "Method for accurate measurement of antenna gain," presented at URSI Meeting, Washington, D. C.; May 1, 1956.

Fig. 2—A view of the experimental corner-reflector antenna.

gains for each position. Additional measurements were carried out to trace the changes in the locations of the three dipole "maximum positions" with changes in the aperture angle. Some measurements were carried out to determine the effect of the aperture angle on the gain, with the size of the reflecting surfaces held constant.

Results

The principal results of this series of measurements are represented by the data on the gains realizable from corner reflectors of various lengths and widths. This material is presented in a manner which should permit a designer to select the size of corner reflector best suited to his application, considering both performance and economy in size. The work also led to a better understanding of the various "maximum positions" of the dipole and of the changes in gain with continuous variations of aperture angle.

The Effect of Aperture Angle on the Optimum Position of the Dipole

As is well known, in order to get maximum gain in the forward direction from a corner-reflector antenna having a given angle of aperture, the dipole may be at one of several specific distances from the apex of the corner. These locations are usually referred to as "first position," "second position," "third position," etc. The first position is relatively broad and involves a compromise. The directivity actually improves as the dipole is brought very close to the apex; however, the radiation resistance becomes quite low and the losses reduce the gain. If the position of the dipole is displaced from the optimum in the direction away from the apex, the gain is reduced first by the broadening and, when the displacement is further increased, by the splitting of the main beam. The second and higher order maxima correspond to points at which the direct radiation and reflected radiation add most favorably in the forward direction. These points are very much more sharply defined than is the location of the first position.

The earlier of these series of measurements were carried out using reflecting surfaces 5 wavelengths wide by 5 wavelengths long, with the purpose of tracing the location of the first, second, and third maximum positions with varying aperture angles. However, it was found that the dimensions of the reflecting surfaces did not materially affect the optimum position of the dipole. Fig. 3 presents the results of these tests. The first position is found to be rather broad and poorly defined with the minimum value of 0.10 to 0.15 for an angle of 180 degrees. It is a continuous function, the distance from the axis increasing as the angle of aperture is made smaller.

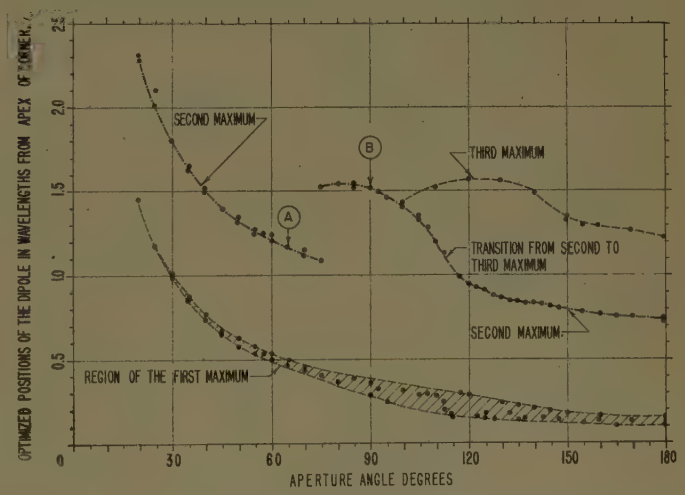

Fig. 3—Locations of the three dipole positions as functions of aperture angle. A) Point of greatest gain for second position ($\phi = 65°$; $S = 1.17\ \lambda$). B) Point of greatest gain for third position ($\phi = 90°$; $S = 1.50\ \lambda$).

The second position is found to be a discontinuous function. Its position roughly parallels the first position, but for aperture angles between 120 and 100 degrees the second position moves out to meet the third position. The second position is found to reappear again for an aperture angle of approximately 75 degrees and continue to the smallest angle measured (20 degrees).

For an aperture angle of 180 degrees, the third position is located at 1.25 wavelengths. The variation in its position with changes in aperture angle is somewhat irregular, being affected by the second position which joins it at a point corresponding to an angle of aperture equal to 100 degrees. The third position is found to disappear when the aperture angle is decreased below 70 degrees. It cannot be traced beyond this point because the limit of available dipole movement, 0–2.5 wavelengths, was insufficient to reach it. (At an aper-

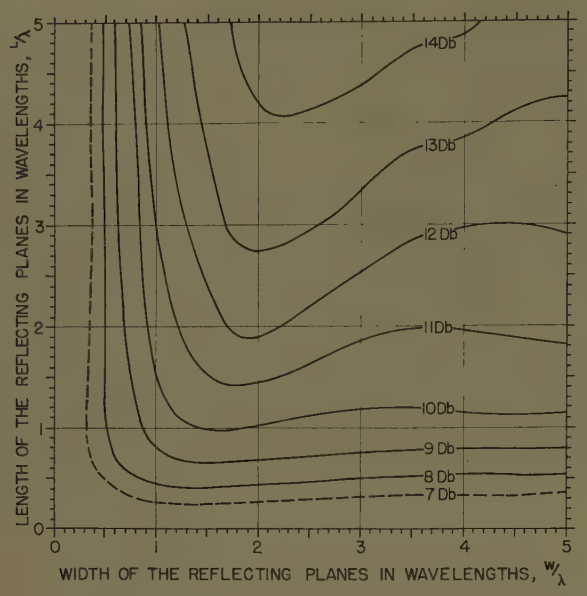

Fig. 4—Contours of constant gain for corner-reflector antenna with dipole in first position for various reflector sizes. The aperture angle adjusted for maximum gain in each case. The optimum value of aperture angle, in general, diminishes with increase in the length of reflecting surfaces.

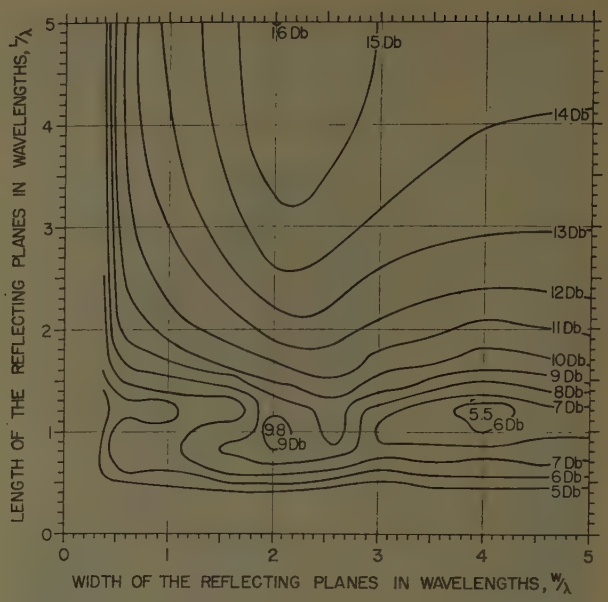

Fig. 6—Contours of constant gain for corner-reflector antenna with dipole in second position for various reflector sizes. The aperture angle adjusted for maximum gain in each case. For lengths greater than 1 wavelength, the optimum value of aperture angle has been found to be 65 degrees.

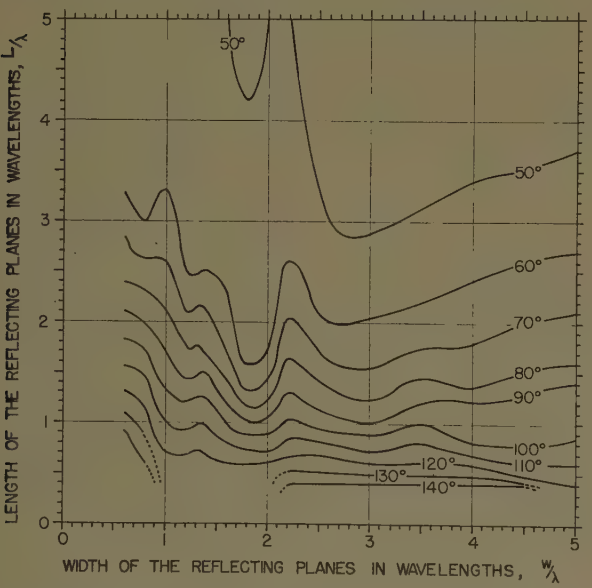

Fig. 5—Contours of aperture angle required to optimize the gain of a corner-reflector antenna, with dipole in first position, for various reflector sizes.

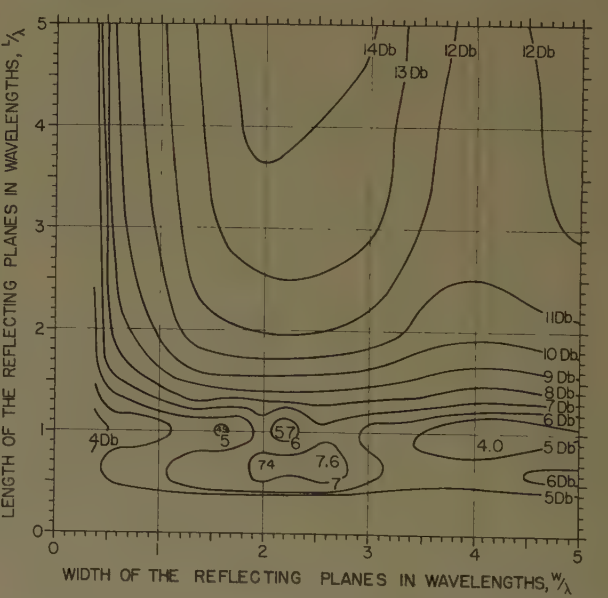

Fig. 7—Contours of constant gain for corner-reflector antenna with dipole in third position for various reflector sizes. The aperture angle adjusted for maximum gain in each case. For lengths greater than about 0.5 wavelength, the optimum value of aperture angle has been found to be 90 degrees.

ture angle of 60 degrees the third position is theoretically predicted to be 2.6 wavelengths away from vertex.)

With the dipole in the first position, the aperture angle required to maximize the gain is a function of the length of the reflecting planes, the larger the planes the smaller the optimum angle and the greater the realized gain. With the dipole in the second position, on the other hand, the maximum gain is realized when the angle of aperture is adjusted to 65 degrees regardless of the size of the reflecting planes, provided these are larger than about 1 wavelength in length and width. The maximum is well defined and a change of aperture angle in either direction by 5 degrees results in a reduction in gain of the order of 0.3 db. With the dipole in the third position there is likewise one optimum value of aperture angle for which the gain is maximized. This value is found to be 90 degrees and is valid for all sizes of reflecting planes longer than 0.5 wavelength.

It should be noted that with moderate-size corner reflectors, the relationship between gain and the size of the reflecting planes and that between gain and the angle of aperture, although continuous, is not smooth, but contains numerous small-scale (of the order of 0.1

db) real variations superimposed upon the major variation. The results presented in this report have been smoothed to remove these small-scale variations.

The Effect of Dimensions of the Reflecting Surfaces on the Gain

The gains realizable with a corner-reflector antenna having various combinations of length and width of reflecting surfaces are presented in Figs. 4, 6, and 7. Fig. 4 represents results obtained with the dipole in the first position. Since the optimum aperture angle in this case depends on the length and, to a lesser extent, on the width of the reflecting surfaces, the optimum values of aperture angle are presented in Fig. 5. Figs. 4 and 5 should be used together, *i.e.*, to realize the gain of a corner-reflector antenna with reflecting planes having length, L, and width, W, which is given by Fig. 4, the aperture angle must be adjusted to values given in Fig. 5 for corresponding length and width. The location of the dipole, in its turn, should be selected from Fig. 3 corresponding to the aperture angle which, in turn, is obtained from Fig. 5.

The gains realizable using a corner-reflector antenna with its dipole in the second position are presented in Fig. 6. For all sizes of reflecting surfaces greater than approximately 1 wavelength long by 1 wavelength wide, the maximum gain was realized with the aperture angle optimized at 65 degrees, and with the dipole 1.17 wavelengths from the apex. For very small corner reflectors the optimized value of aperture angle was irregular and because of the relative unimportance of such corners no attempt is made to present the data on the exact values of the aperture angle for small corner-reflector antennas with dipole in the second position.

Fig. 7 presents the gains of the corner-reflector antenna with the dipole in the third position. As in the preceding case, the aperture angle optimizes at very nearly the same value for all combinations of length and width greater than about 0.5 wavelength. In the case of the dipole in the third position, the optimum value was found to be 90 degrees with the dipole position 1.5 wavelengths away from the corner.

Conclusions

To be of practical use, a corner reflector should have a width of at least 0.5 wavelength. Considerable improvement in gain is realized if the width is increased to a full wavelength. Beyond that, the increase in gain with increase in width is much slower, and beyond a certain point an additional incremental increase in width may actually result in a decrease in gain. The phenomenon can be understood by applying the concept of Fresnel zones on the reflecting planes.

In the case of the dipole in the first position the relationship between the length of the surfaces and the gain is simple: The gain increases monotonically with increase in length. In the cases of the dipole in the second and third positions, the same relationship holds true generally except for lengths of less than 1.5 wavelengths. For these shorter lengths the relationship is irregular. Using the dipole in the first position, the optimum aperture angle depends on the size of the corner, particularly its length. Using the dipole in the second position, the optimum aperture angle is 65 degrees for reflectors of length greater than 1 wavelength. With the dipole in the third position the optimum aperture angle is 90 degrees for reflectors having length greater than approximately 0.6 wavelength.

If the designer's goal is maximum gain along the forward axis, there may be an advantage in employing a corner-reflector antenna with the dipole in the second position. To realize this advantage the lengths of the reflecting surfaces should be greater than 2 wavelengths. The widths of the reflecting surfaces should be approximately 2 wavelengths. For smaller corner reflectors there is an advantage from the standpoint of gain in the use of an antenna having its dipole in the first position. There do not appear to be any advantages in placing the dipole in the third position.

Acknowledgment

The measurements were carried out with the assistance of J. E. Chukoski, E. Rollison, and W. L. Martin Their part in this work has been very much appreciated

Scanning Surface Wave Antennas—Oblique Surface Waves Over a Corrugated Conductor*

R. W. HOUGARDY† AND R. C. HANSEN†

Summary—**The existence of a surface wave which propagates across a corrugated metallic surface at an oblique angle with the teeth is investigated both experimentally and theoretically in this paper. Expressions are derived which give the variation of the wave velocity and amplitude with the change of wave direction. Experimentally measured values of the surface velocity compare favorably with the theory.**

The radiation pattern of an experimental antenna is given which demonstrates that a low sidelobe, narrow azimuth beam scannable to ±30 degrees with a cosecant-squared elevation pattern is attainable. A method of feeding this antenna to give a low silhouette, making the corrugated scanner antenna suitable for flush mounted applications is illustrated.

Introduction

SURFACE wave antennas in their most common form consist of a finite width and length of trapping surface, usually planar, which may or may not be imbedded in a ground plane. Some device, *e.g.*, a waveguide horn, dipole array, or pillbox, is used to excite a surface wave at one end of the trapping surface with the energy end firing off the opposite end.

Patterns produced by surface wave antennas are fan beams, with the pattern in the plane of the surface being approximately that of the feed. Gain may be maximized by adjusting the phase velocity of the surface wave along the trapping surface to give a net phase shift of 2.921 radians (the Hansen-Woodyard condition); however, in this region the gain is changing slowly so a small deviation from the 2.921 figure will not reduce the gain significantly. The gain is directly proportional to the length of the surface, and is $G \simeq 4.83\ l/\lambda$. Beamwidth,[1] in a plane perpendicular to the surface, is approximately inversely proportional to square root of length, with typical minimum figures being 15 degrees for $l = 4\lambda$ and 10 degrees for 10λ. A finite length of traveling wave radiator either in free space or attached to a finite ground plane has the characteristic end fire pattern tilted above the surface plane, due to diffraction of the wave at the end of the surface; the maximum beam tilt is inversely proportional to square root of length (as is the beamwidth) and is given by $\theta_{\text{tilt}} \simeq 124°/\sqrt{kl}$.

Traveling-wave end fire antennas trade the height of an equivalent two-dimensional slot array or dish for length in the beam direction, and while the end fire antennas are not capable of producing very narrow elevation beams, their low height or silhouette (often less than two wavelengths) adapts them to flush mounting on air frames and missile bodies. The most often used trapping surface is a corrugated metallic sheet where the teeth can, if desired, be filled with a low loss ceramic material.

Two points justify the use of surface, or slow, waves. First, the use of a trapping surface allows the elevation pattern to be shaped, with a cosecant square being typical of what can be accomplished by slight modification (curving and tapering) of the trapping surface. Second, the maximum end fire gain condition requires a slow wave with velocity given by $v/c = 1/(1+2.921/kl)$; *e.g.*, for a maximum gain antenna of length 10λ, the ratio should be 0.955.

Qualitative Discussion of Theory

Surface wave propagation over a corrugated metallic ground plane has been studied quite extensively during recent years;[1–7] Elliott[1] has presented a list of earlier papers. These authors have been concerned with the problem where the direction of wave propagation across the surface is normal to the corrugations.

Present requirements for flush mounted antennas demand that it be possible to scan the beam of such an antenna in the plane of the surface, which, in the case of a corrugated conductor antenna, means that the wave propagation direction will not always be normal to the corrugations, but must be along the direction of the scan angle. (See Fig. 1.) Questions have been raised about whether surface waves can exist when propagated at an angle across the corrugations. It was the original purpose of this work to demonstrate that such modes could satisfy the boundary conditions. In the last section the propagation of a skew surface-wave across a corrugated metallic surface is analyzed. The analysis indicates that

* Manuscript received by the PGAP, August 2, 1957; revised manuscript received, June 5, 1958. This research was supported by the AF Cambridge Res. Center, Air Res. and Dev. Command, Cambridge, Mass., under Contract AF19(604)-1317, and is an extract from Hughes Aircraft Co., Culver City, Calif., Scientific Rep. 13 of the same title.

† Microwave Lab., Hughes Aircraft Co., Culver City, Calif.

[1] R. S. Elliott, "On the theory of corrugated plane surfaces," IRE TRANS. ON ANTENNAS AND PROPAGATION, vol. AP-2, pp. 71–81; April, 1954.

[2] L. Brillouin, "Wave guides for slow waves," *J. Appl. Phys.*, vol. 19, pp. 1023–1041; November, 1948.

[3] D. K. Reynolds and W. S. Lucke, "Ridge and Corrugated Antenna Studies," Second Quart. Prog. Rep., Stanford Res. Inst., Menlo Park, Calif., Project No. 199; January, 1950.

[4] D. K. Reynolds and W. S. Lucke, "Corrugated end fire antennas," *Proc. Natl. Electronics Conf.*, vol. 6, pp. 16–28; September, 1950.

[5] W. Rotman, "A study of single-surface corrugated guides," PROC. IRE, vol. 39, pp. 952–959; August, 1951.

[6] A. L. Cullen, "The excitation of plane surface waves," IEE Monograph 93 R, vol. 101, part 4, pp. 225–234; February, 1954.

[7] R. A. Hurd, "The propagation of an electromagnetic wave along an infinite corrugated surface," *Can. J. Phys.*, vol. 32, pp. 727–734; December, 1954.

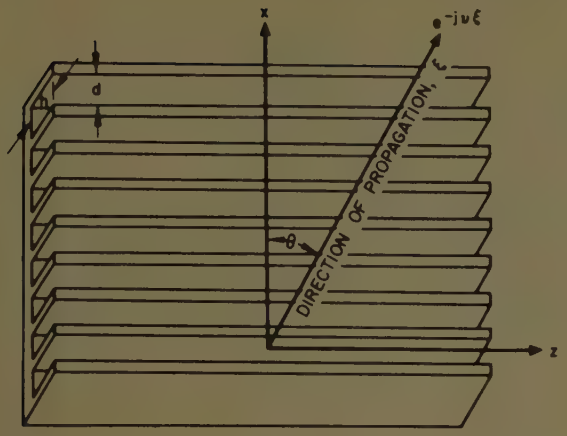

Fig. 1—Oblique propagation over a corrugated surface.

as the direction of propagation is varied from normal to the corrugations ($\theta = 0$ degrees) to the parallel direction ($\theta = 90$ degrees), the free space velocity to surface wave velocity ratio decreases to the plane wave value of unity. Fig. 2 depicts the propagation constant ratio or velocity ratio as a function of angle θ for two depths of teeth and for gap widths d/λ of 0.10 and the limit value zero. For the low values (near unity) required for most practical end fire antennas, the velocity ratio changes slowly with angle as seen in the curves of Fig. 2. The limit curves for h/λ equaling the cutoff value at $\theta = 0$ degrees are also shown. Recent independent work by Kay has considered the efficiency of skew surface-wave excitation.[8]

Experimental Results

Some experimental verification of the theory was attempted by making actual measurements of the wave velocity over a corrugated surface. The surface wave was excited using a linear waveguide slot array which operated at X-band frequencies. The corrugated surface which supported the surface wave has as its geometry $d/\lambda = 0.0953$ and $h/\lambda = 0.0648$ where d and h are the gap width and tooth depth, respectively. The wavelength of the surface-supported wave was measured for scan angles of from 0 to 30 degrees (in 5-degree increments). Values of c/v calculated from these data are plotted with the corresponding theoretical values in Fig. 3.

Since the wave velocity ratio does change slowly and continuously for values of c/v near unity as the wave propagation direction changes, it was desirable to determine what effect the scanning of a practical corrugated surface antenna had on the radiation patterns. To this end a corrugated surface was constructed with a design very similar to that of an existing search radar antenna which, however, cannot be scanned. Both antennas were constructed to give approximately a cosecant squared elevation pattern. The experimental surface was fed by a linear waveguide slot array (Fig. 4) designed for beamwidth of 9 degrees and 25-db sidelobes, and scanned by insertion of spacers in the snake. The azimuth patterns for this antenna are shown in Fig. 5 for scan angles of 0, 8, 15, and 25 degrees, and it is apparent that the main beam remains unchanged as the surface is scanned. Sidelobes are below the recorder threshold. The secondary beam which appears for larger scan angles is a result of slot spacing of the exciting source and, of course, is not a consequence of scanning over the corrugated surface.

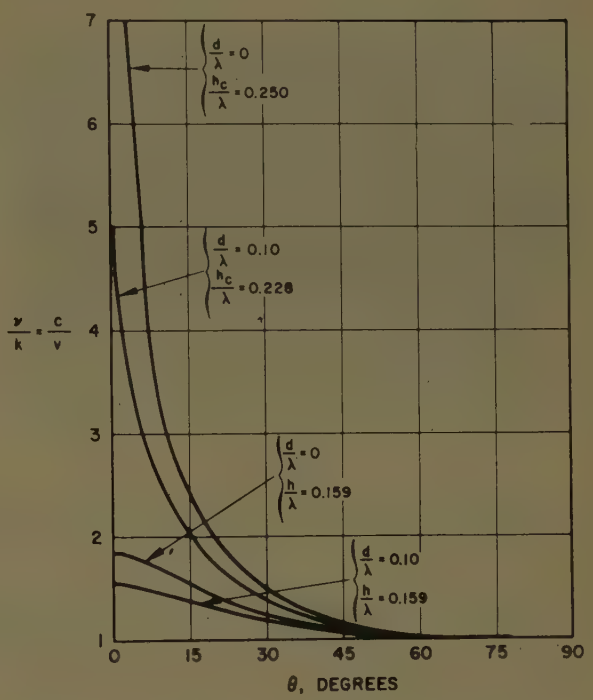

Fig. 2—Velocity ratio vs scan angle: limiting cases.

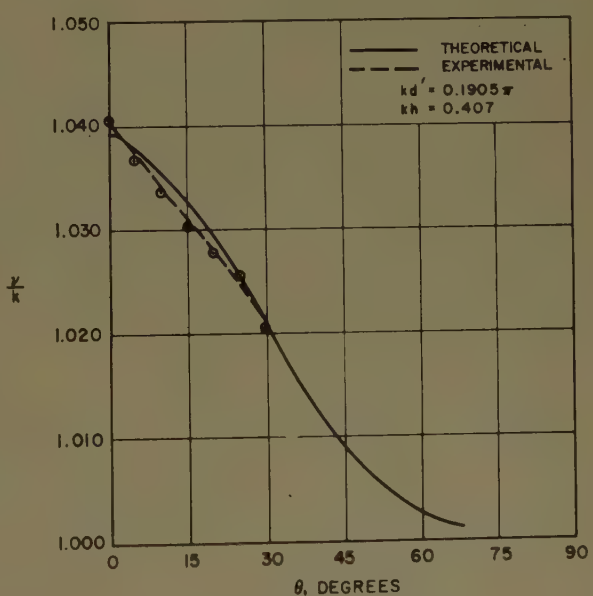

Fig. 3—Experimental velocity ratios.

[8] A. F. Kay, "Excitation Efficiency of Surface Waves Over Corrugated Metal and Doubly Corrugated Metal and in Dielectric Slabs on a Ground Plane," Sci. Rep. No. 5, Tech. Res. Group, New York, N. Y.; December, 1956.

Fig. 4—Prototype corrugated scanner antenna.

Of greater interest, however, are the elevation patterns of this antenna (Fig. 6). The shape of beam is not greatly changed as the antenna is scanned, and although no exhaustive effort was made to obtain an exact cosecant squared beam, the elevation patterns remain within plus or minus 3 db of cosecant squared from 10 to 80 degrees.

For the experimental antenna, it was convenient to mount the snake feed waveguide slot array in a plane perpendicular to the plane of the corrugated surface, as shown in Fig. 4. However, the snake feed array or other feeding device may be placed parallel to and just under the corrugated surface with a small splash plate conveying the energy up to and over the edge of the corrugated surface. Such an antenna could be constructed with a low silhouette, as indicated by the laboratory model shown in the photograph of Fig. 7. Patterns of this antenna were taken and found to be substantially the same as those of the previous model.

Theoretical Analysis

The method employed is that used by Hurd[7] on propagation normally across a corrugated surface, and includes 1) writing the complete fields both above the corrugations and in the gaps, 2) matching the tangential field components at the boundaries, and 3) using a calculus of residues technique to evaluate the resulting infinite set of simultaneous equations. To facilitate the solving of this problem, an idealized physical structure is assumed on which the corrugations or teeth are vanishingly thin. Another important assumption is that all modes but the dominant mode in the slot region are attenuated to negligible amplitude in traveling down the slot to the ground plane and back to the mouth of the slot. The conditions for this assumption to be good will be given later. The approach outlined above is not cognizant of finite tooth thickness, which is a second order effect, but does account for the tooth spacing which has an appreciable effect on the propagation constant.

The physical structure is shown in Fig. 8. A conducting plane of infinite length and width forms the base

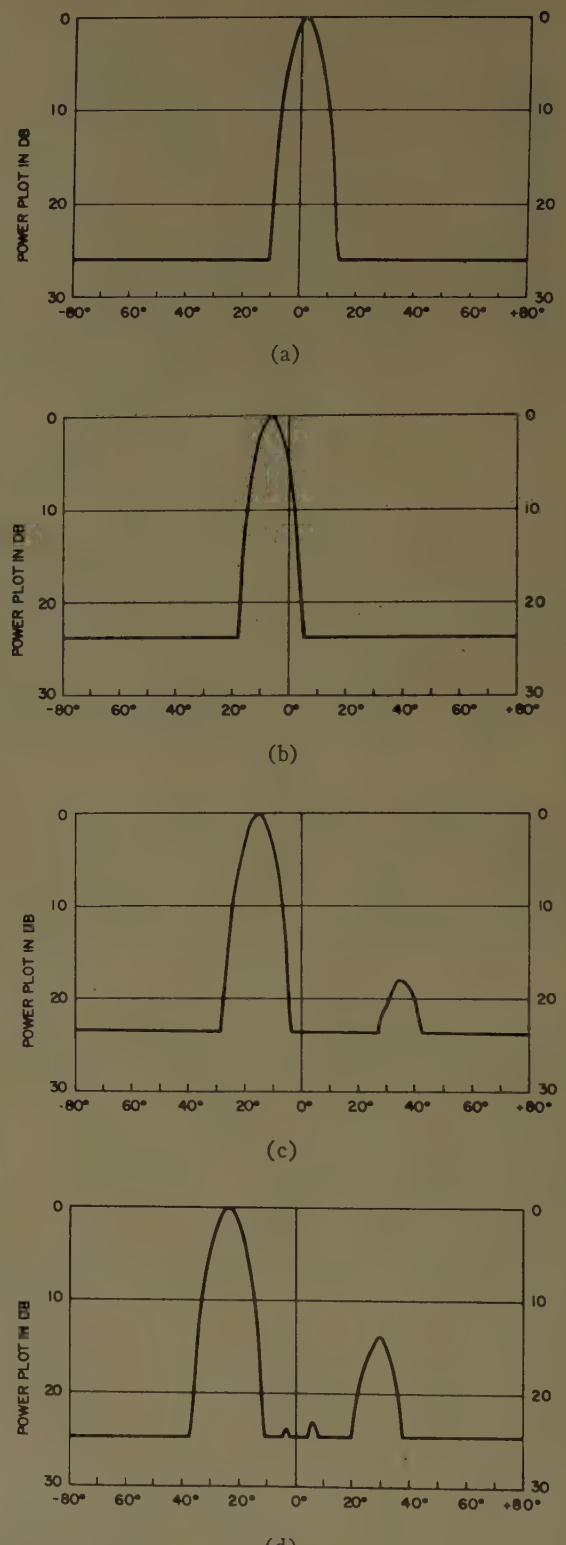

Fig. 5—Azimuth patterns of corrugated scanner antenna. (a) Scan angle = 0 degrees. (b) Scan angle = 8 degrees. (c) Scan angle = 15 degrees. (d) Scan angle = 25 degrees.

for an infinite number of vanishingly thin, evenly spaced parallel metal vanes. The vanes are of height h and separated by a distance d. The origin of coordinates is at the top of a vane with the z axis lying along the

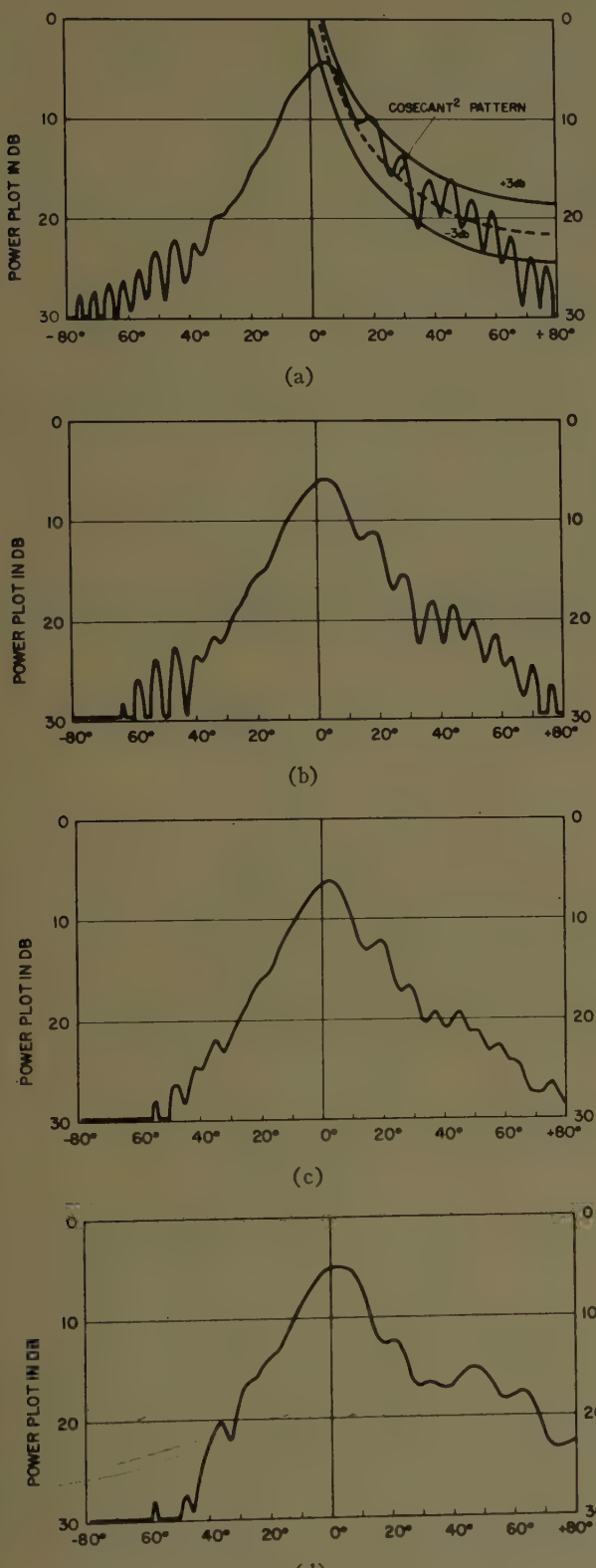

Fig. 6—Elevation patterns of corrugated scanner antenna. (a) $\theta=0$ degrees. (b) $\theta=8$ degrees. (c) $\theta=15$ degrees. (d) $\theta=25$ degrees.

vane and parallel to the ground plane. Fields produced by a source of finite dimensions will not be considered; only the surface wave mode on an infinite structure is assumed.

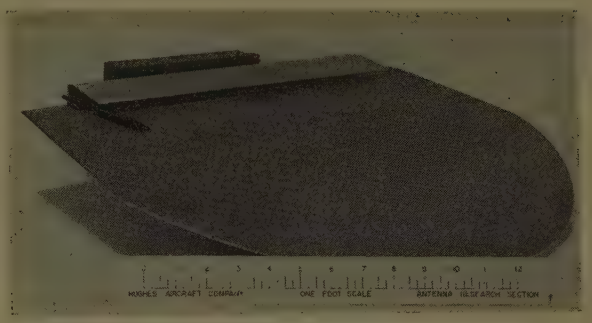

Fig. 7—Low silhouette corrugated scanner antenna.

Fig. 8—Infinite corrugated plane surface.

The allowable electromagnetic field above the corrugations is characterized by the absence of an E_z component, and thus the field can be expressed as

$$E = \text{curl } a_z f \qquad H = \frac{-1}{j\omega\mu} \text{curl curl } a_z f \tag{1}$$

where f is a solution of the scalar wave equation and a_z denotes a z-directed unit vector.

To obtain the correct solution of the scalar wave equation for the region above the corrugations, the desired wave structure is examined. The fields are to be attenuated for increasing y, since only surface waves are to be considered. Due to the nonuniform surface structure in x, higher order surface modes will appear in this direction; however, along the z axis a field variation with but a single propagation constant is valid, since at the $y=0$ plane the fields must match for all z. A time dependence of $e^{j\omega t}$ and loss free media throughout is assumed.

The solution of the scalar wave equation which satisfies these conditions is

$$f_n = A_n \exp(-j\beta_n x - j\tau z - \alpha_n y) \tag{2}$$

where β_n, τ, and α_n are related to the free space propagation constant by

$$k^2 = \beta_n^2 + \tau^2 - \alpha_n^2. \tag{3}$$

Since Floquet's Theorem applies to the periodic parallel-plate configuration in x the propagation constant in that direction must take the form

$$\beta_n = \beta_0 + 2n\pi/d \qquad (n = 0, \pm 1, \pm 2, \cdots) \tag{4}$$

where β_0, which defines the fundamental mode, must be determined by the corrugation geometry. Thus it is seen that for the dominant mode, the direction of propagation is given (see Fig. 1) by

$$\theta = \tan^{-1}(\tau/\beta_0) \tag{5}$$

where θ is measured from the x axis. The free space to surface wave velocity ratio for this mode is therefore

$$\frac{v_0}{v_s} = \sqrt{\frac{\beta_0^2 + \tau^2}{k^2}} = \frac{\nu}{k} . \tag{6}$$

The required solution of the scalar wave equation for the region between the corrugations is readily determined from the boundary conditions imposed upon the field components at the bottom and sides of the gaps. Thus

$$f_m = B_m \cos \frac{m\pi}{d} x[\cos \gamma_m(y + h)]e^{-j\tau z} \tag{7}$$

where

$$k^2 = \left(\frac{m\pi}{d}\right)^2 + \tau^2 + \gamma_m{}^2 \qquad (m = 0, 1, 2, \cdots). \tag{8}$$

Equating tangential electric and magnetic components of the field at the plane $y=0$, three infinite sets of simultaneous equations result, of which only two sets are independent. The orthogonality properties of the trigonometric functions allow these to be reduced to the form[7]

$$\frac{d}{2} \frac{\epsilon_m \gamma_m B_m \sin \gamma_m h}{(-1)^m \exp(-j\beta_0 d) - 1} = \sum_{n=-\infty}^{\infty} \frac{-j\alpha_n \beta_n A_n}{\alpha_n{}^2 + \gamma_m{}^2} \tag{9a}$$

and

$$\frac{d}{2} \frac{\epsilon_m B_m \cos \gamma_m h}{(-1)^m \exp(-j\beta_0 d) - 1} = \sum_{n=-\infty}^{\infty} \frac{-j\beta_n A_n}{\alpha_n{}^2 + \gamma_m{}^2} \tag{9b}$$

where the Neumann number is

$$\epsilon_m = \begin{cases} 2, & m = 0 \\ 1, & m > 0 \end{cases} .$$

Multiplying (9b) by $j\gamma_m$ and then adding and subtracting (9a), there results, after some simplification,

$$\frac{-d}{2} \frac{\epsilon_m \gamma_m B_m e^{-j\gamma_m h}}{(-1)^m \exp(-j\beta_0 d) - 1} = \sum_{n=-\infty}^{\infty} \frac{\beta_n A_m}{\alpha_n - j\gamma_m} \tag{10}$$

and

$$\frac{d}{2} \frac{\epsilon_m \gamma_m B_m e^{j\gamma_m h}}{(-1)^m \exp(-j\beta_0 d) - 1} = \sum_{n=-\infty}^{\infty} \frac{\beta_n A_n}{\alpha_n + j\gamma_m} . \tag{11}$$

If $d<\lambda/2$, then all modes except $m=0$ are evanescent. Furthermore, since in a practical system $h>d$, the factor $\exp(-j\gamma_m h)$ in (10) becomes negligible even for $m=1$. Thus, neglecting the left-hand side of that equation when $m>0$,

$$-\delta_{0m} \frac{\gamma_0 d B e^{-j\gamma_0 h}}{\exp(-j\beta_0 d) - 1} = \sum_{n=-\infty}^{\infty} \frac{\beta_n A_n}{\alpha_n - j\gamma_m} \tag{12}$$

where δ_{0m} is the Kronecker Delta symbol.

From the two infinite sets of simultaneous equations (11) and (12) must be found the amplitude coefficients A_n and B_m and the wave number B_0, the latter yielding directly the propagation constant ν.

These equations may be solved using a calculus of residues technique[9] which enables one to write the right-hand side of (11) and (12) as the sum of the residues of a function $f(w)$. This function $f(w)$ is defined as

1) having simple poles at $w=\alpha_n(n=0, \pm 1, \pm 2, \cdots)$,
2) having simple zeroes at $w=j\gamma_m(m=1, 2, 3, \cdots)$,
3) tending to zero as $|w| \to \infty$ except at $w=\alpha_n$.

By choosing as the path of integration contours of increasingly large radius which avoid the poles $w=\alpha_n$ and enclose $w=j\gamma_0$

$$\frac{1}{2\pi j} \int_C \frac{f(w)dw}{w - j\gamma_m} = \sum_{n=-\infty}^{\infty} \frac{R(\alpha_n)}{\alpha_n - j\gamma_m} + \delta_{0m} f(j\gamma_0) = 0 \tag{13}$$

where $R(\alpha_n)$ is the residue of $f(w)$ at $w=\alpha_n$. Comparing this equation with (12), the coefficients are obtained in terms of the function:

$$f(j\gamma_0) = -\frac{\gamma_0 d B_0 e^{-j\gamma_0 h}}{e^{-j\beta_0 d} - 1} \tag{14}$$

and

$$A_n = \frac{R(\alpha_n)}{\beta_n} . \tag{15}$$

With the same definition for $f(w)$

$$\frac{1}{2\pi j} \int_C \frac{f(w)dw}{w + j\gamma_m} = \sum_{n=-\infty}^{\infty} \frac{R(\alpha_n)}{\alpha_n + j\gamma_m} + f(-j\gamma_m) = 0. \tag{16}$$

When this equation is compared with (11), the same formula results for A_n, but also

$$f(-j\gamma_m) = \frac{d}{2} \frac{\epsilon_m \gamma_m B_m e^{j\gamma_m h}}{(-1)^m e^{-j\beta_0 d} - 1} . \tag{17}$$

Now if $f(w)$ were known, the mode amplitudes could be found from (15) and (17).

It is essential that the function has the prescribed poles and zeroes, and must satisfy (14). In addition to conditions 1), 2), and 3), the function $f(w)$ must also satisfy the edge criterion which requires that the field at the edge of each corrugation be singular in the allowable fashion,[10] as $r^{-1/2}$. Thus it can be shown[11] that the unique expression for $f(w)$ is

[9] R. C. Hansen, "Single slab arbitrary polarization surface wave structure," IRE TRANS. ON MICROWAVE THEORY AND TECHNIQUES, vol. MTT-5, pp. 115–120; April, 1957.

[10] C. J. Bouwkamp, "Diffraction theory," *Reps. Prog. Phys.*, vol. 17, pp. 35–100; May, 1954.

[11] R. C. Hansen, "Single Slab Circular Polarization Surface Wave Structure," Sci. Rep. No. 9, Hughes Aircraft Co., Culver City, Calif.; February, 1956.

$$f(w) = \frac{-\gamma_0 d B_0 \exp(-j\gamma_0 h) \exp \frac{d \ln 2}{\pi} (j\gamma_0 - w)(j\gamma_0 - \alpha_0)\Pi_1(w)\Pi_2(j\gamma_0)}{[\exp(-j\beta_0 d) - 1](w - \alpha_0)\Pi_1(j\gamma_0)\Pi_2(w)} \tag{18}$$

where

$$\Pi_1(w) = \prod_{p=1}^{\infty} (w - j\gamma_p)\left(-\frac{d}{p\pi}\right)\exp\left(\frac{dw}{p\pi}\right) \tag{19}$$

$$\Pi_2(w) = \prod_{p=1}^{\infty} (w - \alpha_p)(w - \alpha_{-p})\left(\frac{d}{2p\pi}\right)^2 \exp\left(\frac{dw}{p\pi}\right). \tag{20}$$

In these infinite products the exponential terms are necessary to produce convergence.

The combination of (14) and (17) for $m=0$ yields the formula

$$f(j\gamma_0) = -f(-j\gamma_0)\exp(-2j\gamma_0 h) \tag{21}$$

from which the phase constant for the dominant mode may be evaluated. Since (21) must be satisfied in argument as well as modulus,

$$\cos^{-1}\frac{\gamma_0}{\beta_0} + \sum_{p=1}^{\infty}\left\{\sin^{-1}\frac{\gamma_0 d}{pn} - \sin^{-1}\frac{\gamma_0}{\beta_p} - \sin^{-1}\frac{\gamma_0}{|\beta_{-p}|}\right\} + \frac{\gamma_0 d \ln 2}{\pi} = \gamma_0 h. \tag{22}$$

The inverse sines in the summations may be approximated by their arguments, and so after some simplification the following expression is obtained which relates the propagation constant ν to the scan angle θ (since $\nu^2 = k^2 + \beta_0^2 - \gamma_0^2$) and to the physical dimensions d and h.

$$\gamma_0 h = \cos^{-1}\frac{\gamma_0}{\beta_0} + \frac{\gamma_0 d}{2\pi}\left[2\psi\left(1 + \frac{\beta_0 d}{2\pi}\right) + \pi\left(\cot\frac{\beta_0 d}{2} - \frac{2}{\beta_0 d}\right) + 2(c + \ln 2)\right]. \tag{23}$$

ψ denotes the digamma function,[12] and c is Euler's constant.

If the gap width d approaches zero, (23) reduces to

$$\cos\gamma_0 h = \gamma_0/\beta_0$$

which is just that obtained by assuming only a single (lowest) mode in each region, and then equating these fields.

[12] A. Erdelyi, *et al.*, "Higher Transcendental Functions, Vol. I," McGraw-Hill Book Co., Inc., New York, N. Y., p. 15; 1953.

Differentiation of (22) with respect to β_0 shows that the maximum allowable value of $\beta_0 d$ is π. When this value is substituted into (23), the cut-off value of the tooth depth h_c is obtained:

$$h_c = \frac{\pi}{2\gamma_0} - \frac{d}{\pi}\ln 2 - \text{Order}(\gamma_0^2 d^3). \tag{24}$$

Thus h_c is a function of the wave propagation direction, For propagation normal to the corrugations, the cut-off depth is exactly that given by Hurd,[7] but as the propagation angle moves from the normal position, h_c increases if d remains fixed.

For propagation across a surface which has constant values for the tooth depth and spacing, there is no cut-off angle for surface wave propagation. This is illustrated in Fig. 2, where ν/k vs θ is plotted for $d/\lambda = 0.1$ and for $d/\lambda = 0$. The upper curves for $h/\lambda = h_c/\lambda$ (at $\theta = 0$ degrees) gives the maximum values for ν/k which can be obtained with the given tooth and gap dimensions. Any h/λ less than this limit value gives a correspondingly lower wave velocity ratio as indicated by the curves for $h/\lambda = 0.159$.

The normalized attenuation factor α_0/k is plotted against the scan angle in Fig. 9. As is to be expected from the variation of ν/k with θ, the attenuation of the "trapped" wave also decreases as the direction of propagation moves from the normal ($\theta = 0$ degrees). Thus as the free space to surface wave velocity ratio decreases, a smaller percentage of the power in the surface wave is concentrated close to the corrugated surface.

The mode amplitudes can be found from (15) and (18) and an approximate solution of these equations gives

$$\left|\frac{A_n}{B_0}\right| \cong \frac{\gamma_0 d(\alpha_n + \alpha_0)(\alpha_n + \alpha_1)(\alpha_n + \alpha_{-1})\Gamma\left(2 + \frac{\alpha_n d}{\pi}\right)\exp\left(-\frac{\alpha_n d \ln 2}{\pi}\right)}{8\pi\alpha_n |\beta_n| (\alpha_n + j\gamma_1)\Gamma\left[2 + \frac{d(\alpha_n + \beta_0)}{2\pi}\right]\Gamma\left[2 + \frac{d(\alpha_n - \beta_0)}{2\pi}\right]}. \tag{25}$$

Two ratios of particular interest have been computed and plotted (Fig. 10) for a specific corrugation geometry. These are $\beta_1/\beta_0|A_1/A_0|$, the ratio of first higher order mode to dominant mode above the corrugations, and $|A_0/B_0|$, the ratio of the dominant mode above to the dominant mode in the corrugations. At $\theta = 90$ degrees the corrugations have no effect on the dominant mode which becomes a plane wave propagating with

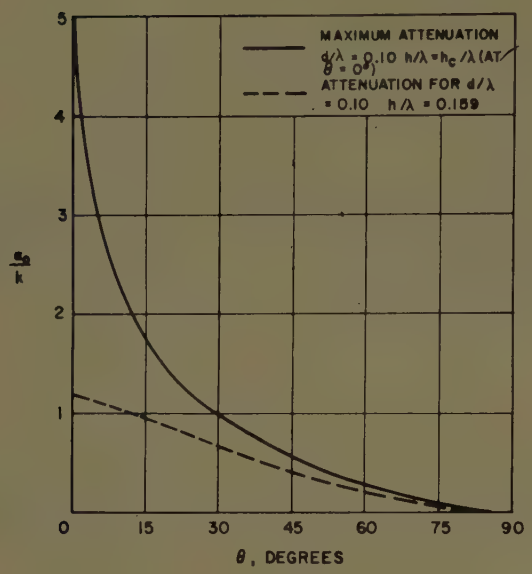

Fig. 9—Transverse attenuation constant vs scan angle.

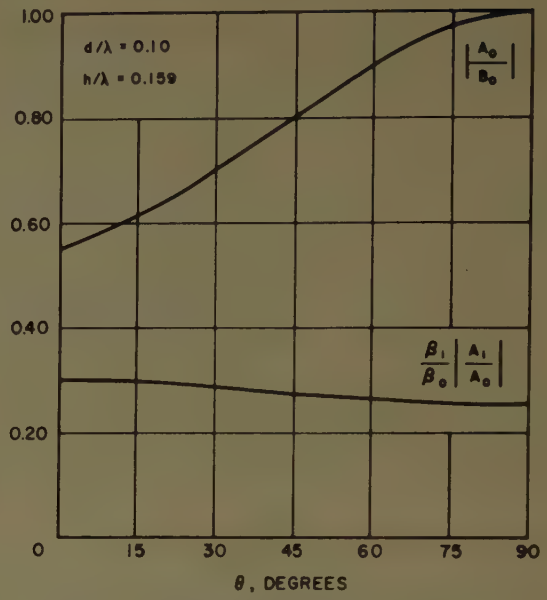

Fig. 10—Amplitude ratios vs scan angle.

the velocity of light in the z direction. The higher order modes, however, are highly attenuated in y, and their amplitudes are small compared to the amplitudes of the dominant mode.

Conclusions

Theory has predicted that a surface wave can propagate across a corrugated surface at an oblique angle, and that the wave velocity increases smoothly to the free space value as the wave direction approaches that parallel to the corrugations. Experiments have shown that a corrugated surface antenna may be scanned through an appreciable angle, at least ± 30 degrees, with the surface maintaining control over the elevation pattern. Thus an additional degree of flexibility has been added to the corrugated surface antenna.

communications

Measurements of the Bandwidth of Radio Waves Propagated by the Troposphere Beyond the Horizon*

J. H. CHISHOLM†, L. P. RAINVILLE†, J. F. ROCHE†, AND H. G. ROOT†

THERE is general agreement that radio waves received well beyond the horizon are propagated by a tropospheric mechanism which produces in effect a multiplicity of equivalent plane wave components arriving simultaneously at the receiving antenna with random phase relationships and angular directions which vary rapidly in time. The description of the communications capacity of this propagation mechanism has been referred to as "bandwidth" which has an explicit meaning to communications engineers for circuit applications based upon parameters of resistance, capacitance, and inductance which do not vary in time. If the troposphere could be "frozen," an instantaneous transmission response could be obtained by transmitting an infinitely narrow impulse and using an infinitely wide bandwidth receiver or tuning a CW transmitter over the spectrum of frequencies of interest and receiving the signal with a narrow band receiver. In order to approximate the latter technique in the case of the actual troposphere, a series of consecutive frequency sweeps over a finite band of frequencies with a period which is small in terms of the fading periods should show the near instantaneous successive transfer function $H(\omega)$ of the mechanism.

We are presenting a brief summary of experiments designed to investigate the transmission characteristics as a function of time and frequency using a frequency modulated 2290-mc klystron transmitter and a wideband traveling-wave tube receiver over the 188-mile path between Round Hill, Mass. and Crawfords Hill, N. J. The transmitter frequency was swept over a 20-mc band at a rate of 100 cps and the results were recorded with a 16-mm movie camera at a rate of 24 frames per second. A sample sequence of motion pictures, shown in Fig. 1, summarizes the results of these experiments. The amplitude appears to vary in a systematic manner. The variation of amplitude as a function of time and frequency is shown simultaneously in the form of a three-dimensional model, Fig. 2, constructed from 1500 frames of the aforementioned motion pictures and indicates variation of amplitude for a one-minute period over the range 2283–2297 mc.

Analyses of these data in both the time and the frequency domains were performed by comparing the spacing of the maxima in time and frequency obtained from experimental data with the spacing predicted with a given scattering model.[1] The results of the time analysis indicate a mean separation of 2.2 seconds compared to a separation of 0.5 second predicted theoretically. Conversely, the result of analysis of data in the frequency domain indicated a separation of maxima of 3 mc which was greater by a factor of about 2 than the separation of 1.7 mc predicted by theory. A more rigorous analysis in the frequency domain consisted of determining the correlation of amplitude as a function of spacing. The results of this analysis indicated a correla-

* Manuscript received by the PGAP, May 29, 1958. The research reported in this document was supported jointly by the Army, Navy, and Air Force under contract with the Massachusetts Institute of Technology.

† Lincoln Lab., Mass. Inst. Tech., Lexington, Mass.

[1] S. O. Rice, "Statistical fluctuations of radio field strength far beyond the horizon," PROC. IRE, vol. 41, pp. 274–281; February, 1953.

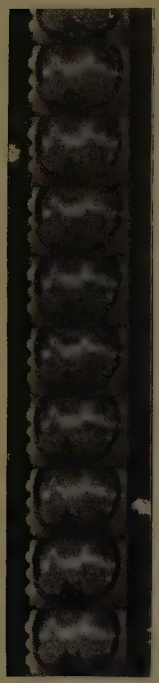

Fig. 1.

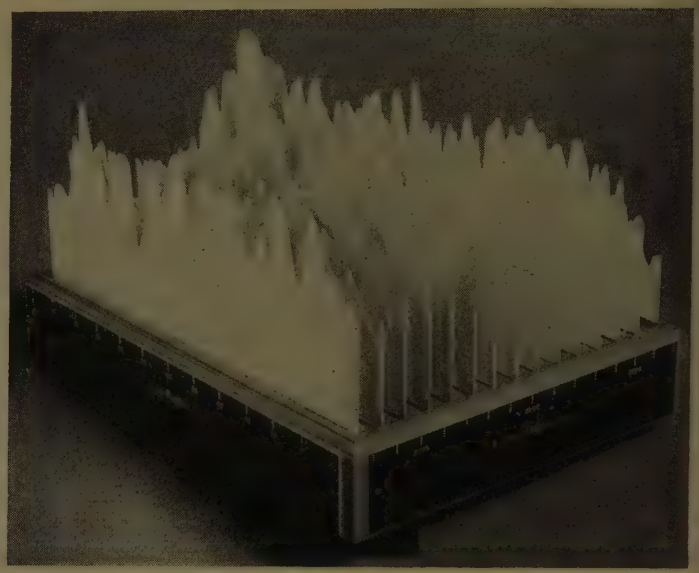

Fig. 2.

tion coefficient of 0.4 at 2 mc separation compared with a 0.02 correlation coefficient predicted theoretically.

Since it is not realistic to represent bandwidth as a simple figure when applied to tropospheric scatter transmissions, a statistical form is used. The maximum variations of amplitude within frequency increments of 1.0 to 10 mc were determined and the distributions compiled (Fig. 3).

The results of the analyses in the time and frequency domains are consistent and both suggest that the multipath delays are less than predicted by the scattering model used by Rice in his theoretical paper.

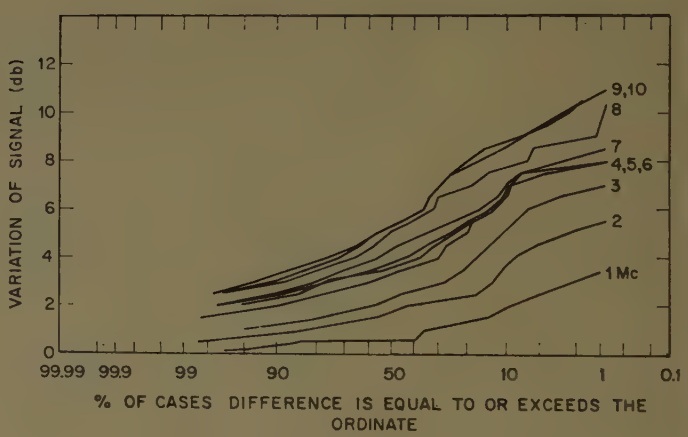

Fig. 3—Distribution of maximum variation of signal.

Remarks on the Fading of Scattered Radio Waves*

RICHARD A. SILVERMAN†

IN a previous paper,[1] hereinafter designated as A, an expression was derived for the envelope fading rate of radio waves scattered by dielectric turbulence, under the tacit assumption that the scattering volume V is effectively at infinity as seen by the transmitter and receiver, *i.e.*, that V is accurately characterized by a single scattering angle. Since this condition is rarely met in practice, the fading rate formula derived in A has only limited applicability. The purpose of this note is to extend the treatment of A by including the additional contributions to fading which result when there is appreciable scattering angle variation within V, as well as when there is appreciable shear of the mean wind within V.

As in A, we begin by dividing V into a large number N of cubical subvolumes $V_1, \cdots V_N$, each of side d. We denote the center of each V_n by P_n, and we associate

* Manuscript received by the PGAP, June 19, 1958. The research reported in this paper has been sponsored by the Electronics Res. Directorate of the AF Cambridge Res. Ctr., Air Res. and Dev. Command, under Contract AF 19(604)3495.

† Inst. Math. Sci., New York University, New York 3, N. Y.

[1] R. A. Silverman, "Fading of radio waves scattered by dielectric turbulence," *J. Appl. Phys.*, vol. 28, pp. 506–511; April, 1957; errata, *ibid.*, p. 922; August, 1957. With a few exceptions, we adhere to the notation and terminology of this reference.

with every P_n its own scattering angle θ_n and scattering wave vector[2] K_n. In addition to assumptions 1–4 and 6 of A, we make the following two assumptions: 1) The scattering wave vectors associated with the different points of any subcube V_n differ from each other by so little that we can regard every point of V_n as having the same typical scattering wave vector, which we choose to be K_n; 2) The quantity d is such that $d \leq L_0$, the macro-eddy dimension, and $K_n d \gg 2\pi$ for $1 \leq n \leq N$. Then, if the incident radiation has angular frequency ω, by a standard approximation[3] the contribution to the total scattered current from the dielectric turbulence in V_n is given by the real part of

$$I_n(t) = Bk^2 \exp(-i\omega t) \exp(i\gamma_n)(g_n g_n'/d_n d_n') \cdot \int_{V_n} \exp[i(K_n \cdot r_n)] \Delta\epsilon(r_n, t) dr_n, \quad (1)$$

where the position vector r_n is referred to P_n as origin, and $\Delta\epsilon(r, t)$ is the random departure from its mean of the relative dielectric constant at the point (r, t). Here d_n is the distance from the transmitting antenna T to P_n, and g_n its gain in the direction TP_n; d_n' and g_n' are the corresponding quantities for the receiving antenna. As we shall see immediately, the values of the constants B and γ_n do not concern us here.

We now assume that[4]

$$\langle I_m(t) I_n^*(t') \rangle \sim 0, \text{ if } m \neq n \text{ and } |t - t'| \leq \tau_0, \quad (2)$$

where τ_0 is of the order of the correlation time of the received scattered current. To justify (2), we note that assumption 2 of the preceding paragraph implies that the "scattering eddies" are small compared to the cube size d. Thus, if as usually assumed, the fine structure of dielectric turbulence is such that the small eddies are substantially uncorrelated when separated by distances large compared to their size, and if in time τ_0 (the greatest time separation of interest) the dielectric noise is convected through a distance small compared to d, then (2) should be a good approximation.[5] Relying on the same kind of heuristics, we can establish the formula[1,3]

$$\left\langle \int_{V_n} \exp[i(K_n \cdot r_n)] \Delta\epsilon(r_n, t) dr_n \cdot \int_{V_n} \exp[-i(K_n \cdot r_n')] \Delta\epsilon(r_n', t') dr_n' \right\rangle \sim \langle (\Delta\epsilon)^2 \rangle L_0^3 \int_{-\infty}^{\infty} R_n(\varrho, \tau) \exp[i(K_n \cdot \varrho)] d\varrho = (2\pi)^3 \langle (\Delta\epsilon)^2 \rangle L_0^3 \Phi_n(K_n, \tau),$$

where $R_n(\varrho, \tau)$ is the space-time correlation function of the dielectric noise as measured in V_n (the variables ϱ and τ are defined by $\varrho = r - r'$, $\tau = t - t'$), and the quantity $\Phi_n(K_n, \tau)$ is the semitransform used in A. Finally, using (1)–(3), we find that the correlation function of the total scattered current $I(t) = \sum_{n=1}^{N} I_n(t)$ is given by

$$C(\tau) = \langle I(t) I^*(t') \rangle / \langle |I(t)|^2 \rangle = \sum_{n=1}^{N} E_n \exp(-i\omega\tau) \Phi_n(K_n, \tau) \Big/ \sum_{n=1}^{N} E_n \Phi_n(K_n, 0), \quad (4)$$

where $E_n = (g_n g_n'/d_n d_n')^2$.

To take into account the effect of convection, we recall (7) of A, to the effect that

$$\Phi_n(k, \tau) = \exp[i(k \cdot v_n)\tau] \Phi_\mu(k, \tau), \quad (5)$$

where $\Phi_\mu(k, \tau)$ is the semitransform of the dielectric noise as measured in a coordinate system which in each V_n moves with the velocity v_n that remains after velocity fluctuations on the scale of the smaller eddies (including the scattering eddies) have been smoothed out. (It is to be expected that this smoothing will have little effect on the *univariate* velocity distribution, which is approximately Gaussian.[6]) In A this moving coordinate system was called the "Lagrangian system," but since the small eddy components of the velocity field have been averaged out, the term is somewhat of a misnomer. The possibility of separating the self-motion of the smaller scattering eddies from their motion due to convection by the larger eddies of size d, at least in an approximate way, is essential to our approach, and seems intuitively reasonable; however, the legitimacy of this separation, which is also implicit in the work of Kolmogorov,[7] has recently been challenged.[8] We now substitute (5) in (4) and obtain

$$C(\tau) = \sum_{n=1}^{N} G_n \exp(-i\omega\tau) \exp[i(K_n \cdot v_n)\tau] \phi(K_n, \tau), \quad (6)$$

where $\phi(k, \tau) = \Phi_\mu(k, \tau)/\Phi_\mu(k, 0)$ is the *normalized* semitransform in the moving system. The weights G_n are defined by

$$G_n = E_n \Phi_\mu(K_n, 0) \Big/ \sum_{n=1}^{N} E_n \Phi_\mu(K_n, 0)$$

and sum to unity.

Since the wind v_n has a turbulent component, the quantity $C(\tau)$ is still random. Thus, if we center v_n about its mean value by writing $v_n = \overline{v_n} + v_n'$, it remains to

[2] Defined as k times the difference between the unit vector from the transmitter to P_n and a unit vector from P_n to the receiver, where k is the wave number of the incident radiation.

[3] See, *e.g.*, R. A. Silverman, "On Radio Scattering by Dielectric Turbulence," New York University, Inst. Math. Sci., Div. of Electromagnetic Res., New York, N. Y., Res. Rep. EM-98; September, 1956.

[4] The angular brackets denote the ensemble average, and the asterisk denotes the complex conjugate.

[5] These conditions seem to be met in practice, at least at the higher of the carrier frequencies used.

[6] G. K. Batchelor, "The Theory of Homogeneous Turbulence," Cambridge University Press, Cambridge, Eng., ch. 8; 1953. The effect of the small eddies on the bivariate velocity distribution is crucial, however (*ibid.*).

[7] A. N. Kolmogorov, "The local structure of turbulence in incompressible viscous fluid for very large Reynolds number," *C. R. (Doklady) Acad. Sci. URSS*, vol. 30, pp. 301–305; 1941.

[8] R. H. Kraichnan, "Irreversible statistical mechanics of incompressible hydromagnetic turbulence," *Phys. Rev.*, vol. 109, pp. 1407–1422; March, 1958; "The Structure of Isotropic Turbulence at Very High Reynolds Numbers," New York University, Inst. Math. Sci., Div. of Electromagnetic Research, New York, N. Y., Res. Rep. MH-9; February, 1958.

average $C(\tau)$ with respect to the random variables v_n', an operation we denote by an overbar. The possibility of doing this averaging independently of the averaging we have already done over realizations of the dielectric noise seen in the moving coordinate system rests on the reasonable assumption that the velocities of eddies of size d are substantially independent of the dielectric fluctuations of the smaller scattering eddies. Assuming that the turbulent velocity field is homogeneous, so that the random variables v_n' are identically distributed, we obtain

$$\overline{C(\tau)} = \sum_{n=1}^{N} G_n \exp(-i\omega\tau) \cdot \exp[i(\boldsymbol{K}_n \cdot \overline{\boldsymbol{v}_n})\tau]\phi(\boldsymbol{K}_n, \tau)\psi(\boldsymbol{K}_n, \tau). \quad (7)$$

The quantity $\psi(k, \tau)$ is defined by

$$\psi(k, \tau) = \overline{\exp[i(k \cdot v')\tau]} = \int_{-\infty}^{\infty} \exp[i(k \cdot v')\tau] p(v') dv', \quad (8)$$

where $p(v')$ is the probability density of the common distribution of the v_n'; $\psi(k, \tau)$, like $\phi(k, \tau)$, is a correlation function in τ for every k. As already remarked, $p(v')$ is effectively the univariate probability density of the turbulent velocity field, which is approximately Gaussian. Hence the correlation function $\psi(k, \tau)$ is real, and is in fact itself approximately a Gaussian function.

The calculation of the envelope fading rate from (7) proceeds in standard fashion. First, we note that since $I(t)$ contains only negative frequencies, the envelope of its real part is just $|I(t)|$. Next, we note that since $I(t)$ is approximately a Gaussian process, $|I(t)|$ is approximately a Rayleigh process.[1] It follows that the rate at which $|I(t)|$ crosses the level $\sigma\sqrt{\langle |I|^2 \rangle}$ is given by[9]

$$Z(\sigma) = 2\sqrt{Q/\pi}\sigma \exp(-\sigma^2), \qquad \sigma \geq 0.$$

[9] V. I. Bunimovich, "Amplitude peaks of random noise," *Zh. Tekh. Fiz.*, vol. 21, pp. 625–636; June, 1951.

The *fading parameter* Q is defined by

$$Q = -\ddot{R}(0) - [\dot{S}(0)]^2 = [-(d^2/d\tau^2)|\overline{C(\tau)}|]_{\tau=0}, \quad (9)$$

where $R(\tau)$ and $S(\tau)$ are the real and imaginary parts of $C(\tau)$, and the dot denotes differentiation with respect to τ. We see from (9) that any unimodular complex factor of $C(\tau)$ can be replaced by unity without changing the envelope fading rate. Thus, we are at liberty to set equal to unity the RF factor $\exp(-i\omega\tau)$ appearing in (7).

The remainder of the calculation is straightforward and consists in calculating the fading parameter Q from (7)–(9). The result is

$$Q = -\sum_{n=1}^{N} G_n \ddot{\phi}(\boldsymbol{K}_n, 0) + \sum_{n=1}^{N} G_n (\boldsymbol{K}_n \cdot \overline{\boldsymbol{v}_n})^2 - \left[\sum_{n=1}^{N} G_n (\boldsymbol{K}_n \cdot \overline{\boldsymbol{v}_n})\right]^2 + \sum_{n=1}^{N} G_n \overline{(\boldsymbol{K}_n \cdot \boldsymbol{v}_n')^2}. \quad (10)$$

It follows from (10) that the mean wind has an effect on the envelope fading rate only when different parts of the scattering volume are characterized by appreciably different scattering wave vectors or when there is appreciable shear in the mean wind within V. To see this, we note that the second and third terms of (10) cancel each other when we set $\boldsymbol{K}_n = \boldsymbol{K}_0$ and $\overline{\boldsymbol{v}_n} = \boldsymbol{v}_0$, $1 \leq n \leq N$. Thus these terms represent the effects of scattering angle variation and wind shear omitted in A, where it was assumed (rather unrealistically) that the effect of variation of $\boldsymbol{K}$ and $\bar{v}$ within V is unimportant. The first and last terms of (10), which were retained in A, represent the fading due to the random self-motion of the scattering eddies as seen in a coordinate system which effectively moves with the local wind velocity and the fading due to the convection of the scattering eddies by the mean wind and the macro-eddies. Finally, we note that for some purposes it may be convenient to approximate the sums in (10) by integrals over V, with terms which are the continuous analogs (defined in the obvious way) of G_n, $\boldsymbol{K}_n$ and $\overline{\boldsymbol{v}_n}$.

Phantom Radar Targets at Millimeter Radio Wavelengths*

C. W. TOLBERT†, A. W. STRAITON†, AND C. O. BRITT†

Summary—This paper describes the techniques and the measured radar return from "phantom targets" using 8.6 and 4.3-millimeter radars. The radar returns are compared to the measured back-scattering cross section of water drops, insects, steam and other materials at 8.6-mm wavelength as measured by a CW radar at this wavelength.

Within the limits of the conditions used in the laboratory, it was impossible to produce returns from synthesized refractive index gradients of sufficient magnitude to account for those noted on the radar. It is concluded, therefore, that for the millimeter wavelengths and the short ranges considered, the observed phantom returns were due to solid or liquid particles in the atmosphere.

* Manuscript received by the PGAP, February 21, 1958; revised manuscript received, June 16, 1958.

† Elec. Eng. Res. Lab., University of Texas, Austin, Texas.

Introduction

MANY observers have noted radar returns from phantom targets at frequencies throughout the radio spectrum. These observers have accumulated a large amount of data on the characteristics of the return from such targets and attempts have been made to simulate conditions hypothesized as responsible for the radar return.[1]

A recent and most complete resume of the data pertaining to the characteristics of these phantom radar returns over a wide range of frequencies has been made by Plank.[2] In this summation and in other reports, a large number of the returns have been attributed to refractive index gradients. The strength of the refractive index gradients and the size and shape of the atmospheric inhomogeneities which would produce these returns, which are called "angels," were considered by Plank. As a general rule, the measured returns are from one to two orders of magnitude greater than have been calculated for the angel models at short centimeter and millimeter wavelengths. The index gradients used in the angel models are based on maximum refractive index measurements as reported by Crain,[3] Cunningham[4] and others, and are assumed to exist over a sufficiently large area to give the effect of an infinite plane.

In order to obtain data on the simultaneous occurrence of phantom returns on 2-mm wavelengths, 8.6-mm and 4.3-mm radars were operated simultaneously. The sensitivity of the radars used was such that most of the observations were restricted to the first 1000 meters above the antenna. In addition, return from a rocket exhaust was measured.

To complement the radar return measurements, back-scattering cross sections of objects that might be airborne were measured with CW techniques.[5] The objects measured included insects, grass, water droplets, soap bubbles filled with helium, and water vapor jets or columns of steam and the fog produced with the atmosphere by cooling with dry ice and liquid nitrogen.

Instrumentation and Measuring Techniques of the Radar Observations

The 8.6-mm and the 4.3-mm radars are shown in Fig. 1. Bistatic antennas were used for transmitting and receiving at each frequency. The effective beamwidth was 1 degree for the 8.6-mm radar and 0.5 degree for the 4.3-mm radar. These antennas were pointed at a common volume. The sensitivity of the two radars was adjusted to produce the same deflection on an "A scope" per unit back-scatter cross section at each wavelength when the antennas were pointed at a point source. This permitted matching the sensitivity of the two systems in the direction of the main beam of the antenna patterns, but did not provide matching in other directions.

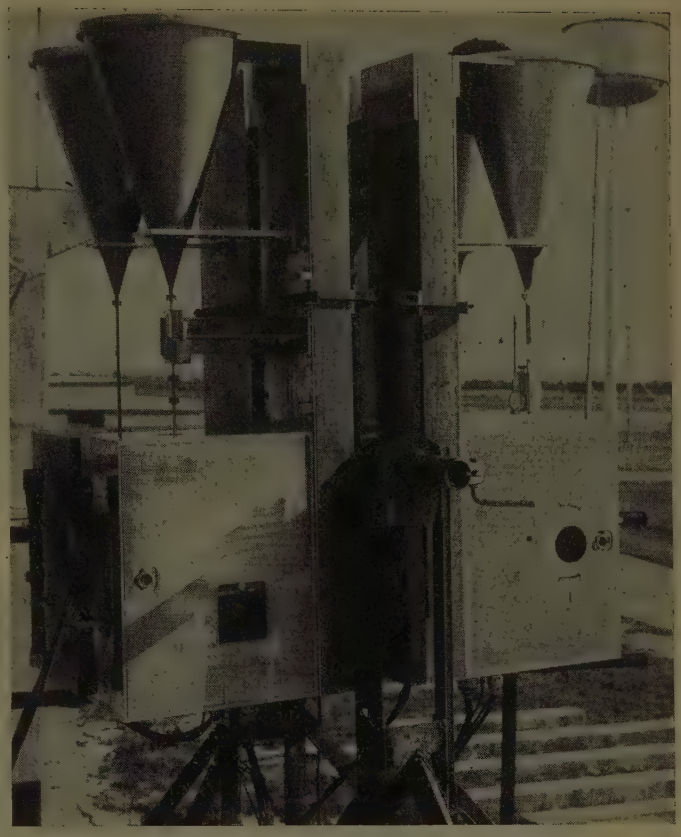

Fig. 1—View of millimeter radar.

Antennas with the same effective beamwidth would have been very desirable, but were not considered essential since the emphasis here is on the presence of phantom targets at the two wavelengths and on the measured back-scattering cross section of possible airborne reflectors and simulated refractive index gradients.

The pulse length of the radars was 0.15 microsecond and the recovery from the "main-bang" was effective within 250 feet of the antennas. The two radars were adjusted to "fire" alternately, with the return from the 4.3-mm system producing a positive return on the A scope and the 8.6-mm system producing a negative return on the A scope. The face of the A scope was photographed with a motion picture camera at 24 frames per second.

Measurements also were made of the back-scattering cross section of the exhaust from a simulated rocket motor burning a 6 to 5 ratio of zinc and sulfur as fuel. The stem or straight high velocity portion of the rocket exhaust filled the antenna pattern between the half-power points, and the plume or flared portion more than

[1] A. B. Crawford, "Radar reflections in the lower atmosphere," Proc. IRE, vol. 37, pp. 404–405; April, 1949.

[2] V. G. Plank, "A Meteorological Study of Radar Angels," Geophysics Res. Paper No. 52, Air Force Cambridge Res. Ctr., Cambridge, Mass.; July, 1956.

[3] J. R. Gerhardt, C. M. Crain, and H. Chapman, "Microwave refractive index fluctuations associated with convective activity in the atmosphere," *Bull. Amer. Meteorological Soc.*, vol. 37, pp. 251–262; June, 1956.

[4] R. M. Cunningham, V. G. Plank, and C. M. Campen, "Cloud refractive index studies," Geophysics Res. Paper No. 51, AFCRC-TR-56-210, ASTIA No. AD110259, Air Force Cambridge Res. Ctr., Cambridge, Mass.; October, 1956.

[5] C. W. Tolbert, *et al.*, "Back-scattering cross sections of water droplets, rain and foliage at 4.3 millimeter radio wavelengths," EERL Rep. No. 91, Univ. of Texas; April 30, 1957.

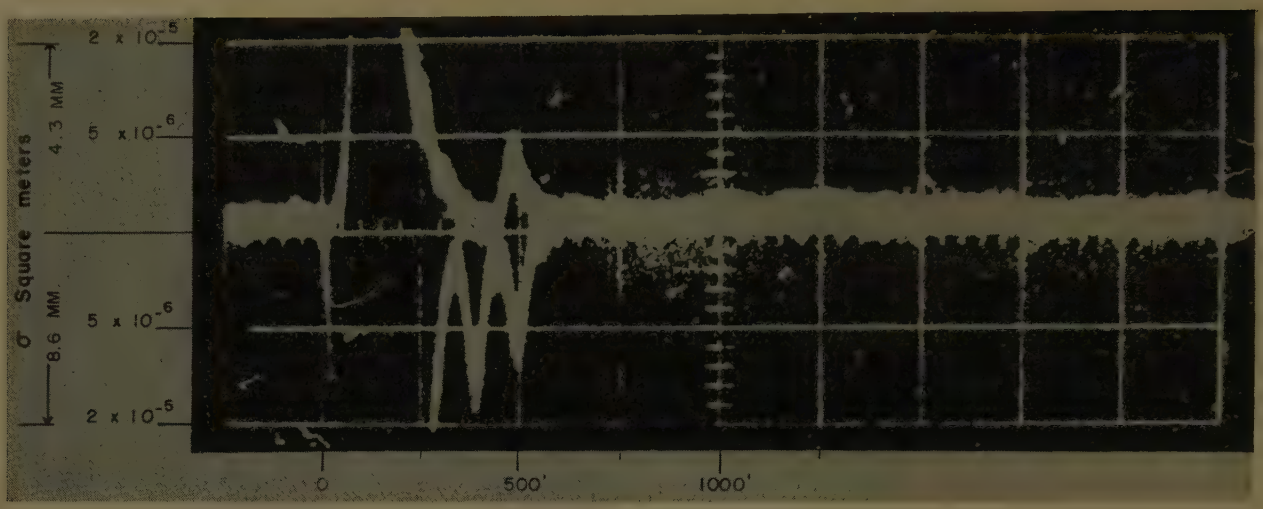

(a)

(b) (c) (d) (e) (f) (g)

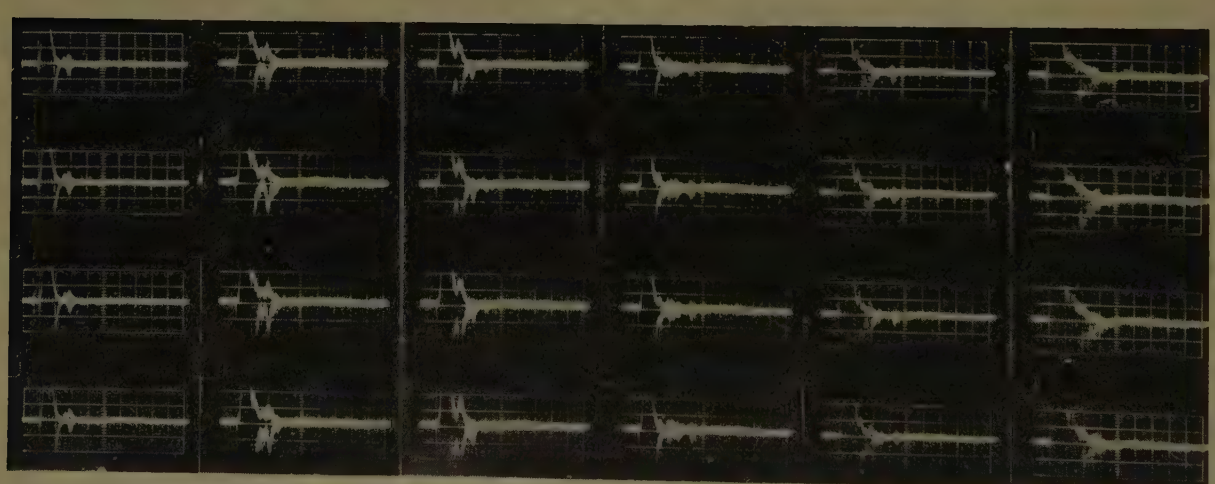

(h) (i) (j) (k) (l) (m)

Fig. 2—Samples of radar recordings on "A scope." (a) Photograph of A scope showing scales. (b) Negligible return on both wavelengths. (c) Single return from 750 feet noted on both wavelengths. (d) Returns from two elevations with 4.3-mm return suppressed. (e) Returns from two elevations with one 4.3-mm return suppressed. (f) Returns from two elevations with 8.6-mm return suppressed. (g) Multiple returns seen alternately on each wavelength. (h) Returns from two elevations with 8.6-mm return suppressed on one. (i) Multiple return noted on both wavelengths. (j) Multiple return from several elevations with some suppression on 4.3 mm. (k) Volume return centered at 500 feet with joint return to 800 feet. (l) Similar to (k) with 4.3-mm return suppressed. (m) Volume return following inverse square law.

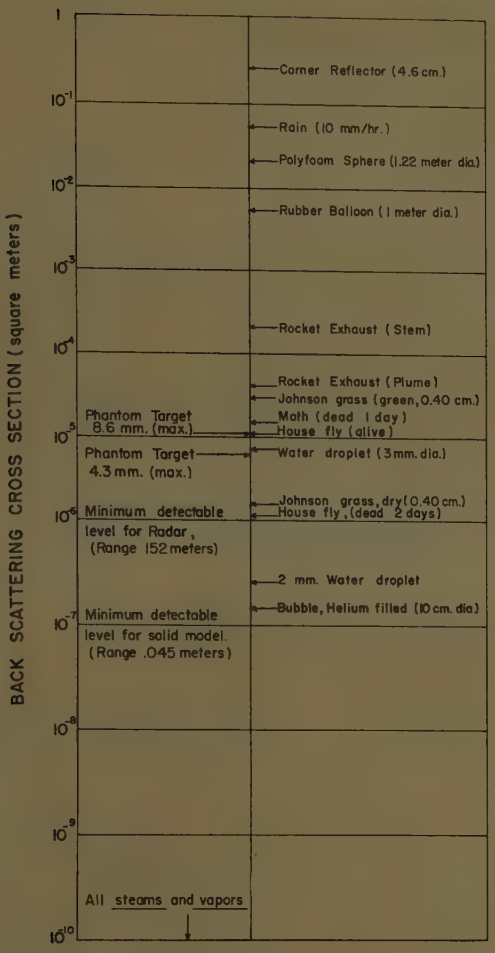

Fig. 3—Measured back-scatter characteristics at 8.6-mm wavelengths.

filled the pattern between the first nulls. The escaping gases and particles were semiopaque to light in both the stem and the plume during the period when radar returns were detected.

Results of the Radar Measurements

The simultaneous vertical soundings of the 8.6 and 4.3-mm radars were made on nine days in January, 1958. The days represented a variety of meteorological situations ranging from completely clear to heavily overcast. On no occasion did the radar fail to pick up a phantom return within a matter of a few seconds. However, there was considerable range in the frequency with which the returns occurred. Samples illustrative of some of the conditions observed on the radars are shown in Fig. 2(b) through 2(m). The horizontal scale shows altitude in increments of 250 feet. The returns measured are characteristic of those reported by other investigators with durations of up to several seconds, flutter characteristics of a coherent target, and occurrences at more than one range simultaneously. As would be expected from the antenna patterns, more 8.6-mm returns were noted than 4.3-mm returns.

In all, 3000 feet of film were taken, which will be analyzed in detail to obtain the statistical properties of the soundings. The analyses will be compared with the meteorological conditions under which they were made. This analysis is beyond the scope of this present work and will be presented in a later report. From these soundings, however, we may select the maximum return for comparison with the cross sections measured in the model range studies described in the next section. The scattering cross sections were calculated for the phantom returns and are included in Fig. 3.

In a similar manner, the scattering cross sections for the rocket exhausts were measured for the column falling within the antenna pattern, both for the stem and the plume and these results are also shown in Fig. 3.

In previous tests, this Laboratory has had occasion to measure the cross section of a 4.6-cm corner reflector, rain[5] as a function of rate, individual water drops as a function of size, and polyfoam spheres and rubber balloons which have been inflated with air. For the sake of comparison with the results of the present work, samples of these previous measurements have been added to Fig. 3.

Instrumentation and Measuring Techniques of the Model Studies

A continuous wave radar[5] operating at 8.6-mm wavelength was set up for laboratory measurements. The system had a minimum point back-scattering cross section detecting level of 10^{-7} square meters at a distance of 0.45 meter from the antenna. The 0.45-meter distance was in the Fraunhofer region for the antenna used.

Measurements were made of the back-scattering cross section of water droplets, insects, and grass. The objects were allowed to fall through and/or were suspended in the antenna pattern. The water droplets were produced with hypodermic needles. The size of the drops was controlled by varying the water pressure and needle size.[5]

A water droplet fog condensed from the air with dry ice and liquid nitrogen was allowed to pour down across the volume illuminated by the antenna. Soap bubbles were filled with helium, steam, and water vapor, and allowed to rise through the illuminated volume in front of the antenna. The distance from the antenna in these measurements was such that the minimum detectable reflectivity was 10^{-10} square meters. The reflected signals were recorded on a Brush recorder. The scattering cross sections calculated for each of the measurable cases are plotted in Fig. 3.

Summary of Cross-Section Measurements

The fog droplets produced by cooling of the air and the soap bubbles filled with water vapor and steam gave no measurable signals and therefore had a power reflection coefficient of less than 10^{-10}.

Single drops of water, 2 mm in diameter, produced a small but measurable return of 2.5×10^{-7} square meters, while a drop 3 mm in size produced a return of 7.5×10^{-6} square meters. It is noted that the 3-mm drop gives approximately the same return as a medium-sized house fly. In Fig. 4 this similarity has been used to compare the return measured for the water drop or house fly to returns calculated from assumed refractive index gradients in the atmosphere.

The steam presented the case of the sharpest artificial gas boundary with a difference across the surface of approximately 150 N units. It is difficult to imagine any index changes in the atmosphere except for solid or liquid particles with gradient as great as this. Since no return at the millimeter wavelength was measurable at the steam boundary, it is felt that it would be very difficult to get a return on millimeter radar from refractive gradients.

The various targets represented in Fig. 3 provide a comparison between reflectors ranging over six decades in scattering cross section, and thus provide a broad scale which helps to orient the cross section of the various materials considered.

Backscatter as a Function of Range

The potential return from a single millimeter water drop or a common house fly is plotted in Fig. 4 as a function of the range from 100 meters to 2000 meters. Two scales are used for the return indication; the one on the left is the ratio of the power transmitted to the power received, normalized to 100 meters, and the one on the right is the power reflectivity of a plane discontinuity which would produce the same return at the same range. This second scale also may be expressed in terms of the refractive index discontinuity which would be required to produce this return. The ordinates corresponding to ΔN of 6.3 and 20 are indicated. It is noted that a smaller index change would be required at a greater range since the assumption of an infinite plane reflector causes the power to decrease only as the square of the range, whereas the point reflector would have the power decrease as the fourth power of the range.

The use of this scale is not intended to imply that a large plane reflecting surface in the atmosphere is realistic. The extent of the flat plate for the reflections shown would need to increase with altitude and the

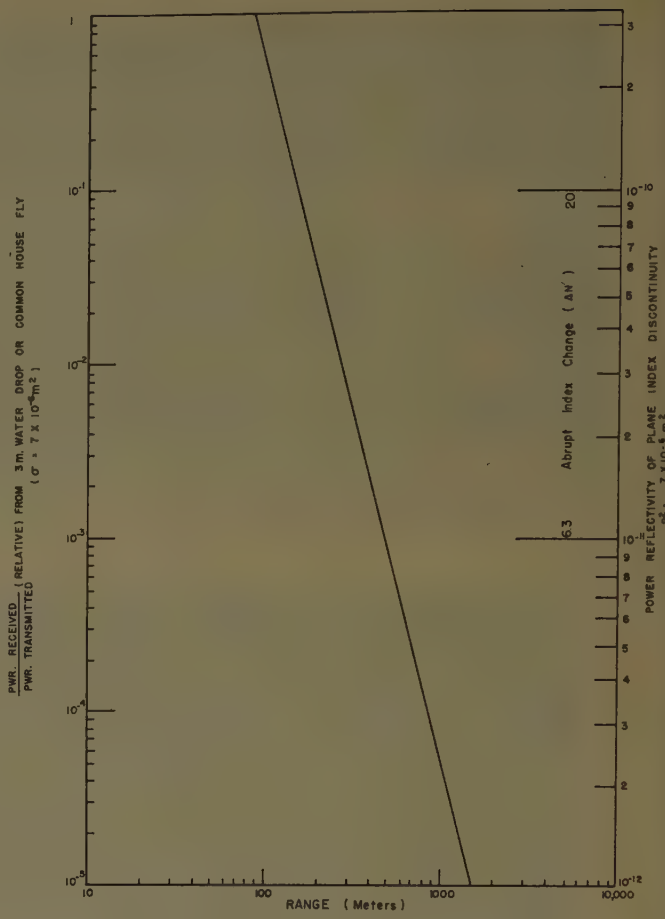

Fig. 4—Range back-scatter characteristics at 8.6-mm wavelengths.

deviations from flatness would need to be small compared to a wavelength. It would seem very unlikely that these conditions would be met in the atmosphere for millimeter wavelengths at least. The plane reflector does present, however, an upper limit to the power that might be returned from a single index gradient. For the short ranges, below approximately 1000 meters, single water drops or insects would seem to present much better targets than refractive index gradients. For much greater ranges and longer wavelengths, index gradients would seem to play a more significant role. Since many of the meteorological conditions under which longer wavelength returns have been noted are conducive to the formation of water drops, the possibility of this type of return should not be overlooked.

Telephone Remote Control Circuit for an Antenna Test Site*

L. YOUNG† AND G. M. WARD†

Summary—**A circuit is described which permits the remote control of several quantities, such as transmitter frequency, direction of polarization and RF match, at an unattended antenna tower. It requires only a single telephone line, which already exists for communication purposes at many test sites. Each quantity is controlled by a separate motor. The motors are controlled separately from the control end. This is achieved by adapting and installing a dialing circuit which allows, first, any desired motor to be "dialed"; next, to be controlled; and, finally, the line cleared so that another motor can be called.**

The parts for the dialing circuit were purchased at a total cost of about $150. Detailed circuit diagrams are given showing how the circuit is constructed.

Introduction

At many antenna test sites, the separation between the transmitting and receiving antennas is so great as to make the remote control of the system parameters (frequency, polarization, matching, etc.) at one of the locations desirable. No suitable remote control equipment seems to be available commercially, and none has been described for this specific application. A system built for an antenna test site at the Westinghouse Electronics Division is described in this communication.

At most sites, a telephone line is available between the two antenna towers for communication purposes. The usual procedure is to instruct a man making the adjustments at the remote antenna. By adapting and installing a dialing circuit connected to several relays controlling motors, the remote tower can be left unattended and the several system parameters can be adjusted independently over the one telephone line.

Frequency Remote Control

The most commonly required adjustment at the remote site has been changing the frequency of the signal generator. The first remote control circuit, therefore, merely used the two wires of the telephone line to drive a slow motor which was suitably geared down to tune the remote signal generator. The frequency was measured at the receiving antenna with the superheterodyne receiver by bracketing the transmitter frequency with the two local oscillator frequencies which peaked the signal. It was arranged so that the remotely controlled motor could be driven in either direction by pressing one of two buttons.

The success of this arrangement led to more ambitious plans. It was desired to adjust by remote control not only the frequency, but also the polarization, and a double stub tuner; the possibility of making other adjustments was also contemplated. A means had to be devised which allowed any one of several motors to be controlled remotely, still using only the one telephone line. This was achieved by adapting and installing a dialing circuit which allowed any desired motor to be first "dialed," and then controlled, and which finally cleared the line until another motor was called. Each motor makes one of the desired adjustments.

The parts for the dialing circuit can all be purchased (total cost from surplus suppliers amounted to about $150), and can readily be constructed.

Dialing and Control Circuit

The circuits at the two ends of the telephone line are shown in Figs. 1 and 2. Their operation will be described in three stages, according to the setting of the operations switch S1.

Operation A

The operations switch S1 shown in Fig. 1, the control end of the line, is set to position 1 ("dial"), thus connecting the contacts of relay K1 across the input end of the telephone line, at terminals T2 and T3. The dialing contacts are normally open; they close as soon as the dial is moved off normal, then open and close successively as the dial returns from the number dialed. In Fig. 2, which depicts the remote end of the line, the relay K2 is normally released as shown. When the number is dialed, relay K3 successively operates and releases, energizing and deenergizing the coil of stepping switch SS1 via the contacts of K3, thus moving the wipers of the two-bank ten-position stepping switch SS1 to the desired position. The contacts of one bank (B) are all tied together, except for the first contact, and connected to the slow-operate relay K2, which operates a fraction of a second after dialing has been completed. Its contacts prepare a new circuit arrangement described in operation B.

Operation B

The operations switch S1 (Fig. 1) is now set to position 2 ("operate"), connecting the telephone line terminals T2 and T3 across the momentary contact double-pole-double-throw key KS1, which is normally open, and which can connect the 48-volt dc power supply with either polarity across T2–T3. Since relay K2 in Fig. 2 is now operated, and the stepping switch SS1 is set on bank A to connect through to the selected relay

* Manuscript received by the PGAP, January 27, 1958; revised manuscript received, June 2, 1958.

† Westinghouse Electric Corp., Baltimore, Md.

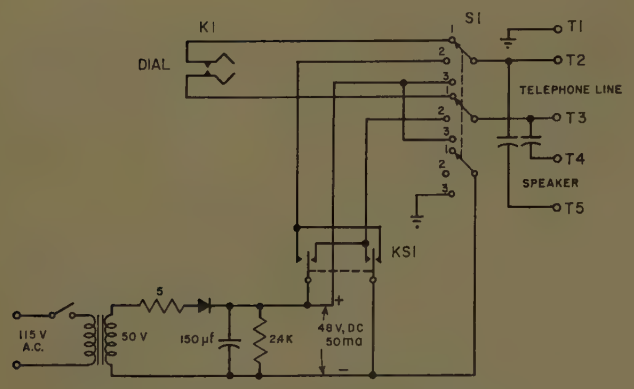

Fig. 1—Telephone remote control (control end).

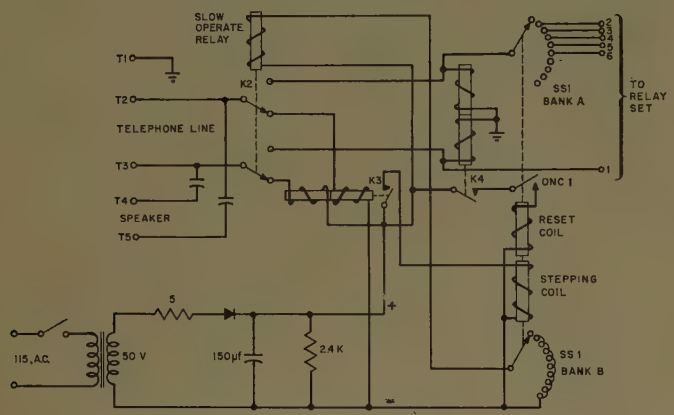

Fig. 2—Telephone remote control (remote end).

coil in the relay set (Fig. 3), the selected relay now operates. This closes a circuit containing a motor and power supply, both of which are at the remote end, for as long as the key KS1 at the control end (Fig. 1) is operated. Because of the rectifiers in series with the relays, the polarity determined by the key KS1 controls the direction of motor drive by selecting the appropriate relay. The correct setting having been obtained with the selected motor, operation B is completed.

Operation C

It remains to clear the line so that the next motor can be dialed. The operations switch S1 (Fig. 1) is set to position 3. This shorts T2 and T3 and connects both to the 48-volt dc power supply. Since there is no voltage between T2 and T3, but only from either of them to ground, relay K4 (Fig. 2) operates. Its contact energizes the reset coil of SS1, via its off-normal contact ONC1,

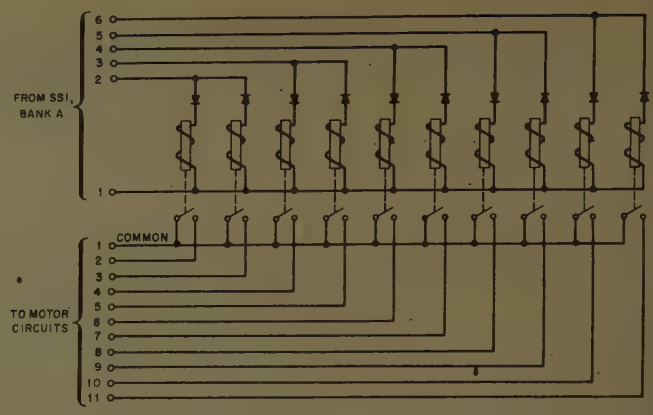

Fig. 3—Relay set.

which was closed in operation A, thus driving all the wipers of the stepping switch SS1 back to position 1. At this time, the off-normal contact ONC1 opens, and the wipers of the stepping switch SS1 stop. At the same time, the circuit of K2 is opened on bank B and it releases. Everything is now set as it was before operation A. When the operations switch S1 (Fig. 1) is again set in position 1, the next motor may be dialed as described under operation A.

Speakers

At both ends of the line, speakers are connected across terminals T4 and T5. The line is balanced (hence the two coils for relay K3), so that the speakers may be left permanently connected across the line through large capacitors and used at any time.

Conclusion

A circuit which uses only available and reliable components, and which can readily be constructed at low cost, has been described. It gives great flexibility in remote control with only a single telephone line by allowing any one of several motors to be dialed, then controlled and set, and, finally, released to select a new function. Each motor adjusts some quantity, such as frequency or direction of polarization, which can thereby be remotely controlled.

Acknowledgment

The circuit was constructed and tested by Rodney Melhuish, whose ability to improvise contributed greatly to the success of this arrangement.

Contributors

L. J. Anderson, for a photograph and biography, please see page 321 of the July, 1958 issue of these TRANSACTIONS.

❖

Morrel P. Bachynski (S'54–M'56) was born on July 19, 1930, in Bienfait, Saskatchewan, Canada. He received the B.E. degree in engineering physics in 1952, the M.S. degree in 1953, both from the University of Saskatchewan, and the Ph.D. degree from McGill University in 1955.

M. P. BACHYNSKI

Until October, 1955, as a member of the staff of the Eaton Electronics Research Laboratory, McGill University, he was engaged in investigations concerning aberrations in microwave lens systems. Since that time he has been with the RCA Victor Research Laboratories, Montreal, Canada, concerned primarily with short-wave propagation problems and is now head of the wave propagation division.

❖

D. K. Bailey was born in Clarendon Hills, Ill., on November 22, 1916. After receiving the B.S. degree in astronomy at the University of Arizona in 1937, he attended Oxford University as a Rhodes Scholar. He received the B.A. degree in physics in 1940, and the M.A. degree in 1943. From 1940 to 1941, he was in Antarctica as a physicist with the U. S. Antarctic expedition to make cosmic-ray observations.

D. K. BAILEY

Mr. Bailey served on active duty with the Signal Corps from 1941 to 1946. From 1941 to 1943 he was attached to the Royal Air Force and acted as the Air Ministry representative in the Inter-Services Ionosphere Bureau (ISIB). For the next twenty months, he was assigned to the War Department where he established the Radio Propagation Unit (now the Radio Propagation Agency). From April, 1945, to June, 1946, he served in Manila, Leyte, and Tokyo in connection with Signal Corps ionosphere stations. In Tokyo, he assisted the Japanese in reestablishing a radio research program.

In December, 1946, Mr. Bailey joined the RAND project at the Douglas Aircraft Company where he worked in the communication and electronics field. In 1948 he joined the National Bureau of Standards (CRPL) and from 1948 to 1950, he was a member of the U. S. delegation in Geneva, Switzerland, serving as chairman of the propagation working group of the Provisional Frequency Board. Since then, he has been a member of numerous U. S. delegations to international conferences, and now serves as the International Chairman of Study Group VI (Ionospheric Propagation) of the International Radio Consultative Committee (CCIR). From 1951 to 1955, as a consultant to his division chief, he was actively engaged in a senior capacity in a research group investigating regular long-distance VHF ionospheric propagation and related communications matters. In 1955 he joined the firm of Page Communications Engineers, Inc., as scientific director.

Mr. Bailey holds the Legion of Merit and is a member of Phi Beta Kappa. He received the 1951 Arthur S. Flemming Government Award and has received U. S. Department of Commerce awards for both meritorious and exceptional service. He is a member of the American Astronomical Society and the American Physical Society, and a fellow of the Royal Geographical Society and the Royal Astronomical Society.

❖

Alyce M. Conda, for a photograph and biography, please see page 321 of the July, 1958 issue of these TRANSACTIONS.

❖

Herman Vladimir Cottony (M'45–SM'51) was born in Nizhni-Novgarod, Russia, on March 27, 1909. He received the B.S. degree in 1932 from Cooper Union Institute of Technology, New York, N. Y.; the M.S. degree in electrical engineering in 1933 from Columbia University, New York, N. Y.; and the E.E. degree in 1946 from Cooper Union Institute of Technology.

H. V. COTTONY

From 1935 to 1937, he was a research engineer with Sonotone Corporation, Elmsford, N. Y. In 1937 he joined the staff of the National Bureau of Standards, Washington, D. C., and with the exception of a period of military leave from 1941–1945 has remained in their employ to the present time. He is now an electronic scientist engaged in antenna studies and design. During World War II, he was at Signal Corps laboratories in various capacities, including chief of the Thermionics Branch. He is author of a number of papers and reports on cosmic and radio noise and antennas.

Mr. Cottony is a member of Tau Beta Pi, RESA, U. S. Commission VI of URSI, and U. S. Preparatory Committee III of CCIR.

❖

Andre Dion (A'53) was born in Quebec City, Canada, on May 3, 1926. He received the B.S. degree in 1949, the M.S. degree in 1950, and the Sc.D. degree in 1953, all in physics, from Laval University. Since 1953 he has been employed at the Canadian Armament Research and Development Establishment, Valcartier, Quebec, where he is engaged in the design and development of microwave antennas.

A. DION

Dr. Dion is a member of the Canadian Association of Physicists.

❖

Robert C. Hansen (S'47–A'49–M'55–SM'56) was born on August 3, 1926, in St. Louis, Mo. His college studies at the Missouri School of Mines and Metallurgy, Rolla, were interrupted by service in the USN in 1945–1946 as an RT instructor. He then resumed studies at the same school, graduating in January, 1949, with the degree of B.S. in electrical engineering. The M.S. degree was granted in 1950 by the University of Illinois, Urbana, where for the next several years he was research assistant and research associate in the Antenna Laboratory. He received the Ph.D. degree in electrical engineering from the University of Illinois in May, 1955. Since that time he has been, successively, head, Surface Wave Group, head, Electromagnetic Research Section, and technical staff assistant to the department manager, Antenna Research Department, all at the Microwave Laboratory of Hughes Aircraft Co., Culver City, Calif.

R. C. HANSEN

Dr. Hansen is a registered Professional Engineer in Missouri, and is a member of the American Physical Society, Tau Beta Pi, Sigma Xi, Eta Kappa Nu, Phi Kappa Phi, and Commission VI, URSI.

Robert W. Hougardy was born on December 20, 1933, in Roundup, Mont. He received the B.S. degree in engineering physics from Montana State College, Bozeman, in 1955, and the M.S. degree in applied physics from the University of California at Los Angeles in 1957. He is at present working toward the Ph.D. in physics at U.C.L.A. under a Hughes Doctoral Fellowship.

R. W. HOUGARDY

In 1955 he joined the technical staff of the Hughes Research and Development Laboratories, Culver City, Calif., where he is currently employed. He has been primarily interested in surface-waves and their applications to microwave antennas.

Mr. Hougardy is a member of Tau Beta Pi and Phi Beta Kappa.

❖

H. E. J. Neugebauer was born in Berlin, Germany, on May 8, 1905. He studied mathematics and physics at the University of Berlin from 1924 to 1929. In 1935, he received the Doctor's degree from the Technische Hochschule of Dresden with a dissertation on multicolor printing. Until 1951 he worked on various research and development projects, most of which were connected with optics or colorimetry.

H. NEUGEBAUER

He went to Montreal, Canada, in 1951 and applied his experience in the field of visible light to the study of microwave optics and electromagnetic wave theory. He worked for the Eaton Electronics Research Institute of McGill University, for Adalia Ltd., and, recently, for RCA Victor Company Ltd. as head of the wave propagation section of the Research Laboratories in Montreal. Presently he is a consultant to RCA Victor Company and others.

Dr. Neugebauer is a member of the Optical Society of America and the Technical Association of the Graphic Arts, and has published papers on optics, colorimetry, and electromagnetic wave theory. At the past Annual Assembly of URSI in Boulder, Colo., he was elected a member of Commission VI.

I. P. Shkarofsky (M'58) was born in Montreal, Canada, on July 4, 1931. He received the B.Sc. degree with first class honors in physics and mathematics from McGill University in 1952. In the following year, he obtained the M.Sc. degree conducting his research at the Eaton Electronics Research Laboratory, McGill University, in the fields of microwave optics and antennas. He then joined the microwave tube and noise group at the Eaton Electronics Research Laboratory and received the Ph.D. degree in 1957 with a dissertation on modulated electron beams in space-charge-wave tubes and klystrons. He worked during the summers for the Defense Research Board and for Canadian Aviation Electronics Ltd. in electronics and radar research. After graduation, he joined the Research Laboratories, Electromagnetic Division, where he is engaged in research on microwave diffraction, electromagnetic wave interaction with plasmas, and obstacle gain.

I. P. SHKAROFSKY

Dr. Shkarofsky is an associate member of the Canadian Association of Physicists.

❖

Louis G. Trolese, for a photograph and biography, please see page 323 of the July, 1958 issue of these TRANSACTIONS.

❖

James R. Wait, for a photograph and biography, please see page 323 of the July, 1958 issue of these TRANSACTIONS.

❖

Alan T. Waterman, Jr. (S'51–A'53–SM'57) was born in Northampton, Mass., on July 8, 1918. He received the A.B. degree in physics in 1950 from Princeton University, the B.S. degree in meteorology in 1940 from the California Institute of Technology, and the A.M. degree in 1949 and the Ph.D. degree in 1952 in engineering sciences and applied physics from Harvard University.

He was employed by American Airlines as a meteorologist from 1940 to 1941, when he became an instructor in meteorology at the University of Minnesota. From 1942 to 1945 he did research on methods of weather forecasting at California Institute of Technology. He then engaged in research on radio meteorology at the University of Texas and Columbia University from 1945 to 1946. For the next six years, he was a research assistant at Harvard University in ionospheric radio-wave propagation.

A. T. WATERMAN, JR.

Presently, he is associate professor of electrical engineering at Stanford University, where he is doing research in radio wave propagation with particular emphasis on tropospheric scatter. He also is Associate Director of the Systems Techniques Laboratory at Stanford for a program of electronic countermeasures, and Consultant to Weapons Systems Evaluation Group, Department of Defense.

Dr. Waterman is a member of the American Physical Society, the American Meteorological Society, the American Association for the Advancement of Science, and Sigma Xi.

❖

Alvin C. Wilson (M'57) was born in Casper, Wyo., on September 24, 1925. From 1943 to 1945 he was a radio operator and technician in the U. S. Army, with service in Europe. He received the B.S. degree in electrical engineering in 1948 from the University of Colorado in Boulder.

A. C. WILSON

From June, 1948, to June, 1949, he did seismograph work with the Stanolind Oil and Gas Co., Fort Worth, Texas. From June, 1949, through January, 1951, he was employed as an electrical engineer with the Standard Engineering and Manufacturing Co., Denver, Colo. From February, 1951, to October, 1955, he was a member of the civilian instructor staff in radar bombing systems at Lowry Air Force Base, Denver, Colo. Since October, 1955, he has been an electronic engineer in the Radio Propagation Physics Division of the Boulder Laboratories, National Bureau of Standards.

Mr. Wilson is a member of the Research Engineering Society of America.

Index to

IRE TRANSACTIONS

ON

ANTENNAS AND PROPAGATION

Volume AP-6, 1958

IRE Transactions on Antennas and Propagation

Index to Volume AP-6, 1958

Contents

Volume AP-6, Number 1, January, 1958

Volume AP-6, Number 2, April, 1958

Volume AP-6, Number 3, July, 1958

Volume AP-6, Number 4, October, 1958

Index to Authors

Index to Technical Subjects

INSTITUTIONAL LISTINGS

The IRE Professional Group on Antennas and Propagation is grateful for the assistance given by the firms listed below, and invites application for Institutional Listing from other firms interested in the field of Antennas and Propagation.

ANDREW CORPORATION, 363 E. 75th St., Chicago 19, Ill.
Antennas, Antenna Systems, Transmission Lines, Development and Production.

ANTLAB, INC., 6330 Proprietors Rd., Worthington, Ohio
Antenna Pattern Range Systems—Recorders & Mounts.

BLAINE ELECTRONETICS, INC., 14757 Keswick St., Van Nuys, Calif.
Antennas, Paraboloids, Scale Models, Antenna Radiation Pattern Measurement Towers.

COMMUNICATION PRODUCTS COMPANY, INC., Marlboro, N. J.
Fixed Station and Vehicular Antennas and Associated Cable Systems

DEVELOPMENTAL ENGINEERING CORP., 1001 Conn. Ave. N.W., Washington, D. C. and Leesburg, Va.
Research, Development, Installation of Antennas and Antenna Equipment for Super Power Stations.

DORNE AND MARGOLIN, INC., 29 New York Ave., Westbury, L. I., N. Y.
Research, Development, and Manufacture of Airborne Antennas and Systems

THE GABRIEL LABORATORIES, Div. of the Gabriel Co., 135 Crescent Road, Needham Heights 94, Mass.
Research and Development of Antenna Equipment for Government and Industry.

HUGHES AIRCRAFT COMPANY, Culver City, Calif.
Research, Development, Mfr.: Radar, Missiles, Antennas, Radomes, Tubes, Solid State Physics, Computers.

I-T-E CIRCUIT BREAKER CO., Special Products Div., 601 E. Erie Ave., Philadelphia 34, Pa.
Design, Development and Manufacture of Antennas, and Related Equipment.

JANSKY & BAILEY, INC., 1339 Wisconsin Ave. N.W., Washington 7, D. C.
Radio & Electronic Engineering; Antenna Research & Propagation Measurements; Systems Design & Evaluation.

MARK PRODUCTS CO., 6412 W. Lincoln Ave., Morton Grove, Ill.
Multi Element Grid Parabolas, Antennas for Two-Way Communications, R & D.

THE RAMO-WOOLDRIDGE CORPORATION, Los Angeles 45, Calif.

TRANSCO PRODUCTS, INC., 12210 Nebraska Ave., Los Angeles 25, Calif.
Res., Design, Dev., & Mfr. of Antenna Systems & Components for Missile, Aircraft & Ground Installations.

WHEELER LABORATORIES, INC., 122 Cutter Mill Road, Great Neck, N. Y.
Consulting Services, Research and Development, Microwave Antennas and Waveguide Components.

WIND TURBINE COMPANY, West Chester, Pa.
Complete Antenna Systems and Towers

The charge for an Institutional Listing is $25.00 per issue or $75.00 for four consecutive issues. Application may be made to the Technical Secretary, The Institute of Radio Engineers, 1 East 79th Street, New York 21, N.Y.